Engineering Metal Oxides for (Photo)Electrochemical Oxygen Evolution/Hydrogen Evolution Reactions

A Dissertation Submitted to the

Indian Institute of Technology Guwahati

in Partial Fulfilment for the Degree of

DOCTOR of PHILOSOPHY

by

Ching Thian Moi

DEPARTMENT OF CHEMISTRY

INDIAN INSTITUTE OF TECHNOLOGY GUWAHATI

GUWAHATI, ASSAM, INDIA

OCTOBER 2022

Engineering Metal Oxides for (Photo)Electrochemical Oxygen Evolution/Hydrogen Evolution Reactions

A Dissertation Submitted to the

Indian Institute of Technology Guwahati

in Partial Fulfilment for the Degree of

DOCTOR of PHILOSOPHY

by

Ching Thian Moi

Roll No - 176122009

DEPARTMENT OF CHEMISTRY

INDIAN INSTITUTE OF TECHNOLOGY GUWAHATI

GUWAHATI, ASSAM, INDIA

OCTOBER 2022

STATEMENT

I, hereby declare that the scientific findings incorporated in this thesis entitled, "**Engineering Metal Oxides for (Photo)Electrochemical Oxygen Evolution/Hydrogen Evolution Reactions**" is the result of my research work under the supervision of Prof. Mohammad Qureshi, at the Department of Chemistry, Indian Institute of Technology Guwahati, Assam, India, for the award of the degree of Doctor of Philosophy.

The research work included in this thesis is the outcome of original research done by me except where otherwise mention in this thesis with proper citations. I declared that the experiment were perform in accord with the ethics policies and integrity standards of the Indian Institute of Technology Guwahati. The experimental data included in this thesis were present honestly and without prejudice. The thesis work has not been submitted for a degree or professional qualification to any other university or institution.

IIT Guwahati
October 2022

Ching Thian Moi
Candidate
Department of Chemistry
IIT Guwahati
Guwahati-781039, Assam
India

Dr. Mohammad Qureshi
Professor
Department of Chemistry
Indian Institute of Technology Guwahati
Guwahati – 781039, India
Tel: +91 – 361 – 2582320;
Fax: +91 – 361 – 2582349
Email: mq@iitg.ac.in

Certificate

I, hereby certified that the work described in this thesis entitled "**Engineering Metal Oxides for (Photo)Electrochemical Oxygen Evolution/Hydrogen Evolution Reactions**" by Miss. **Ching Thian Moi**, Department of Chemistry, Indian Institute of Technology Guwahati has been carried out under my supervision and has not been submitted elsewhere for a degree.

17/10/22

Guwahati
October 2022

Mohammad Qureshi
Thesis supervisor
Department of Chemistry
Indian Institute of Technology Guwahati
Guwahati – 781039, Assam, India

ACKNOWLEDGEMENT

It gives me immense pleasure to express my heartfelt gratitude and appreciation to everyone who has contributed in some way to the successful completion of my Ph.D. thesis work and for making this journey a beautiful and memorable one. I feel humble, grateful, and appreciative for the help and support I have received to reach this journey.

Foremost, I would like to express my sincere gratitude to my thesis supervisor Prof. Mohammad Qureshi for his constant guidance, prudent counsel, and encouragement throughout my Ph.D. I am also grateful for the opportunity to work under your excellent supervision. Thank you, sir, for providing the platform to explore my ideas and thoughts during my research work and for pushing my limits to achieve the unachievable.

I wish to extend my heartfelt gratitude to my doctoral committee members, Prof. Parameswar Krishnan Iyer, Prof. Chivukula V Sastri, and Dr. Nageswara Rao Peela for their periodic evaluation, technical suggestions, feedback, and motivation during my Ph.D. tenure. My sincere gratitude to Prof. C. V. Sastri for providing the CH Instrument facility. I thank the faculty members and staff of the Department of Chemistry. My sincere gratitude to the staff of the Central Instruments Facility, for their assistance with several analytical instruments, essential during my research work. My heartfelt gratitude to IIT Guwahati for the fellowship and all other important facilities and the Department of Science and Technology, India for the financial support.

My deep gratitude and appreciation to each member of MSL 109 for their constant support, fruitful suggestions, and input throughout my research work. My heartfelt gratitude to my seniors Dr. A. S Patra, Dr. M. S Ansari, Dr. A. Banik, Dr. G. Gogoi, Dr. T. K. Sahu, Dr. S. Alam, Dr. A. K. Shah, my batch mates Manoj and Sourav, and present laboratory members Alpana, Nitul, Peeyush and Anjana for their support and for creating a healthy work environment.

I awe a deep sense of gratitude to Joint Registrar T T Haokip and his family for providing me with spiritual guidance, countless good meals, and physical support during my stay in campus. This journey would not have been memorable without my friends Christy Noche K Marak, Emily Thomas, Thangsei Nengneilhing Baite, and Serena Ngiimei D. Thank you all for listening to my boring stories, for the constant physical and emotional support, and for keeping me sane throughout this roller coaster. Thank you, for cheering me up through the hard times and the constant failure. I would also like to thank Iban, Kisan, Bishwanath, Alhing, and to all my friends in the IITG campus.

Lastly, my Ph. D. endeavor would not have been possible without the unconditional love, support, and blessings from my family. My sincere love and heartfelt gratitude to my beloved parents (Ts. SingKhanKhup & Mrs. NingKhoKim) for their constant prayers, unconditional love, and sacrifices. I am also grateful to my brothers (Ts Paumunmuang Simte & Ts Ginhauthang Simte) for their love and emotional support during my Ph.D. tenure. My heartfelt gratitude to Jouthansang Simte for being my emotional and physical support and for pulling me through my worst times.

Moi

TABLE OF CONTENTS

Dedicated To

My Granny

"Niang Kim"

Thesis Title: Engineering Metal Oxides for (Photo)Electrochemical Oxygen Evolution/Hydrogen Evolution Reactions

Name of the Candidate: Ching Thian Moi
Registration Number: 176122009
Thesis Supervisor: Prof. Mohammad Qureshi
Department: Chemistry
Institute: Indian Institute of Technology Guwahati, Assam – 781039, India

Thesis Overview

Chapter 1: Chapter one demonstrates the basic technique of (photo)electrochemical water splitting to meet global energy demands and environmental crises. The present chapter also describes the working principle of (photo)electrochemical water splitting in different electrolytic conditions. This chapter also discussed the literature survey of current state-of-the-art scenarios, challenges, and various strategies for the development of stable, efficient, cheap, and abundant catalysts for practical application.

Chapter 2: This chapter discusses the comprehensive synthetic protocols of the metal oxides and the co-catalysts, which are employ to show (photo)electrochemical water splitting. The chapter also describes instrumentation techniques used in the characterization of the materials. It demonstrates the complete experimental procedure used in (photo)electrochemical characterization of the catalysts. In this chapter, different performance perimeters for photo and electrocatalyst are also discuss in detail.

Chapter 3: Enhanced Surface Reaction Kinetics in Vanadium Doped Hematite co-modified by NiFe Layered Double Hydroxide for Electrocatalytic Oxygen Evolution Reaction. (C. T. Moi et al., *Electrochim. Acta*, 2021, 370, 137726)

The present chapter describes exploring a low-cost, efficient and stable electrocatalyst to replace noble metal-based catalysts for oxygen evolution reaction (OER) for practical applications. Herein, we have proposed vanadium doping and co-modification of α- Fe_2O_3 utilizing NiFe LDH for noble metal-free electrocatalytic oxygen evolution reaction (OER), which exceeds the

performance of benchmark RuO_2 under similar experimental conditions. Vanadium doping enhances the carrier density, whereas NiFe LDH contributes to the surface-active sites for promoting water oxidation kinetics. A five-fold enhancement in electrochemically active surface area (ECSA) for α- Fe_2O_3:V-NiFe LDH (2.5 mF/cm^2) compared to α- Fe_2O_3 (0.5 mF/cm^2) is observed. The composite α- Fe_2O_3:V-NiFe LDH exhibited an impressive overpotential of 190 mV @ 10 mA/cm^2 with corresponding Tafel slopes of 42 mV/dec. Detailed electrochemical studies with long-term stability indicate the potential of as-synthesized composite α- Fe_2O_3:V-NiFe LDH for utilization as a heterogeneous catalyst for efficient oxygen evolution reaction.

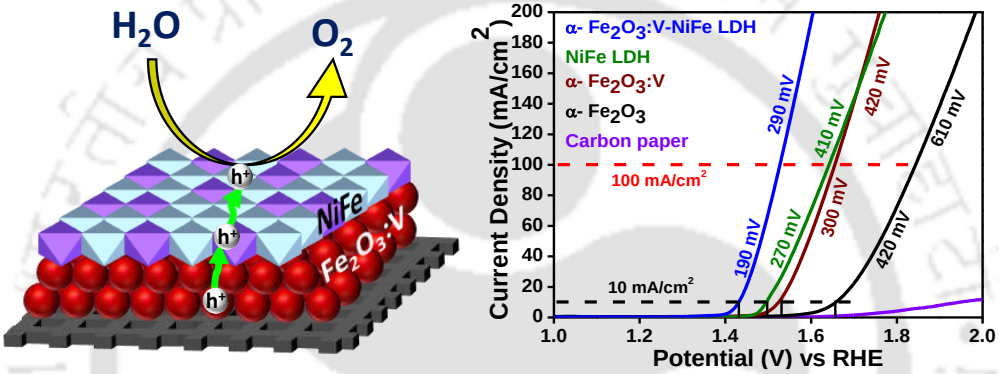

Figure 1: Graphical illustration of probable reaction mechanism of α- Fe_2O_3:V-NiFe LDH along with *JV* of all prepared electrocatalyst in 1M KOH.

Chapter 4: Hierarchical FeO(OH)/CoCeV (oxy)hydroxide as a water cleavage promoter (C. T. Moi et al., ACS Appl. Mater. Interfaces, 2021, 13, 51151–51160)

Search for a bifunctional electrocatalyst having water cleavage promoting ability along with the operational stability to efficiently generate oxygen and hydrogen could lead to robust systems for applications. These fundamental ideas can be achieved by designing the morphology, tuning the electronic structure, and using dopants in their higher oxidation states. Herein, we have fabricated a binder-free FeO(OH)-CoCeV-layered triple hydroxide (LTH) bifunctional catalyst by a two-step hydrothermal method, in which the nanograin-shaped FeO(OH) coupled with CoCeV-LTH nanoflakes provide more electro catalytically active sites and enhanced the charge transfer kinetics for hydrogen evolution reaction (HER) and oxygen evolution reaction (OER). The composition (FeO(OH)-$Co_{0.5}Ce_{0.05}V_{0.15}$-LTH) acts as an efficient water cleavage composite, which yields an overpotential of 53 mV for HER, and 227 mV for OER to drive 10 mA/cm^2 current

density in 1M KOH, with a corresponding Tafel slope of 70 mV/dec for HER and 52 mV/dec for OER. Furthermore, for the overall water splitting reaction, the heterostructure FeO(OH)-$Co_{0.5}Ce_{0.05}V_{0.15}$-LTH, acts as a dual-functional electrocatalyst, which requires a cell voltage of 1.52 V vs RHE to drive 10 mA/cm^2 current density.

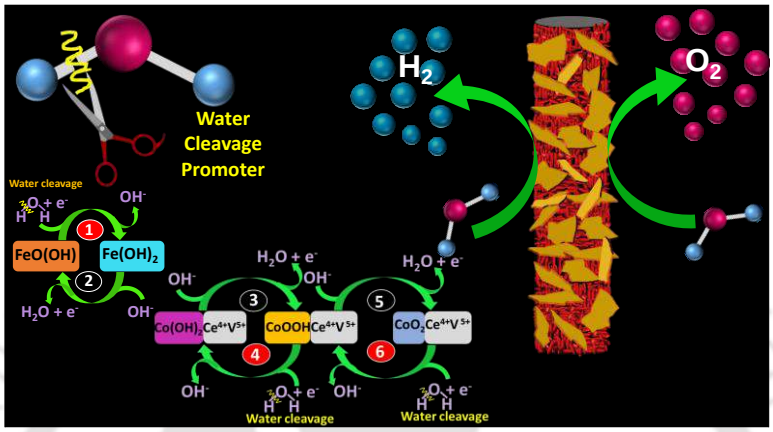

Figure 2: Graphical representation of probable water cleavage mechanism of FeO(OH)-$Co_{0.5}Ce_{0.05}V_{0.15}$-LTH.

Chapter 5: Tapping the potential of high-valent Mo and W metal centres for dynamic electronic structure in multi-metallic FeVO(OH)/$Ni(OH)_2$ for water splitting (*ACS Appl. Mater. Interfaces* 2023, 15, 4, 5336–5344)

Rationally designing a noble metal-free electrocatalyst for OER and HER is pivotal for large-scale energy generation via water splitting. Multi-metallic electrocatalyst FeVO(OH)/$Ni_{0.86}Mo_{0.07}W_{0.07}(OH)_2$ aiming at tuning the electronic structure is fabricated, giving a huge improvement in water splitting reaction kinetics. By taking the advantage of (ē–ē) repulsions at the t_{2g} level, we have introduced high-valent Mo and W to provide a viable path for π–electron donation from oxygen 2p orbitals to vacant Mo and W orbitals for a dynamic electronic structure and interfacial synergistic effect which optimized the bond lengths for reaction intermediates to facilitate the water-splitting. The hybrid catalyst FeVO(OH)/NiMoW$(OH)_2$ shows an intrinsic activity and durability towards OER and HER.

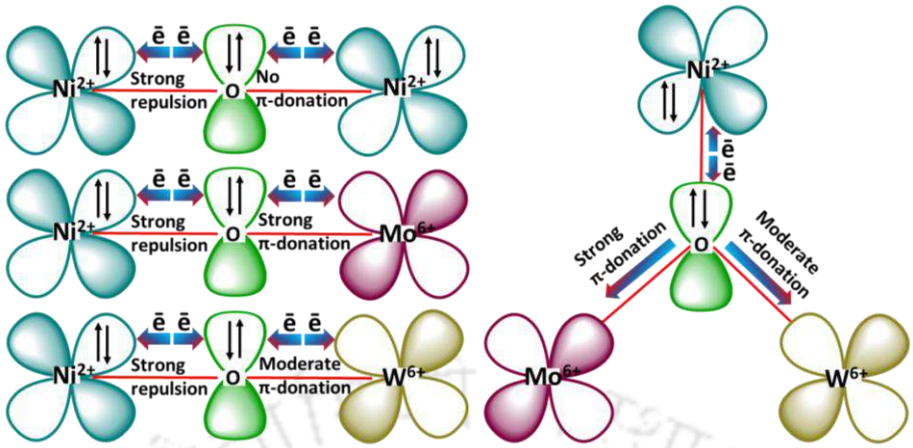

Figure 3: Schematic illustrations of the electronic coupling between Ni^{2+}, Mo^{6+} and W^{6+} of $NiMoW(OH)_2$.

Chapter 6: Noble metal-free hierarchical VS_2 onto WO_3 nanoflakes as heterojunction strategy for photoelectrochemical water oxidation (C. T. Moi et al., *Sustainable Energy Fuels*, 2019, 3, 3481)

Chapter 6 describes the design of highly surface reactive and noble metal-free VS_2 nanoflowers onto in situ grown WO_3 photoanode as a heterojunction strategy for efficient charge separation. The main drawback of WO_3 is slow surface reaction kinetics leading to undesired carrier recombination. VS_2, with active sites both on the edge and basal plane, reduces the surface charge recombination and enhances the kinetics of O_2 evolution reaction. The current chapter study about the charge carrier density, charge transfer kinetics, and durability of the prepared catalyst for PEC water oxidation. A significant increment in photocurrent density is observed for WO_3-VS_2 composite as compared to the bare WO_3 with an increase in charge carrier density from 2.5 x 10^{21} for WO_3 to 1.5 x 10^{22} for WO_3-VS_2. Electrochemical impedance spectroscopy indicates an effective reduction in charge transfer resistance from 7.71 x 10^5 for WO_3 to 2.79 x 10^3 for WO_3-VS_2. A Faradaic efficiency of 87 % is indicative that the oxygen generated in the reaction is mainly due to photoelectrochemical water oxidation.

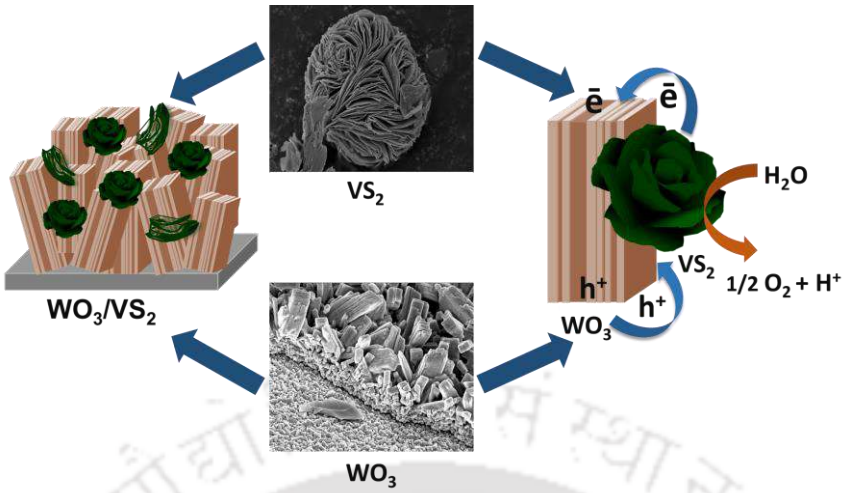

Figure 4: Schematic illustrations of synthesis and reaction mechanism of WO_3-VS_2.

Chapter 7: Thesis Overview and Future Perspectives

This chapter, in brief, outlines the outcomes and the overview of the current thesis. Herein, it also discusses the possible modification that can be perform with the metal oxides/hydroxide to enhance OER and HER performance in the near future.

CHAPTER 1

Introduction

Chapter one demonstrates about the basic techniques of (photo)electrochemical water splitting to meet the global energy demand and environmental crisis. The present chapter also describe about the working principle of (photo)electrochemical water splitting in different electrolytic conditions. This chapter also discusses the literature survey of current state-of-the art scenarios, challenges and various strategies for the development of stable, efficient, cheap and abundance catalyst for practical applications.

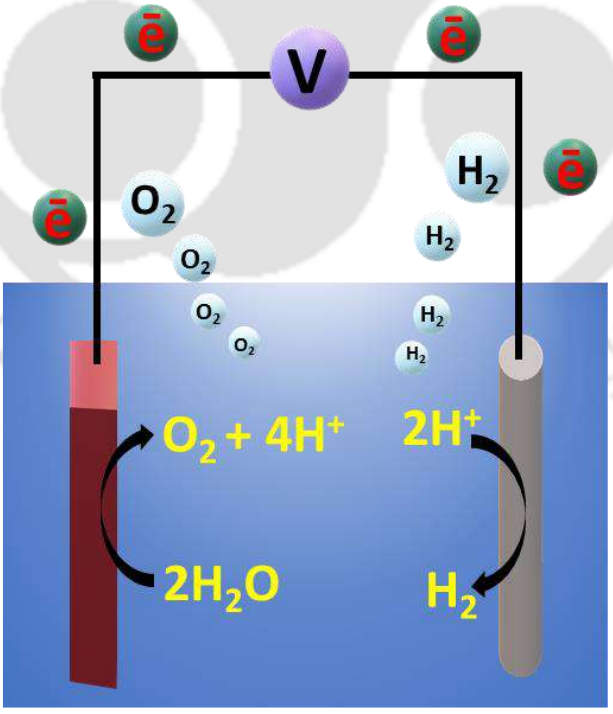

1.1 GLOBAL ENERGY CONSUMPTION AND ENVIRONMENTAL CRISIS

Energy is indispensable for the social and economic development of mankind. Energy can be obtained from non-renewable sources like fossil fuels, petroleum, coal, oil, natural gas, etc, and from renewable sources like solar, hydropower, wind, biomass and geothermal energy.[1] With the advancement in new technology and the rapid increase in the economic growth of developing countries, the demand for energy consumption has surged in the 21st century.[1, 2] The total primary energy consumption from fossil fuels is approximately 80 %. The Sustainable Development Goals (SDGs) were signed by both developed and developing countries in September 2015, is officially known as the 2030 Agenda for Global Development of SDGs. The SDGs 2015 give importance to air pollution, and includes two primary objectives: (i) Reduction of health problems caused by hazardous elements (SDG 3.9) and (ii) The action of reducing the air pollution from metro cities affecting people (SDG 11.6).[3]

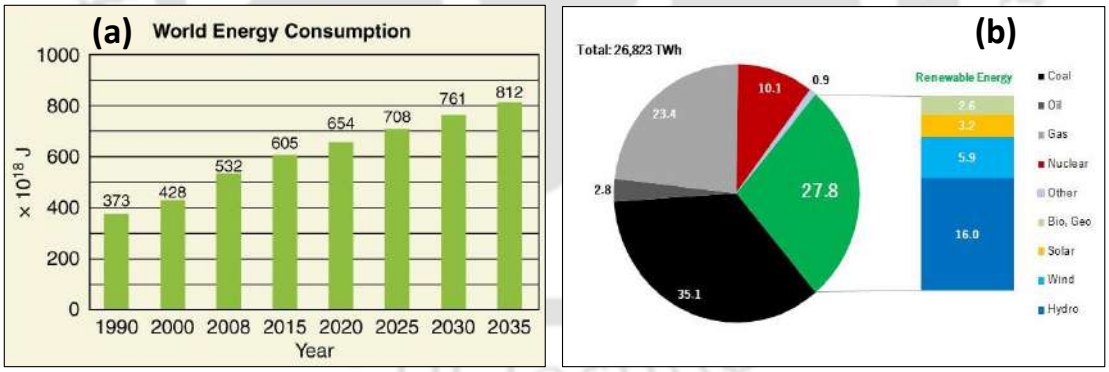

Figure 1.1 (a) Bar diagram showing probable world energy consumption (Source: https://www.texasgateway.org/resource/79-world-energy-use), (b) Pie chart showing the global primary energy consumption based on fuels sources (Source: https://www.renewable-ei.org/en/statistics/international/).

Figure 1.1 (a) bar diagram indicates the expected global energy consumption. The primary global energy consumption from different fuel sources based on 2021 data analysis is shown in **Figure 1.1 (b)**. According to World Energy data based on 2021, major global energy

consumption comes from non-renewable sources like crude oil, coal, and natural gas.[4, 5]. With this surge in global energy consumption, accompanied with the fast-growing technology, Environmental Impact Assessment (EIA) agency predicts that the CO_2 emissions would increase by 35 % in 2035. The dependency on fossil fuels as the main sources of energy will continue till 2035 and renewable energy sources will contribute about 14 % of global energy consumption.[6] Therefore, the main objective of change in the global energy consumption is to reduce CO_2 emissions.

Global warming and climate change are critical threats to the environment and humankind. The rapid increase in the temperature of the Earth's surface is termed global warming and the results of global warming lead to increase in sea level, rapid increase in glaciers melting, drought, flood and an increase in greenhouse gas emissions which cause climate changes. Greenhouse gases are primarily caused by natural calamities, which include volcanic eruptions, the release of methane gases, forest fires and deforestation.[7] The rapid emission of CO_2 is considered to be the main cause of greenhouse gas, which originates from the combustion of fossil fuels, decomposition of biomass and the exhalation processes of mankind and animals.[1] So, the hunt for alternative renewable sources of energy to meet the global energy demands is indispensable.

1.2 RENEWABLE ENERGY SOURCES

With the depletion of fossil fuels and an increase in energy demand, the generation of clean, renewable and environmentally friendly sources of energy is a globally challenging issue.[1,2,8] Renewable energy can reduce greenhouse gas emissions by contributing two-thirds of the total global energy demand, which is required to limit an increase in the average global surface temperature below 2°C by 2050.[2] Hydrogen energy plays a critical role in achieving zero CO_2 emission.[8] Hydrogen is a versatile energy carrier and an alternative fuel that can

replace the total energy dependency on fossil fuels in principle. In the meantime, hydrogen energy can be easily stored and transported and can also be used in numerous fields such as electricity, thermal, transport and industry sectors, which account for two-thirds of global CO_2 emission.[8, 9] Hydropower contributes the largest renewable energy source as shown in **Figure 1.2.** The contribution of renewable energy from different sources is expected to increase by 86 % in 2050 from the total global primary energy supply chain as estimated by International Renewable Energy Agency (IRENA). In the past two decades, solar and wind energy technologies have developed at a rapid rate.[10]

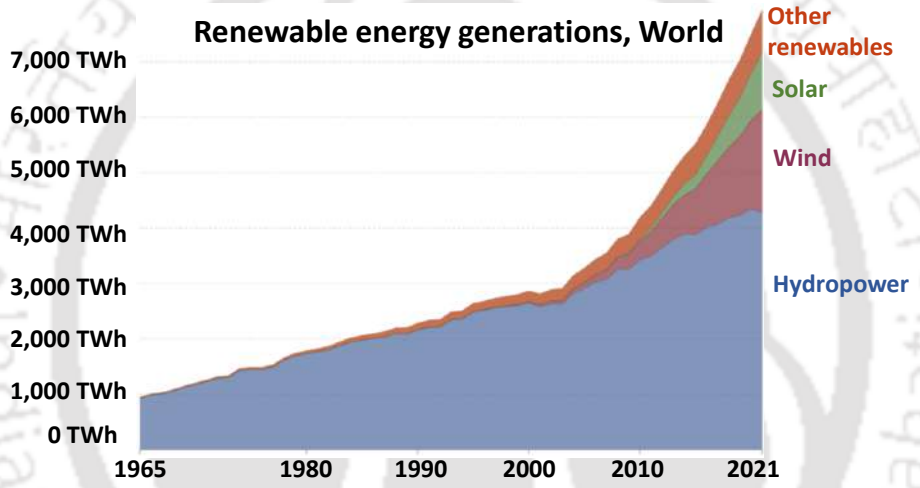

Figure 1.2 Global renewable energy production (Source: https: // www. greenesa. com /article/renewable-energy-statistics).

Solar energy is the most abundant and important renewable source of energy obtained from sunlight. The energy harnessed from sunlight is clean, renewable and cheap and is available in direct and indirect forms.[10] The Sun produces solar energy at a rate of 3.8×10^{23} kW, of which, the earth's surface captures approximately about 1.8×10^{14} kW of solar energy from the Sun.[11] Solar energy can be utilized in various fields such as photovoltaic, solar cooking, solar drying technology, solar thermal power etc. Solar energy is directly converted to electricity by photovoltaic device and electricity can be stored as hydrogen storage, electrolyzer and fuel cell. However, the challenge lies in the development of efficient

and stable photoelectrode for storage, harnessing and application.[11, 12] Hydrogen has a high gravimetric energy value of 141.9 MJ/kg, which is higher than most traditional fossil fuels like methane (55.5 MJ/kg), gasoline 47.5 (MJ/kg), diesel 44.8 (MJ/kg) and methanol (20.0 MJ/kg), and H_2 also has a low volumetric energy density of 5.6 MJ/L in comparison to gasoline (32.0 MJ/L). However, H_2 is technically produced by reforming methane (CH_4) gas, which emits harmful CO_2 gas. Therefore, the development of highly efficient, low cost and zero-carbon-emission hydrogen production technology at an industrial scale is crucial.[13, 14] Photo(electrochemical) water splitting is a promising approach for the generation of hydrogen energy with zero emission and holds great potential for future energy prospects.

1.3 (PHOTO)ELECTROCHEMICAL WATER SPLITTING

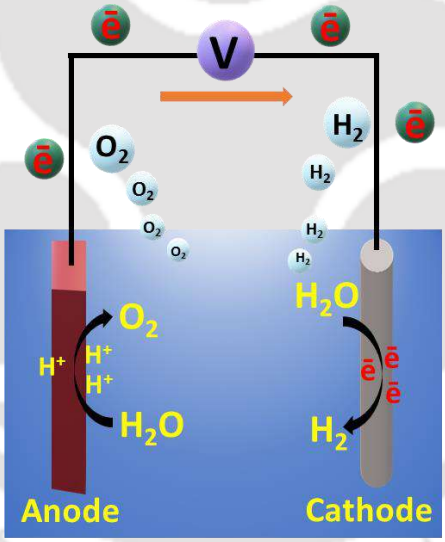

Figure 1.3 Graphical representation of (Photo)electrochemical water splitting, where oxidation takes place at the anode and reduction at the cathode respectively in an aqueous medium.

(Photo)electrochemical (PEC) water splitting is a process to convert solar energy to storable hydrogen fuel by applying solar energy or electricity, which offers a promising strategy for the generation of renewable hydrogen fuel and environmental remediation.[15-17] Since Fujishima and Honda first reported PEC water splitting using TiO_2 as photoanode in 1972, numerous efforts have been made to develop an efficient catalyst for hydrogen production.[16] A

typical (photo)electrochemical (PEC) cell is composed of a photoanode (working electrode), counter electrode (platinum/graphite rod), and reference electrode (Ag/AgCl or Hg based electrodes) immersed in an electrolyte as shown in **Figure 1.3**.[15, 17]

(Photo)electrochemical water splitting involves two half-reactions, where oxygen evolution reaction (OER) takes place at the anode, and hydrogen evolution reaction (HER) at the cathode respectively.[18] The possible reactions process taking place based on the electrolytic condition are discussed below.

$$H_2O \longrightarrow H_2 + \frac{1}{2}O_2 \, , E^0 = 1.23 \text{ V} \quad (1.1)$$

In neutral medium:

At Anode,

$$H_2O \longrightarrow 2H^+ + \frac{1}{2}O_2 + 2\bar{e}, E^0 = 1.23 \text{ V} \quad (1.2)$$

At cathode,

$$2H_2O + 2\bar{e} \longrightarrow H_2 + 2OH^-, E^0 = 0.0 \text{ V} \quad (1.3)$$

In alkaline medium:

At anode,

$$2OH^- \longrightarrow H_2O + \frac{1}{2}O_2 + 2\bar{e}, E^0 = -0.40 \text{ V} \quad (1.4)$$

At cathode,

$$2H_2O + 2\bar{e} \longrightarrow H_2 + 2OH^-, E^0 = 0.83 \text{ V} \quad (1.5)$$

For PEC water splitting, the valence band (VB) and conduction band (CB) positions of a semiconductor should thermodynamically stay below the water oxidation potential (1.23 V vs normal hydrogen electrode, NHE) and above the reduction potential (0 V vs NHE). An ideal

semiconductor with a bandgap of ~2.0 eV can achieve a photocurrent density of 14.5 mA/cm^2 under AM 1.5 G illumination (100 mW/cm^2), with a theoretical solar-to-hydrogen (STH) conversion efficiency of 17.9 %.[15] Photoanode can be selected based on its light-harvesting capability and its wide light absorption range. As shown in **Figure 1.4**, PEC water splitting is composed of three processes: (1) light absorption to generate electrons (ē) and holes h$^+$; (2) charge generation, separation, and transfer; (3) surface chemical reaction.[19]

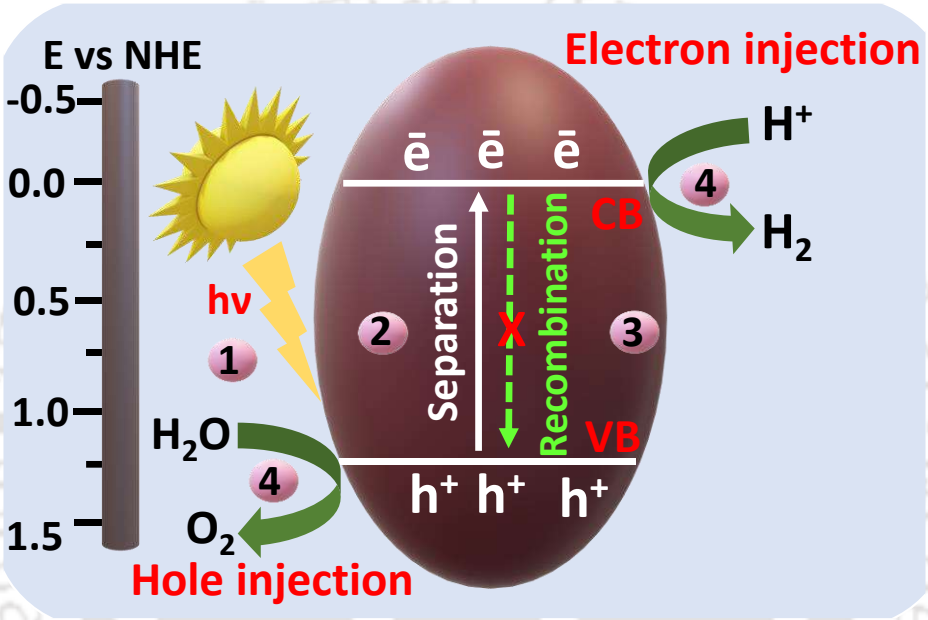

Figure 1.4 Schematic illustration of various steps involving photoelectrochemical (PEC) water splitting.

1.4 STRATEGIES TO IMPROVE (PHOTO)ELECTROCHEMICAL PERFORMANCE

In this section, we have summarized different strategies reported in the literature to improve the (photo)electrochemical performance of the material for oxygen evolution reaction (OER) and hydrogen evolution reaction (HER). The important strategies adopted are classified as follows: (1) Doping; (2) Heterostructure strategy; (3) Co-Catalyst modification; (4) Surface modification.

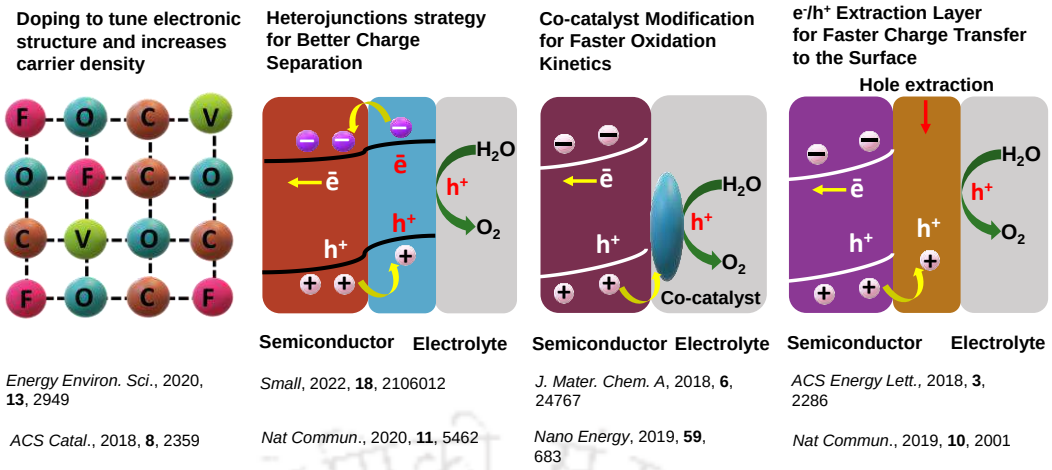

Figure 1.5 Schematic graphic showing different modification strategies for (photo)electrochemical water splitting.

1.4.1 Heteroatom doping

Heteroatom doping is an important strategy to regulate the electronic structure of materials for (photo)electrocatalytic performance. The introduction of heteroatom changes the crystal lattice structure, thereby, changing the electronic environment. The change in electronic structure generates vacancy, additional active sites and enhances the catalytic activities.[20-22]

Single/dual metal atom dopants

Heteroatom doping can be classified into three types: dual-metal atom doping, dual-non-metal atom doping, and metal and non-metal atom doping. The original lattice structures get distorted with doping due to differences in atomic radii, which result in the redistribution of an electron. This electronic structural modification can activate either dopants or neighbouring atoms to be catalytically active centers.

For transition metal-based materials, the single or dual metal atom is one important strategy for enhancing catalytic performance. Vanadium with its flexible redox state can optimize adsorption energy of reaction intermediates for OER.[21, 23] Li *et al.* reported vanadium doped NiFe LDH for water oxidation, which results in change in the electronic structure and

decrease in energy band gap which generates additional active sites, faster electronic transport, and better conductivity.[21] Cerium (Ce) is an important transition element for its good electrical conductivity and facile redox reactions. The variable oxidation state of Ce also provides robust electron interactions with other metal ions.[24, 25] The doping of Ce ions optimized the local electronic structures of the OER intermediates, thereby facilitating the OER reactions. For examples, doping concentration of 30 % Ce doped NiFe LDH exhibits a low overpotential of 242 mV to drive 10 mA/cm^2 current density.[24]

Dual metal cation doping is found to efficiently cause lattice distortion as compared to single doping, and dual metal doping causes a reduction in the water dissociation energy and optimizes the adsorption energy for the reaction intermediates during the HER and OER processes.[26-29] Co-doping not only improves the reactivity of the active site but also activates the neighbouring atom to be catalytically active, by tuning the electronic properties.[22-28] Y. Li *et al.* synthesize Co and Fe co-doped $NiSe_2$ nanosheets. The co-doping of Fe and Co cations facilitates stronger electronic interaction due to lattice distortion and optimized adsorption energy of reaction intermediates as compared to single metal doped or pristine $NiSe_2$ nanosheets. The optimized catalyst $Fe_{0.09}Co_{0.13}$-$NiSe_2$ show an overpotential of 251 mV for OER and 92 mV for HER respectively to drive 10 mA/cm^2. [27] The co-doping of Mo and Fe in $Ni(OH)_2$/NiOOH nanosheets is reported by Shen *et al.*, in which the experimental results show the enhancement in stability and electrocatalytic properties of $Ni(OH)_2$/NiOOH nanosheets. The improvement with co-doping of Mo and Fe can be attributed to the synergistic effect to optimize the OH_{ad} and the composite MoFe:$Ni(OH)_2$/NiOOH requires only 280 mV to drive 100 mA/cm^2.[30] The photo and electrochemical catalytic activity of WO_3 has been studied with Mn and V doping. The optimum doping concentration of Mn and V requires only 97 mV and 38 mV for HER to drive 10 mA current density respectively. For photoelectrochemical water splitting, the individual doping of Mn and V produced 1.38 mA/cm^2 and 2.49 mA/cm^2

respectively as compared to pristine WO_3 (0.61 mA/cm^2). The enhancement in catalytic activity with doping arises from the variation in electronic structure and free energy hydrogen adsorption.[31]

1.4.2 Interface engineering

Design of heterostructure for generating additional active sites by tailoring interface electronic structure is a significant strategy for enhancing the catalytic properties of a material.[22] Heterostructure strategy is an important approach for band engineering to modify the surface/interface charge transfer/separation and simultaneously enhance the overall water splitting.[32] Interface engineering has attracted the attention of a lot of researchers for tuning and enhancing the water splitting performance, which provides synergistic interaction at the heterogeneous structure interface.[33-35] The construction of heterogeneous material results in the modification of catalytically active centers which results from strong electronic interactions between the two components. The heterogeneous strategy provides favourable adsorption of reaction intermediates and enhances the overall water splitting kinetics.[34, 35]

For example, Wei *et al.* synthesized a heterogeneous catalyst NiV-LDH/FeOOH, which demonstrated an OER activity of 297 mV @ 100 mA/cm^2 with a long-term stability test for 20 h. The enhancement in current density could be due to the synergistic effect of catalytically active Fe and Ni species and the heterogenous interface between $Ni(OH)_2$ and FeOOH.[36, 37] Three-dimensional FeOOH/NiFe-LDH heterojunction is constructed between poor crystalline NiFe-LDH and crystalline FeOOH by Zou *et al*. which gives an overpotential of 238 mV @ 100 mA/cm^2 for OER with a corresponding Tafel slope value of 28.9 mV/dec. The solid-solid heterostructure interface provides robust electronic interaction between NiFe-LDH and FeOOH which facilitates the intrinsic OER activity.[38] For overall water splitting in the same electrolytic condition, Liu *et al*. constructed a hybrid electrocatalyst by coupling OER and HER catalyst in

a single electrode configuration. The hybrid catalyst FeOOH/Ni_3S_2 nanosheets exhibit an overpotential of 187 mV for OER and 106 mV for HER at 10 mA/cm^2 current density respectively. Based on DFT calculations, the heterostructure interface between FeOOH and NiS_2 has two functional groups of Ni–O–Fe and Fe–S bonds, responsible for accelerating the overall water splitting kinetics.[39] As illustrated by Li *et al*. the CoP/CoOOH/CP heterostructure strategy reduced the energy barrier and provides optimal adsorption energy for reaction intermediates. The fabricated hybrid catalyst CoP/CoOOH/CP required an overpotential of 81 mV (HER) and 200 mV (OER) at 10 mA current density. From the experimental evidence, the core-shell heterostructure interface enhances the durability, accelerates the overall water splitting (OWS) kinetics, and decreases the activation energy.[40] Bai *et al.* synthesized heterojunction WO_3/Fe_2O_3 modified with NiFe LDH to give 3.0 mA/cm^2 which is 5 and 7 times higher as compared to pristine WO_3 and α-Fe_2O_3 respectively.[41] Another heterojunction strategy WO_3/Bi_2S_3 is proposed by Wang *et al.* for PEC water oxidation, which exhibited a photocurrent density of 5.95 mA/cm^2 @ 0.9 V vs RHE.[42] The enhancement in current density is attributed to better charge separation and increase in light absorption.

1.4.3 Morphological modification

Morphological modification is another significant approach to enhance the (photo)electrochemical catalytic activity by shortening the diffusion length of generated charges, enhancing the electrode/electrolyte surface contact, and better exposure of surface-active sites.[43] One-dimensional nanomaterial like nanowires,[44, 45] nanotubes,[46, 47] nanorods, [48, 49] nanoribbons [50, 51] have been investigated for (photo)electrochemical water splitting for their potential in enhancing the catalytic activity, facile charge transport, and better mass transport of active species.[52] Two-dimensional transition metal oxide/hydroxide having a morphology of nanosheets, nanowires, nanoparticles, nanocube, core-shell, etc., due to their high surface area and porosity, facilitates electrode/electrolyte contact and promotes electrolyte penetration for

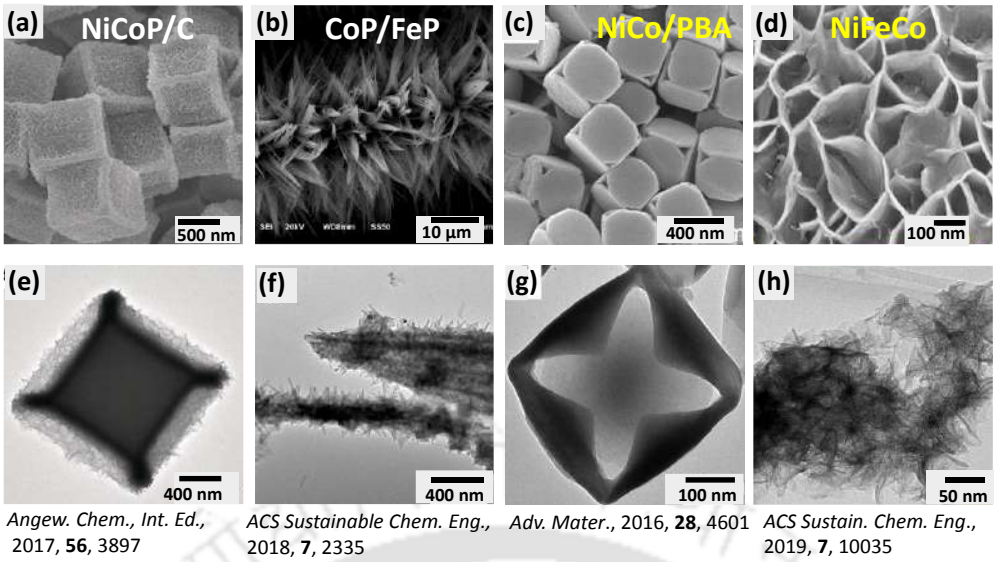

Figure 1.6 Numerous morphological modifications to enhance (photo) electrochemical water splitting.

accelerating the overall water splitting performance.[53] Hollow metal-organic framework (MOF) derived Nanoboxes (NiCoP/C) exhibit good stability and high activity benefitting from their unique structural features and composition. The FESEM image (**Figure 1.6 (a))** indicates uniform nanocubes with a size of ~750 nm and the TEM image in **Figure 1.6 (e)** show that the nanocubes are covered with nanosheet and the NiCoP/C nanoboxes show an overpotential of 330 mV to drive 10 mA current density.[54] Ai *et al.* proposed CoP nanowires arrays modified with FeP nanorods to provide better interfacial contact and to generate a built-in electric field at the heterojunction interface, thereby enhancing the electrocatalytic properties. The hybrid catalyst CoP/FeP requires an overpotential of 71 mV for HER and 250 mV for OER to drive 10 mA/cm^2 current density **(Figure 1.6 (b))**.[55] Ni–Co Prussian-blue-analog (PBA) nanocages was first synthesized by Han *et al.* The Ni–Co PBA mixed metal oxide nanocages in **Figure 1.6 (c)** required a low overpotential of 0.38 V @ 10 mA/cm^2 for OER.[56] 2D NiFeCo LDH electrode required a low overpotential of 210 mV for OER and 108 mV for HER to drive 10 mA current density **(Figure 1.6 (d))**. The high electrocatalytic properties of NiFeCo LDH can be attributed to its porosity and 2D nanosheet structure, which facilitates stability, enhances electric conductivity and electron transport and increases the number of surface-active sites.[57]

1.4.4 Co-catalyst modification

Co-catalyst plays two very important and significant roles, namely, charge separation and electrode/electrolyte surface reaction. The modification of semiconductors with co-catalyst shows an enhancement in charge separation and surface reaction kinetics which contributes to increase in catalytic properties.[58-59] Co-catalyst can be divided into oxidation co-catalyst which trapped holes for oxidation half-reactions, and reduction co-catalyst which trapped electrons for reduction half-reactions. For example, transition metal oxide (CoO_x),[60] metal hydroxide (CoAl LDH),[61] metal phosphide (CoPi)[62] can serve as oxidation co-catalyst, and similarly, transition metal sulfides (NiS),[63] noble metal (Pt),[64] non-noble metal (NiFe LDH),[65] metal selenide ($CoSe_2$),[66] can be utilized as reduction co-catalyst.

Dual co-catalyst modification for PEC water splitting is reported by Chen *et al.* One dimensional Ta_3N_5 is taken as base material and co-modified with CoPi sheet layer at the bottom and covered with $Co(OH)_2$ at the top. The resultant photoanode $Co(OH)_2$/CoPi-Ta_3N_5 exhibits a photocurrent density of 3.8 mA/cm^2 at 1.23 V vs RHE, which is higher as compared to single co-catalyst modification of CoPi-Ta_3N_5 and $Co(OH)_2$-Ta_3N_5.[67]

Heterostructure strategy $BiVO_4$/WO_3 photoelectrode modified with F:FeOOH as hole extractor is studied by Li *et al.* The hybrid photoanode F:FeOOH/$BiVO_4$/WO_3 exhibits superior OER activity of 3.1 mA/cm^2, which is 7 and 9 times higher as compared to pristine WO_3 and $BiVO_4$ respectively. The enhancement in photocurrent density could be attributed to F:FeOOH acting as a hole extractor, thereby promoting the electron and hole separation and enhancing the electron lifetime.[68] Cu_2O nanocubes co-modified with electron extractor NiS and Al with surface plasmon resonance (SPR) effect facilitates the light absorption, charge separation and transfer, which result in a photocurrent density of -5.16 mA/cm^2 @ 0 V vs RHE.[69] The photoanode Cu_2O/CuO composite exhibits enhanced photocurrent stability at mild pH and

gives a photocurrent density of -1.54 mA/cm^2 @ 0 V vs RHE.[70] Zhao *et al.* fabricated $BiVO_4$ photoanode modified with CoMn-LDH as hole extractor which exhibits a photocurrent density 2.69 mA/cm^2 @ 1.23 V vs RHE.[71]

1.5 MOTIVATION AND OBJECTIVES OF THE CURRENT PROJECT

The reported experimental values for PEC are far from the theoretically predicted value of water-splitting. The common cause for poor activity is surface recombination at the electrode/electrolyte interface and bulk recombination. One of the benefits of PEC water splitting is that it requires low potential to split water into hydrogen and oxygen. Meanwhile, the main drawback is the incapability to operate 24 X 7. Electrochemical water splitting is an alternate option to overcome PEC drawback, since electrocatalyst can be operated in dark. For HER and OER, platinum (Pt) and iridium oxide (IrO_2) are used as the global benchmark for electrocatalytic water splitting. The best reported noble metal free (photo)electrocatalyst for OER and HER for practical application based on literature is discussed below. For OER, the heterostructure CF/graphene nanosheets/MoS_2/FeCoNi$(OH)_x$ requires 30 mV @10 mA/cm^2 in 1 M KOH, with excellent stability for about 100 h.[72] For HER, F-anion-doped Ni_3S_2 nanosheet array grown on Ni foam, which exhibits a low overpotential of 38 mV at 10 mA/cm^2 with a Tafel slope of 78 mV/dec and can sustain for 30 h in alkaline electrolyte.[73] Numerous reports has been made on noble metal electrocatalyst, but their high cost and scarcity make it unfavourable for large-scale applications. The search for noble metal free (photo)electrocatalyst for water splitting is a challenging topic for researches. Therefore, the main objectives of the current project are listed under:

1. Fabrication of heterostructure to provide robust synergistic interactions between the components to accelerate the charge transfer and mass transport properties.

2. Synthesis of *in-situ* grown (photo)electrocatalyst directly onto substrate (carbon paper (CP) or fluorine-doped tin oxide (FTO)) to provide better mechanical adhesion and electrical conductivity.
3. Fabrication of noble metal free (photo)electrocatalyst which is stable and robust for practical application.
4. Electronic structure modification by doping with metals having high oxidation state for optimal adsorption of reaction intermediates.
5. Designing of electrocatalyst for HER and OER, which is active in the same electrolytic medium.

1.6 REFERENCES

1. S. Bilgen, *Renewable Sustainable Energy Rev.*, 2014, **38**, 890 —902.
2. D. Gielen, F. Boshell, D. Saygin, M.D. Bazilian, N. Wagner and R. Gorini, *Energy Strat Rev*, 2019, **24**, 38-50.
3. T. Ahmad and D. Zhang, *Energy Rep*., 2020, **6,** 1973-199.
4. Texas gateway for online source, *https://www.texasgateway.org/resource/79-world-energy-use.*
5. Renewable Energy, *https://www.renewable-ei.org/en/statistics/international.*
6. World energy data, *https://www.worldenergydata.org/world-final-energy.*
7. A. K. Verma, *International Journal of Biological Innovations*, 2021, **3**, 331-337.
8. I. Staffell, D. Scamman, A. V. Abad, P. Balcombe, P. E. Dodds, P. Ekins, N. Shah and K. R. Ward, *Energy Environ. Sci.*, 2019, **12**, 463 —491.
9. M. vanderSpek, C. Banet, C. Bauer, P. Gabrielli, W. Goldthorpe, M. Mazzotti, S. T. Munkejord, N. A. Røkke, N. Shah, N. Sunny, D. Sutter, J. M. Trusler and M. Gazzani, *Energy Environ. Sci.*, 2022, **15**, 1034-1077.

10. Renewable Energy Statistics, 2021, *https://www.greenesa.com/article/renewable-energy-statistics*
11. N. L. Panwar, S. C. Kaushik and S. Kothari, *Renewable and Sustainable Energy Reviews*, 2011, **15**, 1513-1524.
12. P. A. Østergaard, N. Duic, Y. Noorollahi, H. Mikulcic and S. Kalogirou, *Renew. Energy* 2020, **146**, 2430–2437.
13. J. H. Kim, D. Hansora, P. Sharma, J.-W. Jang and J. S. Lee, *Chem. Soc. Rev.*, 2019, **48**, 1908 —1971.
14. V. Romano, G. D'Angelo, S. Perathoner and G. Centi, *Energy Environ. Sci.*, 2021, **14**, 5760 —5787.
15. S. Wang, G. Liu and L. Wang, *Chem. Rev*., 2019, **119**, 5192-5247.
16. A. Fujishima and K. Honda, *Nature*, 1972, **238**, 37.
17. J. W. Ager, M. R. Shaner, K. A. Walczak, I. D. Sharp and S. Ardo, *Energy Environ. Sci.*, 2015, **8**, 2811 —2824.
18. P. M. Bodhankar, P. B. Sarawade, G. Singh, A. Vinu and D. S. Dhawale, *J. Mater. Chem. A*, 2021, **9**, 3180 —3208.
19. Y. Yang, S. Niu, D. Han, T. Liu, G. Wang and Y. Li, *Adv. Energy Mater.*, 2017, **7**, 1700555.
20. J. Huang, Y. Jiang, T. An and M. Cao, *J. Mater. Chem. A*, 2020, **8**, 25465 —25498.
21. P. S. Li, X. X. Duan, Y. Kuang, Y. P. Li, G. X. Zhang, W. Liu and X. M. Sun, *Adv. Energy Mater.*, 2018, **8**, 1703341.
22. X. Du, J. Huang, J. Zhang, Y. Yan, C. Wu, Y. Hu, C. Yan, T. Lei, W. Chen and C. Fan, *Angew. Chem., Int. Ed.* 2019, **58**, 4484.
23. Q. Ma, H. Jin, F. Xia, H. Xu, J. Zhu, R. Qin, H. Bai, B. Shuai, W. Huang, D. Chen, Z. Li, J. Wu, J. Yu and S. Mu, *J. Mater. Chem. A*, 2021, **9**, 26852 —26860.

24. H. Xu, C. Shan, X. Wu, M. Sun, B. Huang, Y. Tang and C.-H. Yan, *Energy Environ. Sci.*, 2020, **13**, 2949 —2956.

25. K. Xiong, L. Yu, Y. Xiang, H. Zhang, J. Chen, Y. Gao, *J. Alloy. Compd*., 2022, **912**, 165234.

26. Y. Song, J. Cheng, J. Liu, Q. Ye, X. Gao, J. Lu and Y. Cheng, *Appl. Catal., B*, 2021, **298**, 120488.

27. Y. Sun, K. Xu, Z. Wei, H. Li, T. Zhang, X. Li, W. Cai, J. Ma, H. J. Fan and Y. Li, *Adv. Mater.*, 2018, **30**, 1802121.

28. B. Zhang, J. Shan, X. Wang, Y. Hu and Y. Li, *Small*, 2022, **18**, 2200173.

29. V. K. Singh, U. T. Nakate, P. Bhuyan, J. Chen, D. T. Tran and S. Park, *J. Mater. Chem. A*, 2022, **10**, 9067 —9079.

30. Y. Jin, S. Huang, X. Yue, H. Du, P. K. Shen, *ACS Catal.*, 2018, **8**, 2359– 2363.

31. S. Chandrasekaran, P. Zhang, F. Peng, C. Bowen, J. Huo and L. Deng, *J. Mater. Chem. A*, 2019, **7**, 6161 —6172.

32. S. Shen, S. A. Lindley, X. Chen and J. Z. Zhang, *Energy Environ. Sci.*, 2016, **9**, 2744 —2775.

33. C.-Z. Yuan, K. S. Hui, H. Yin, S. Zhu, J. Zhang, X.-L. Wu, X. Hong, W. Zhou, X. Fan, F. Bin, F. Chen and K. N. Hui, *ACS Mater. Lett.*, 2021, **3**, 752– 780.

34. J. Zhang, Q. Y. Zhang and X. L. Feng, *Adv. Mater.*, 2019, **31**, 1808167.

35. L. Li, P. Wang, Q. Shao and X. Huang, *Chem. Soc. Rev.*, 2020, **49**, 3072 —3106.

36. W. W. Bao, L. Xiao, J. J. Zhang, Z. F. Deng, C. M. Yang, T. T. Ai and X. L. Wei, *Chem. Commun.*, 2020, **56**, 9360 —9363.

37. S. Niu, Y. Sun, G. Sun, D. Rakov, Y. Li, Y. Ma, J. Chu and P. Xu, *ACS Appl. Energy Mater.*, 2019, **2**, 3927 —3935.

38. Y. Liang, J. Wang, D. P. Liu, L. Wu, T. Z. Li, S. C. Yan, Q. Fan, K. Zhu and Z. G. Zou, *J. Mater. Chem. A*, 2021, **9**, 21785 —21791.

39. X. Ji, C. Cheng, Z. Zang, L. Li, X. Li, Y. Cheng, X. Yang, X. Yu, Z. Lu, X. Zhang and H. Liu, *J. Mater. Chem. A*, 2020, **8**, 21199 —21207.

40. B. Zhang, J. Shan, W. Wang, P. Tsiakaras and Y. Li, *Small*, 2022, **18**, 2106012.

41. S. L. Bai, X. J. Yang, C. Y. Liu, X. Xiang, R. X. Luo, J. He and A. Chen, *ACS Sustainable Chem. Eng.*, 2018, **6**, 12906.

42. Y. Wang, W. Tian, L. Chen, F. Cao, J. Guo and L. Li, *ACS Appl. Mater. Interfaces*, 2017, **9**, 40235 —40243.

43. J. Joo, T. Kim, J. Lee, S. I. Choi and K. Lee, *Adv. Mater.*, 2019, **31**, 1806682.

44. Y. Wang, D. Liu, Z. Liu, C. Xie, J. Huo and S. Wang, *Chem. Commun.*, 2016, **52**, 12614 —12617.

45. A. A. Dubale, W.-N. Su, A. G. Tamirat, C.-J. Pan, B. A. Aragaw, H.-M. Chen, C.-H. Chen and B.-J. Hwang, *J. Mater. Chem. A.*, 2014, **2**, 18383 —18397.

46. T. Li, S. Li, Q. Liu, J. Yin, D. Sun, M. Zhang, L. Xu, Y. Tang and Y. Zhang, *Adv. Sci.* 2020, **7**, 1902371.

47. Z. Wu, Z. Wang and F. Geng, *ACS Appl. Mater. Interfaces*, 2018, **10**, 8585 —8593.

48. Y. Liu, Z. Kang, H. Si, P. Li, S. Cao, S. Liu, Y. Li, S. Zhang, Z. Zhang, Q. Liao, L. Wang and Y. Zhang, *Nano Energy*, 2017, **35**, 189 —198.

49. J. R. Jia, M. K. Zhai, J. J. Lv, B. X. Zhao, H. B. Du and J. J. Zhu, *ACS Appl. Mater. Interfaces*, 2018, **10**, 30400 —30408.

50. X. P. Wang, H. J. Wu, S. B. Xi, W. S. V. Lee, J. Zhang, Z. H. Wu, J. O. Wang, T. D. Hu, L. M. Liu, Y. Han, S. W. Chee, S. C. Ning, U. Mirsaidov, Z. B. Wang, Y. W. Zhang, A. Borgna, J. Wang, Y. H. Du, Z. G. Yu, S. J. Pennycook and J. M. Xue, *Energy Environ. Sci.*, 2020, **13**, 229 —237.

51. Z. Wei, X. Hu, S. Ning, X. Kang and S. Chen, *ACS Sustainable Chem. Eng.*, 2019, **7**, 8458 —8465.

52. J. Li and G. Zheng, *Adv. Sci.* 2017, **4**, 1600380.

53. Y. Lian, H. Sun, X. Wang, P. Qi, Q. Mu, Y. Chen, J. Ye, X. Zhao, Z. Deng and Y. Peng, *Chem. Sci.*, 2019, **10**, 464.

54. P. He, X. Y. Yu and X. W. Lou, *Angew. Chem., Int. Ed.*, 2017, **56**, 3897.

55. Z. Niu, C. Qiu, J. Jiang and L. Ai, *ACS Sustainable Chem. Eng.*, 2018, **7**, 2335.

56. L. Han, X. Y. Yu and X. W. Lou, *Adv. Mater.* 2016, **28**, 4601.

57. P. Babar, A. Lokhande, V. Karade, B. Pawar, M. G. Gang, S. Pawar and J. H. Kim, *ACS Sustain. Chem. Eng.*, 2019, **7**, 10035 —10043.

58. S. Bai, W. Yin, L. Wang, Z. Li and Y. Xiong, *RSC Adv.*, 2016, **6**, 57446

59. S. Zhong, Y. Xi, S. Wu, Q. Li, L. Zhao and S. Bai, *J. Mater. Chem. A*, 2020, **8**, 14863 —14894.

60. S. Y. Xiao, Y. Liu, X. F. Wu, L. T. Gan, H. Y. Lin, L. R. Zheng, S. Dai, P. F. Liu and H. G. Yang, *J. Mater. Chem. A.*, 2021, **9**, 14786.

61. C. Wang, X. Long, S. Wei, T. Wang, F. Li, L. Gao, Y. Hu, S. Li and J. Jin, *ACS Appl. Mater. Interfaces*, 2019, **11**, 29799 —29806

62. D. Li, J. Y. Shi and C. Li, *Small*, 2018, **14**, 1704179.

63. Z.F. Liu and M. Zhou, *ACS Sustainable Chem Eng*, 2019, **8**, 512-519.

64. Z. Liu, X. Lu and D. Chen, *ACS Sustainable Chem. Eng.*, 2018, **6**, 10289 —10294.

65. H. Qi, J. Wolfe, D. Fichou and Z. Chen, *Sci. Rep.*, 2016, **6**, 30882.

66. M. Basu, Z.-W. Zhang, C.-J. Chen, P.-T. Chen, K.-C. Yang, C.-G. Ma, C. C. Lin, S.-F. Hu and R.-S. Liu, *Angew. Chem., Int. Ed.*, 2015, **54**, 6211.

67. R. Z. Chen, C. Zhen, Y. Q. Yang, X. D. Sun, J. T. S. Irvine, L. Z. Wang, G. Liu and H. M. Cheng, *Nano Energy*, 2019, **59**, 683.

68. Y. Li, Q. Mei, Z. Liu, X. Hu, Z. Zhou, J. Huang, B. Bai, H. Liu, F. Ding and Q. Wang, *Applied Catalysis B: Environmental*, 2022, **304**, 120995.

69. D. Chen, Z. Liu, Z. Guo, W. Yan and M. Ruan, *Chem. Eng. J.*, 2020, **381**, 122655.

70. Z. Zhang and P. Wang, *J. Mater. Chem.*, 2012, **22**, 2456 —2464.

71. F. Zhao, N. a. Li, Y. Wu, X. Wen, Q. Zhao, G. Liu and J. Li, *Int J Hydrogen Energy*, 2020, **45,** 31902-31912.

72. X. Ji, Y. Lin, J. Zeng, Z. Ren, Z. Lin, Y. Mu, Y. Qiu, J. Yu, *Nat. Commun.*, 2021, **12**, 1380.

73. W. He, L. Han, Q. Hao, X. Zheng, Y. Li, J. Zhang, C. Liu, H. Liu and H. L. Xin, *ACS Energy Lett.*, 2019, **4**, 2905 —2912.

CHAPTER 2

Experimental section

This chapter discusses the comprehensive synthetic protocols of the metal oxides and the co-catalysts, which were employed to show (photo)electrochemical water splitting. It also describes instrumentation techniques used in the characterization of the materials. It displays the complete experimental procedure used in (photo)electrochemical characterization of the catalysts. In this chapter, different performance parameters for photo and electrocatalysts are also discussed in detail.

2.1 INTRODUCTION

The present chapter describe about the chemicals and materials used during the fabrication and synthesis processes. It also describes about the basic instrumental techniques used for characterisation of the synthesized materials. The important parameters for quantifying the performance of the materials are discussed in this chapter.

2.2 CHEMICALS AND MATERIALS USED

Iron chloride ($FeCl_3$), ammonium fluoride (NH_4F), cobalt chloride ($CoCl_2.6H_2O$), cerium nitrate hexahydrate **(**$Ce(NO_3)_3.6H_2O$), urea (CH_4N_2O), tungsten chloride (WCl_6), nickel nitrate hexahydrate ($Ni(NO_3)_2.\ 6H_2O$), ammonium heptamolybdate tetrahydrate ($(NH_4)_6Mo_7O_{24}\cdot\ 4H_2O$), iron (II) sulfate ($FeSO_4$), sodium tungstate dihydrate ($Na_2WO_4\ \cdot\ 2H_2O$), perfluorinated nafion solution (5 wt %), fluorine doped tin oxide (FTO) are purchased from Sigma-Aldrich. Sodium nitrate ($NaNO_3$), hydrochloric acid (HCl) (35−37 %), potassium hydroxide (KOH), hydrogen peroxide (H_2O_2) (30 % w/w in H_2O), sodium sulphate (Na_2SO_4) and isopropanol are all obtained from Merck. Ammonium metavanadate (NH_4VO_3), sodium orthovanadate (Na_3VO_4) and Torey carbon paper from Alfa Aesar. Ruthenium (IV) oxide (RuO_2) and Platinum on carbon (10 % /C) from Sigma Aldrich and thioacetamide (CH_3CSNH_2) is from Himedia and ethanol from TMEDA. Milli-Q water (18.2 MΩ/cm^2) is used for all measurements. All reagents are of analytical grade and used as received.

2.3 MATERIALS CHARACTERIZATION

(1) Powder X-ray diffraction (XRD) is performed on Bruker D2 PHASER X-ray diffractometer with Cu–K_α X-ray generator (λ = 1.54 Å), and on the Rigaku Smart lab X-

ray diffractometer equipped with a Cu K_α (λ=1.54 Å) source with a 9 kW rotating anode at a scan rate of 5°/min within 2θ range from 5° to 80°.

(2) Micro-Raman spectroscopy analysis is performed on Horiba lab Ram HR spectrometer using a solid-state laser source of 488 nm, 514 nm and 633 nm laser excitation.

(3) JASCO Model V-650 and Shimadzu (UV-2600) diffuse reflectance spectrophotometer is used to perform UV-Visible absorption spectra, where $BaSO_4$ was used as reference.

(4) Perkin Elmer (Spectrum-II) instrument is used to perform Fourier transformed infrared spectroscopic (FT-IR) studies using KBr pellet.

(5) Morphology and microstructure of the catalyst are measured by field-emission scanning electron microscope (FESEM, Sigma 300) at 5 kV and transmission electron microscope (TEM, JEOL JEM-2100F) with an operating voltage of 200 kV. Surface elemental mapping is performed on electron dispersive X-ray spectroscopy (EDX, Sigma 300, Zeiss).

(6) The surface elemental composition and electronic environment of an element is determined by X-ray photoelectron spectroscopy (XPS) analysis. The X-ray photoelectron spectroscopy (XPS) is performed by using ESCALAB Xi^+ (Made: Thermo Fisher Scientific Pvt. Ltd., UK) with a monochromated Al K_α ($h\nu$ = 1486.6 eV) and Thermo Scientific (NEXA surface analysis with micro-focused, 72 W, 12 kV) with Al-K_α ($h\nu$ = 1486.6 eV) as X-ray source. All peaks are calibrated with C 1s spectra at 284.7 eV as reference to compensate the charging effect on the surface. XPSPEAK 4.1 software is used to fit and deconvolute the data.

(7) All electrochemical measurements are performed on electrochemical workstation using CHI1120B, CHI760D (Inc., Austin, TX) and Gamry Instrument (Interface1010 E).

(8) Incident photon to current conversion efficiency (IPCE) of photoelectrodes are measured using Newport ORIEL IQE-200 instrument fitted with a 250 W quartz tungsten halogen lamp. Calibrating tungsten halogen lamp by standard Si and Ge diodes.

(9) Online gas chromatography (GC) (Model-7820A, Agilent Technologies) is used to measure Faradaic yield with nitrogen as a carrier gas.

2.4 (PHOTO)ELECTROCHEMICAL MEASUREMENTS

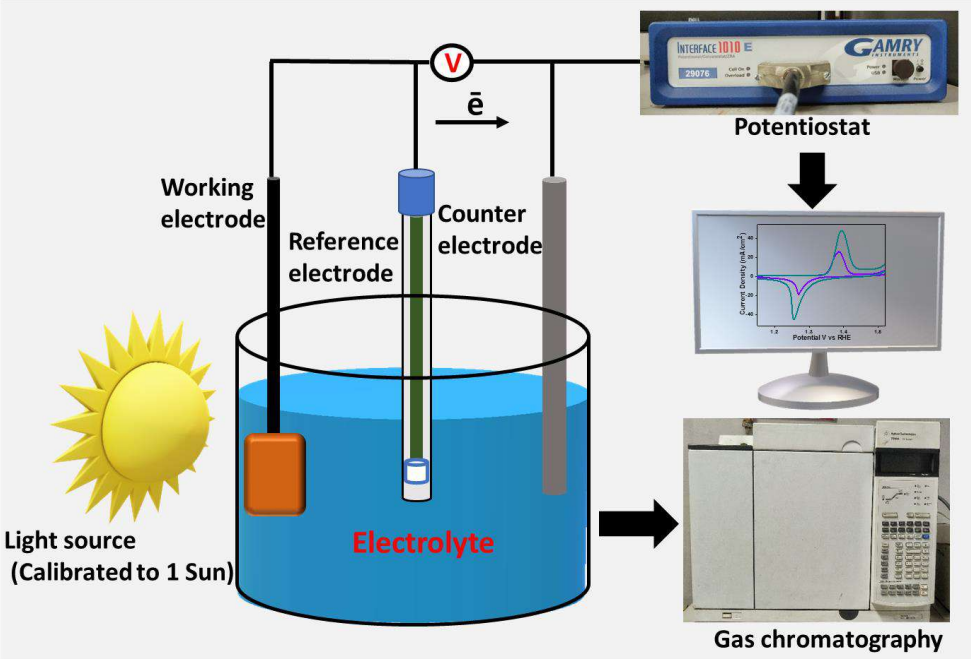

Figure 2.1 Schematic illustration of the experimental setup for (photo)electrochemical water splitting.

Figure 2.1 shows the schematic illustration of the experimental setup for performing (photo)electrochemical water splitting. Electrochemical workstation (CH1120B, CHI760D and Gamry Instrument (Interface1010 E)) is used for all electrochemical characterizations in 0.1 M

Na_2SO_4 **(chapter 3)** and 1M KOH **(chapter 4, 5 & 6)** electrolyte solution in three electrode system. *Insitu*-grown catalysts onto substrate are directly used as working electrodes, platinum rod/graphite rod as the counter electrode, and silver/ silver chloride (Ag/Agcl) and mercury/mercurous oxide (Hg/HgO) as a reference electrode. The electrolyte solution is degassed with N_2 before all the electrochemical measurements to remove dissolved O_2. Before measurements, cyclic voltammetry (CV) is performed for about 100 cycles until a stable CV curve is obtained. Polarization curves are documented at 10 mV/sec in 0.1 M Na_2SO_4 using a light source of 300 W halogen lamp with the light intensity calibrated to 100 mW/cm^2 for the measurements **(chapter 3)**. Mott–Schottky curves are obtained with an AC frequency of 1000 Hz under dark conditions **(chapter 3&4)**. The linear sweep voltammetry (LSV) curves are documented at a scan rate of 5 mV/sec or 10 mV/sec and the Tafel slope is obtained from the corresponding LSV curves. Electrochemical active surface area (ECSA) of the electrodes is obtained by measuring double-layer capacitance (C_{dl}) in the non-Faradaic region. Electrochemical impedance spectroscopy (EIS) measurements are performed in an electrochemical workstation by applying an AC voltage in a frequency range from 100 kHz to 0.01 Hz. For overall water splitting, the as-synthesized electrocatalyst acts as both anode and cathode and the LSV cure is documented in 1M KOH electrolyte solution **(chapter 5&6)**. The durability of the prepared catalyst is evaluated by subjecting to continuous 1000 CV cycles at a scan rate of 20 mV/s, the LSV curves after the 1000 CV cycles are documented again. For assessment, 10 % @ Pt/C and RuO_2 are used as a benchmark for HER and OER respectively. The Faraday yield is measured on online gas chromatography (GC), 7820A Agilent Technologies with nitrogen as a carrier gas. The electrode potential is calibrated to the reversible hydrogen electrode (RHE) according to the Nernst equation.

$$E_{RHE} = E_{Ag/AgCl} + 0.059 \times pH + E^0_{Ag/AgCl} \quad (2.1)$$

Where, E_{RHE} is the potential *vs.* RHE, $E_{Ag/AgCl}$ is the potential measured experimentally *vs.* Ag/AgCl, $E^0_{Ag/AgCl}$ is the standard potential of the Ag/AgCl reference electrode against RHE (0.1976 V) and pH is the pH of the electrolyte solution.

$$E_{RHE} = E^{O}_{Hg/HgO} + 0.059pH + E_{Hg/HgO} \quad (2.2)$$

Where, E_{RHE} is the potential vs. RHE, $E^{O}_{Hg/HgO}$ is the standard potential of Hg/HgO at 25 °C, $E_{Hg/HgO}$ is the experimentally measured potential against the Hg/HgO reference electrode, pH is the pH of electrolyte medium.

2.5 (PHOTO)ELECTROCHEMICAL PERFORMANCE PARAMETERS

2.5.1 Faradaic yield

The Faradaic yield (%) gives the ratio of the experimental and theoretical amounts of evolved gas (H_2 or O_2), according to **Equation (2.4)**, in which *J* represents the experimentally measured current density (mA/cm^2) that is produced during measurement time *t* (s), *A* represents the area of the working electrode (cm^2), *e* is the charge of an electron (1.602x10^{-19} C), and N_A is Avogadro's constant (6.02x10^{23} mol^{-1}). [1]

$$\text{Faradaic yield} = \frac{\text{theoretical gas evolved}}{\text{experimental gas evolved}} = \frac{\text{measured gas evolved}}{\text{the gas evolved based on current}} \quad (2.3)$$

$$= \frac{\text{measured gas evolved}}{\left(\left(\frac{JxAxT}{e}\right)/4\right)/N_A} \text{ x } 100 \quad (2.4)$$

2.5.2 Mott–Schottky analysis

The flat band potential is an important parameter for evaluating the performance of an electrode. Mott−Schottky (M-S) analysis can estimate the band edge position of a new material. M-S is used to calculate the flat-band potential (E_F), and the donor concentration (N_d) (for an n-

type semiconductor), or acceptor concentration, (N_a) (for a p-type).[2] The flat band potential, is the potential at which the electric potential drop at the junction between the electrode surface and the bulk of the semiconductor is zero. Then, the M–S equation can be used to obtain the value of E_F after obtaining the M–S plots. The flat band (E_F) and carrier density (N_D) of the photoelectrodes can be calculated using the following **equation (2.5):**[3]

The flat band (E_{FB}) and charge carrier density (N_D) are calculated according to the following formula:

$$\frac{1}{C^2} = \frac{2}{A^2 N_D e\varepsilon\varepsilon_0}[E - E_{FB} - \frac{kT}{e} \qquad (2.5)$$

where C is the capacitance, N_D is the charge carrier density, ε is the semiconductor relative permittivity, e is the fundamental charge constant, ε_0 is the permittivity of vacuum, E is the applied potential, E_{FB} is the flat band potential, T is the absolute temperature and k is the Boltzmann constant. **Figure 2.2** shows the typical Mott-Schottky (M-S) plot for semiconductor for an n-type and p-type semiconductor.

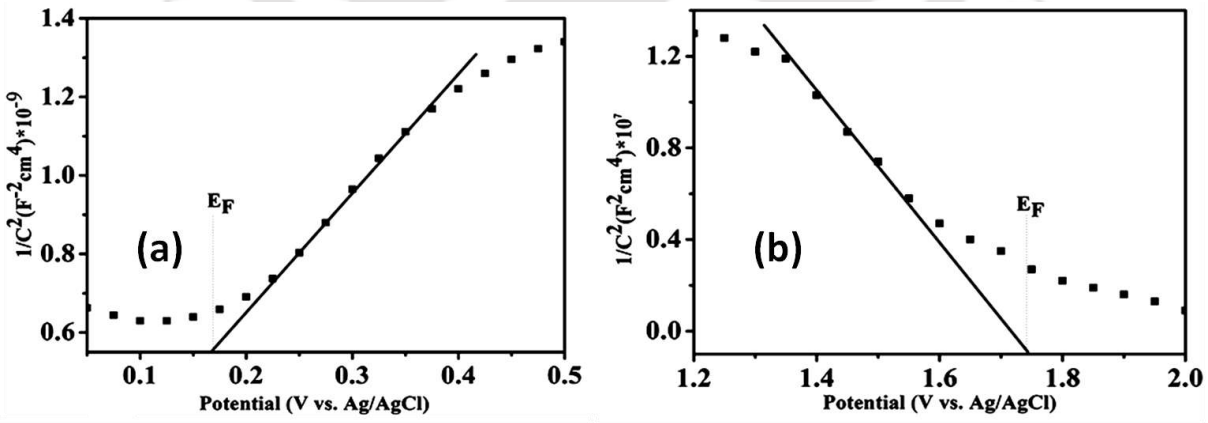

Figure 2.2 Typical Mott-Schottky plot for semiconductor (a) photoanode (n-type), and (b) photocathode (p-type) showing the nature of conductivity.[4]

2.5.3 Electrochemical Impedance Spectroscopy (EIS) Analysis

Electrochemical impedance spectroscopy (EIS) is an important technique to understand the reaction happening at the surface of electrode and electrolyte interface. In principle, impedance is an alternating current (AC) technique in which fixed sinusoidal potential is applied by a potentiostat across a three-electrode system in electrolytic medium. During an EIS measurement, the resulting current response of an electrode to that of the perturbation is recorded, while applying an AC signal with variable frequencies (usually 0.1 Hz < f < 10^6 Hz).[5] From the EIS measurements, Nyquist plots (real vs. imaginary impedance) can be deduced. In **Figure 2.3 (a)**, the X-axis and Y-axis presents real and imaginary impedance respectively, theoretically Nyquist plot gives two semicircle arcs at high and mid-frequency regions. The high frequency region, which is close to the initial point, corresponds to bulk resistance (R_{bulk}), which represent charge transfer resistance

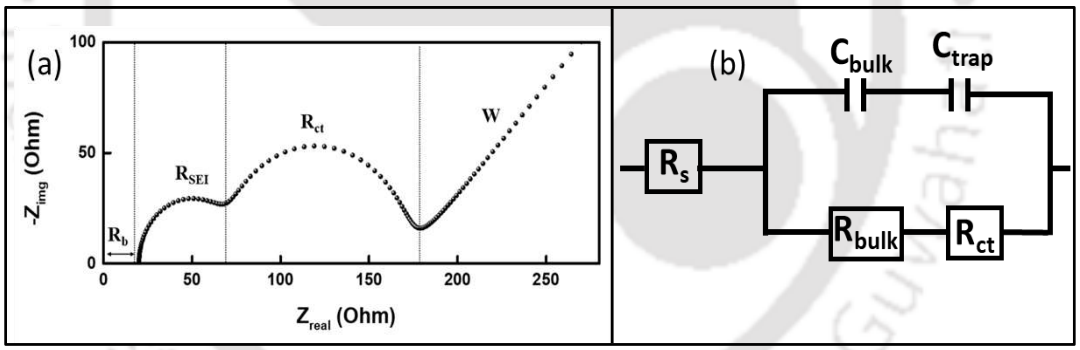

Figure 2.3 (a) Nyquist plot taken from **Ref. 7** and (b) Equivalent Randles circuit diagram to fit the EIS data.

from the valence band/conduction band of electrode to the electrode surface. The semicircle at the mid-frequency region can be assigned to charge transfers between working electrode/electrolyte interface and lower the charge transfers values (R_{ct}) signify a faster charge transfer kinetics at the electrode/electrolyte interface. The Nyquist plot also gives information about the impedance of Nernst diffusion of redox species (R_D). The semicircle arc related with Nernst diffusion takes long duration for analysis to complete and appears at the low frequency region. **Figure 2.3 (b)** show an

equivalent Randles circuit model, important parameters such as solution or contact resistant (R_s), charge transfer resistant (R_{ct}), surface traps state electron (R_{trap}) and capacitance ($C_{trap,}$ and C_{bulk}) can be obtained.[6,7]

2.5.4 Turnover Frequency (TOF)

Turnover frequency (TOF) of electrocatalyst is calculated to assess the intrinsic catalytic active sites. TOF measures the amount of product formed (H_2 in HER or O_2 in OER) per unit time with respect to the amount of reactant consumed at a given potential. The anodic current density values at fixed potential are plotted against various scan rates obtained from the cyclic voltammogram (CV), which gives a linear relationship. To calculate the TOF values of the electrocatalyst, the number of active sites of the electrocatalysts (mol/cm^2) (N_S) can be calculated using the following **equation (2.6)**. [8, 9]

$$Slope(\frac{J_{anodic}}{Scan\ rate}) = n^2F^2AN_S/4RT \qquad (2.6)$$

Where N_S is no. of electrons transferred to generate one mole of product (mol/cm^2), T is the absolute temperature and R is the ideal gas constant. Finally, TOF is calculated using the **equation (2.7)** [8,9]

$$TOF = \frac{J \times A}{n \times F \times N_S} \qquad (2.7)$$

Where j is the current density at fixed overpotential (mA/cm^2), A is the area of the working electrode (cm^2), n is the no. of moles of active material (n=2 for HER, and n=4 for OER), and F is the Faraday constant (96458 C/mol).

2.5.5 Tafel slope

For electrocatalytic water splitting, Tafel slope is used to determine the fundamental activity parameters of an electrocatalyst. Tafel slope signify the kinetics behaviour of the catalytic reaction during the electrochemical processes. The slope of Tafel plot is inversely proportional to

the charge transfer kinetics, so lower is the Tafel slope value faster is the charge transfer kinetics at the electrocatalytic interface. Tafel slope is expressed by **equation (2.8).**[8, 9]

$$\log(i) = \log(i_o) + \frac{\eta}{b} \qquad (2.8)$$

where (η) is the overpotential at fixed current density (i), Tafel slope value is (b) and (i_o) represent the exchange current density.

2.5.6 Incident Photon-to-Current Conversion Efficiency (IPCE) or External Quantum Efficiency (EQE)

Incident photon-to-current conversion efficiency (IPCE) or external quantum efficiency (EQE) is considered to be an important parameter to quantify the activity of photelectrochemical (PEC) water splitting. IPCE can be defined as the number of incident photons to generate excited state electrons by a photoelectrode. IPCE principally determine the light harvesting efficiency of an electrode, which is express by **equation (2.9)**:

$$\text{IPCE} = 1240 \times \frac{J_{sc}}{\lambda \times P_{mono}(\lambda)} \qquad (2.9)$$

Where P_{mono} is the light intensity at each wavelength (λ).

2.5.7 Electrochemically active surface area (ECSA)

Electrochemically active surface area (ECSA) is considered to reveal the actual surface area of the active material which gets exposed to the electrolyte solution. ECSA provides information about the inherent electrocatalytic properties of the material based on their morphology, shape, size and porosity. To measure the ECSA of a material, cyclic voltammetry (CV) is used in the non-Faradaic potential region within a narrow potential with increasing scan rate to calculate the double layer capacitance (C_{dl}). Non faradaic currents arise from the adsorption and desorption of ions in the electrolyte on the surface of the working electrode. The C_{dl} value can

be determined by plotting both the charge and discharge currents against varying scan rate to get 2 C_{dl} from which C_{dl} can be deduced. However, estimation of ECSA from C_{dl} value has disadvantages since the adsorption/desorption sites of an electrode can never be same with each measurement. [8, 10]

2.6 REFERENCES

1. C. Jiang, S. J. Moniz, A. Wang, T. Zhang and J. Tang, *Chem. Soc. Rev.*, 2017, **46**, 4645.
2. A. Hankin, F. Bedoya-Lora, J. Alexander, A. Regoutz and G. Kelsall, *J. Mater. Chem. A*, 2019, **7**, 26162
3. S. P. Berglund, F. F. Abdi, P. Bogdanoff, A. Chemseddine, D. Friedrich and R. van de Krol, *Chem. Mater.*, 2016, **28**, 4231.
4. Y. Feng, C. Liu, J. Chen, H. Che, L. Xiao, W. Gu and W. Shi, *RSC Adv.*, 2016, **6**, 38290.
5. S. Anantharaj and S. Noda, *ChemElectroChem*, 2020, **7**, 2297 —2308.
6. C. Chen, G. Yesilbas, A. Lenz, O. Schneider, A. C. Knoll, In Proceedings of the 46th Annual Conference of the IEEE Industrial Electronics Society (IECON), Singapore, 2020, 3747 –3752.
7. W. Choi, H. C. Shin, J. M. Kim, J. Y. Choi and W. S. Yoon, *J. Electrochem. Sci. Technol.*, 2020, **11**, 1 —13.
8. S. Anantharaj, P. E. Karthik and S. Noda, *Angew. Chem., Int. Ed.*, 2021, **60**, 23051 — 2306.
9. S. Anantharaj, S. Ede, K. Karthick, S. S. Sankar, K. Sangeetha, P. Karthik and S. Kundu, *Energy Environ. Sci.*, 2018, **11**, 744 —771.
10. Y. Wang, H. Arandiyan, K. Dastafkan, Y. Li and C. Zhao, *Chem. Res. Chin. Univ.*, 2020, **36**, 360–365

CHAPTER 3

Enhanced Surface Reaction Kinetics in Vanadium Doped Hematite co-modified by NiFe Layered Double Hydroxide for Electrocatalytic Oxygen Evolution Reaction

The present chapter describe about exploring a low-cost, efficient and stable electrocatalyst to replace noble metal-based catalysts for oxygen evolution reaction (OER) for practical applications. Herein, we have proposed vanadium doping and co-modification of α- Fe_2O_3 utilizing NiFe LDH for noble metal free electrocatalytic oxygen evolution reaction (OER). Vanadium doping enhances the carrier density, whereas NiFe LDH contributes to the surface active sites for promoting water oxidation kinetics. Detailed electrochemical studies with long-term stability indicate the potential of as-synthesized composite α- Fe_2O_3:V-NiFe LDH for utilization as a heterogeneous catalyst for efficient oxygen evolution reaction.

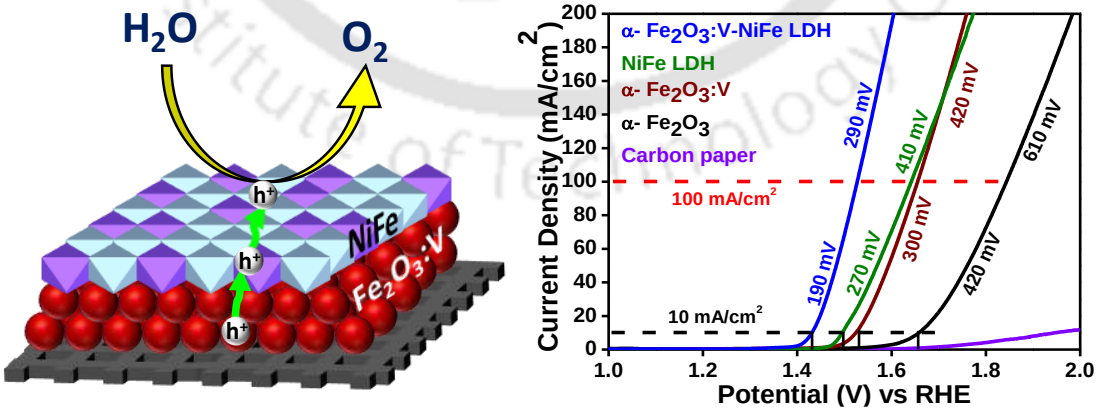

C. T. Moi et al., *Electrochim. Acta,* 2021**, 370,** 137726

3.1 INTRODUCTION

Earth-abundant, highly efficient and stable, binder-free electrocatalysts to address the energy crisis utilizing renewable sources such as water for generating H_2 and O_2 offered a promising alternative. Molecular hydrogen, with its high energy density and environmentally benign, was a modern substitute for traditional fossil fuels.[1,2] The primary bottleneck to cumulative overall energy conversion efficiency utilizing water was that oxygen evolution reaction (OER) comprising of four half-reactions was a thermodynamically uphill process.[3] Benchmark for OER and HER at present were the compounds containing noble metals, such as Iridium Oxide (IrO_2) and Platinum (Pt) with impressive low overpotential and faster kinetics. But these systems suffer from high cost, scarcity and instability in alkaline electrolytes, which hindered their wide practical utilization.[4] For a promising earth-abundant and cost-effective electrocatalysts, numerous attentions have been paid to first-row transition metal alloys, phosphides, sulfides, oxides/hydroxides/oxyhydroxides, doping, etc., for their versatility, abundance and practicality.[4]

Transition-metal oxides were appropriate candidates for electrocatalytic OER activity due to their variable oxidation states, coordination environments, and long-term stability in alkaline conditions.[5] Due to its earth abundance, chemical stability, environmental friendliness, and easy preparation, hematite (α-Fe_2O_3) as a transition metal oxide was a suitable contender for OER activity.[6] However, the sluggish water oxidation kinetics and poor conductivity of α-Fe_2O_3 limits its OER activity. Significant efforts have been worked upon to overcome these barriers, such as incorporating oxygen-evolving cocatalysts (OECs, like 3d metal oxides/hydroxides) to improve the sluggish water oxidation kinetics,[7,8] elemental doping (e.g., Ti, Si, Sn, Ni, V, P, N) to modulate the electronic environment [5,9-11] as well as surface deposition of metal oxides overlayer for passivating the surface defect states.[12,13]

Recently, layered double hydroxides (LDH) have emerged as efficient electrocatalysts for a promising OER in alkaline media.[14] LDH's with easily exchangeable intercalated anions and controllable morphology enhance the exposure of surface active sites, thereby increases the mass transport property and surface reaction kinetics.[14-17] Inspired by these promising ideas, we have synthesized vanadium(V) doped α-Fe_2O_3 via a one-pot hydrothermal method onto low-cost, high conductivity, and high surface area carbon paper. The vanadium doping increased carrier density and modulated electronic interactions. To further enhance the surface reaction kinetics of the electrode material, layered double hydroxide NiFe LDH was electrochemically deposited over the surface of *in-situ* grown vanadium doped α-Fe_2O_3. Notably, α- Fe_2O_3:V-NiFe LDH exhibited excellent OER activity of 190 mV overpotential (η_{OER}) @ 10 mA/cm^2 in contrast to bare α- Fe_2O_3 (420 mV) with corresponding Tafel slopes of 42 mV/dec and 106 mV/dec for α- Fe_2O_3:V-NiFe LDH and α- Fe_2O_3 respectively, in 1M KOH. Present work highlights the design of low cost and highly stable hematite with enhance electroactive sites and surface oxidation kinetics which surpasses the benchmark for OER catalyst, RuO_2 (350 mV @ 10 mA/cm^2) under similar experimental conditions.[18]

3.2 EXPERIMENTAL SECTION

3.2.1 Synthesis of α-Fe_2O_3 and α-Fe_2O_3:V

α-Fe_2O_3 nano particles were directly grown onto carbon paper following the reported procedure.[12] In a typical synthesis, 0.15M $FeCl_3$ and 1M $NaNO_3$ were dissolved in 60 mL distilled water in 100 mL Teflon lined vessel, concentrated HCl was added to maintain the pH at 1.5 under continuous stirring. Different atomic weight % of NH_4VO_3 was added to the above solution for different doping concentrations of vanadium and hydrothermally treated at 160 °C for 6 hours in the presence of carbon paper. The amount of catalyst deposited on the carbon paper was about ~3 mg

3.2.2 Electrochemical deposition of NiFe LDH on α -Fe_2O_3:V

Electrochemical deposition of NiFe-LDH onto α- Fe_2O_3:V was performed following a reported procedure.[19] Herein, a three-electrode configuration was utilized in which α- Fe_2O_3:V directly grown onto carbon paper was the working electrode, Pt wire as the counter electrode, and a Ag/AgCl as the reference electrode. The electrolyte solution consists of 0.15 M of $Ni(NO_3)_2.6H_2O$ and 0.15 M of $FeSO_4.6H_2O$ dissolved in 50 mL deionized water under continuous purging with N_2 to prevent the oxidation of Fe^{2+} and to remove the dissolved oxygen. The deposition time was 50 s at 1.0 V vs Ag/AgCl and the resulting electrode after deposition was cleaned with distilled water and ethanol. **Scheme 3.1** shows the schematic illustration of the fabrication processes of α- Fe_2O_3:V-NiFe LDH.

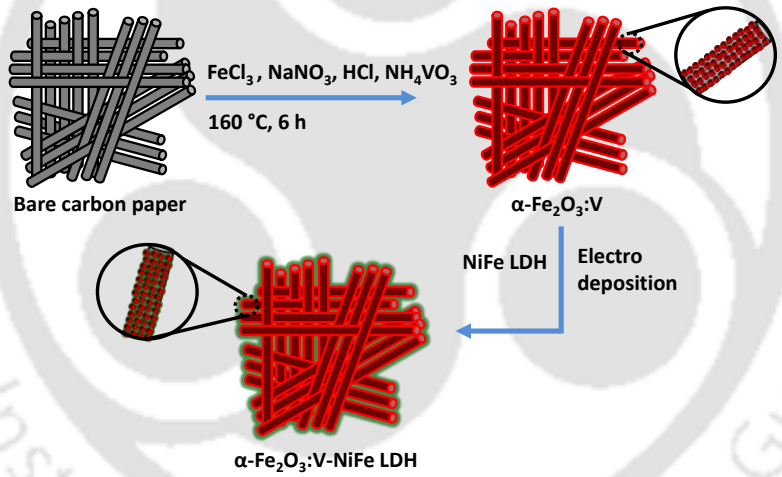

Scheme 3.1 Schematic Illustration of the fabrication processes of α- Fe_2O_3:V-NiFe LDH.

3.3 RESULTS AND DISCUSSIONS

3.3.1 Powder X-Ray Diffraction (PXRD) and Raman Analysis

Thin-film XRD of α- Fe_2O_3, α- Fe_2O_3:V, NiFe LDH, α- Fe_2O_3:V-NiFe LDH were shown in **Figure 3.1 (a)**. Diffractograms in **Figure 3.1 (a)** can be assigned to the α-phase of Fe_2O_3 (JCPDS-01-071-5088), wherein peaks were indexable to (104), (110), (113), (024), (214) and (300).[20] Besides α- Fe_2O_3 diffraction peaks, no significant peaks of NiFe LDH were

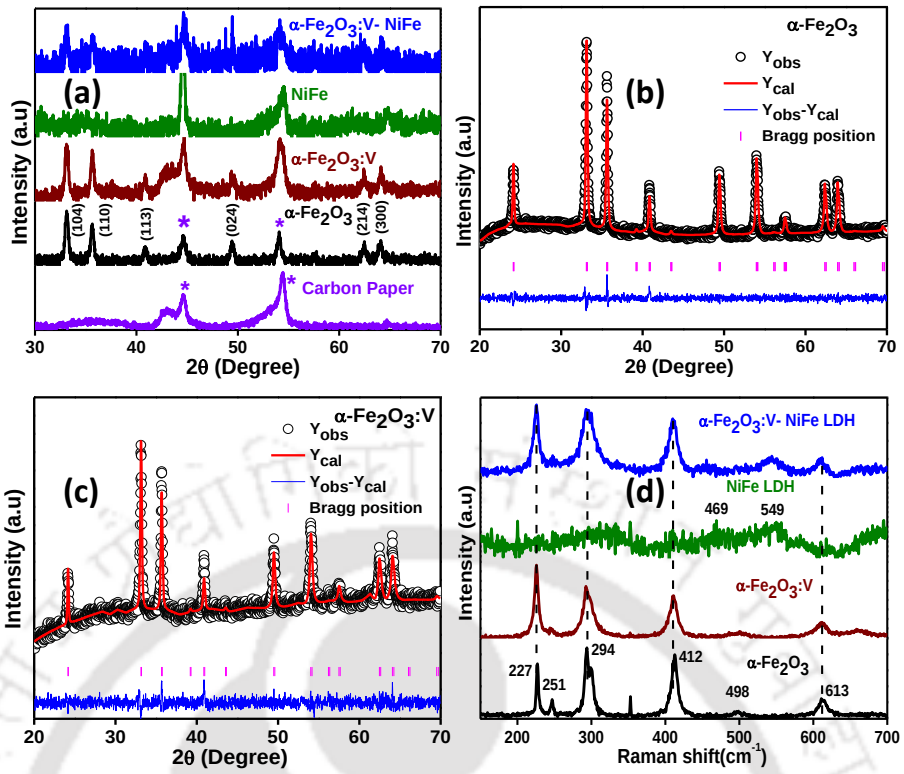

Figure 3.1 (a) XRD patterns of α- Fe_2O_3, α- Fe_2O_3:V, NiFe LDH, α- Fe_2O_3:V-NiFe LDH, * = Carbon paper peak. Rietveld refinement diffraction patterns of powder samples of (b) α- Fe_2O_3 and (c) α- Fe_2O_3:V. The black circular data points represent the original data, red line passing through the black circle points indicates the calculated profile. The blue line indicates the difference between the observed and calculated patterns. The tick vertical pink marks represent Bragg position. (d) Raman spectra of α- Fe_2O_3, α- Fe_2O_3:V, NiFe LDH, α- Fe_2O_3:V-NiFe LDH.

observed. Rietveld refinement of the PXRD data of α- Fe_2O_3 and α- Fe_2O_3:V were shown in **Figure 3.1 ((b)-(C))**. The patterns in **Figure 3.1 ((b)-(C))** shows that the compound forms into the Al_2O_3 type rhombohedral structure with the hexagonal system in the space group, *R*−3c. The calculated PXRD pattern was in good agreement with the experimental one.[21] The agreement of Rietveld refined data was evaluated with initial parameters in relation to the weighted and expected residual factors (R_{wp}, R_{ex}), and their ratio, corresponding to the goodness-of-fit (χ^2). The weighted-profile R value, R_{wp} was defined as

$$R_{wp} = \{\Sigma_i w_i [y_i (obs) - y_i (calc)]^2 / \Sigma_i w_i [y_i (obs)]^2\}^{1/2} \qquad \textbf{(3.1)}$$

where y_i *(obs)* was the observed intensity at step *i*, y_i *(calc)* the calculated intensity, and w_i the weight. The expected R value, R_{exp} was defined as

$R_{exp} = [(N-P)\ \Sigma_i^N\ w_i\ y_i\ (obs)^2]^{1/2}$ **(3.2)**

Where, N and P correspond to the number of observations and parameters respectively.

Table 3.1. From Rietveld refinement the obtained lattice parameters of undoped and V doped α-Fe_2O_3 were tabulated below.

Sample	a (Å)	c (Å)	Volume ($Å^3$)	R_{wp}	R_{ex}	χ^2
α-Fe_2O_3	5.0355	13.7683	302.3415	17.0	12.9	1.73
α-Fe_2O_3:V (1.1 at. wt. %)	5.0309	13.7759	301.849	21.5	15.68	1.87
α-Fe_2O_3:V (2.2 at. wt. %)	5.0308	13.7750	301.841	26.3	23.81	1.22
α-Fe_2O_3:V (3.3 at. wt. %)	5.0377	13.8010	303.3189	33.5	23.88	1.96

In **Table 3.1**, the calculated parameters of α- Fe_2O_3 and α- Fe_2O_3:V, were tabulated, which shows a close proximity to the reported values. The decreases in the unit cell parameters of α- Fe_2O_3:V (a= 5.031 Å, c= 13.775 Å) compared to the bare α- Fe_2O_3 (a= 5.035 Å, c= 13.768 Å) has been observed. Vanadium doping leads to a decreases of unit cell volume from 302.34 $Å^3$ to 301.84 $Å^3$ owing to substitution of Fe^{3+} (r= 0.64 Å) for V^{5+} (r= 0.59 Å). This observation confirms the vanadium doping into the α- Fe_2O_3 crystalline structure.[21, 22]

To understand the electronic interactions among the components, Raman spectroscopy was performed as shown in **Figure 3.1 (d)**. Peaks at 227 cm^{-1} and 498 cm^{-1} corresponds to A_{1g} vibrational modes and peaks at 251, 294, 412 and 613 cm^{-1} corresponds to E_g vibrational modes of α- Fe_2O_3.[11] With the electrodeposition of NiFe LDH, additional peaks at 469 cm^{-1} and 549 cm^{-1} were observed, which corresponds to the vibrational mode of NiFe LDH and confirms the presence of NiFe LDH in the composite.[4, 16]

3.3.2 X-Ray Photoelectron Spectroscopy (XPS) Analysis

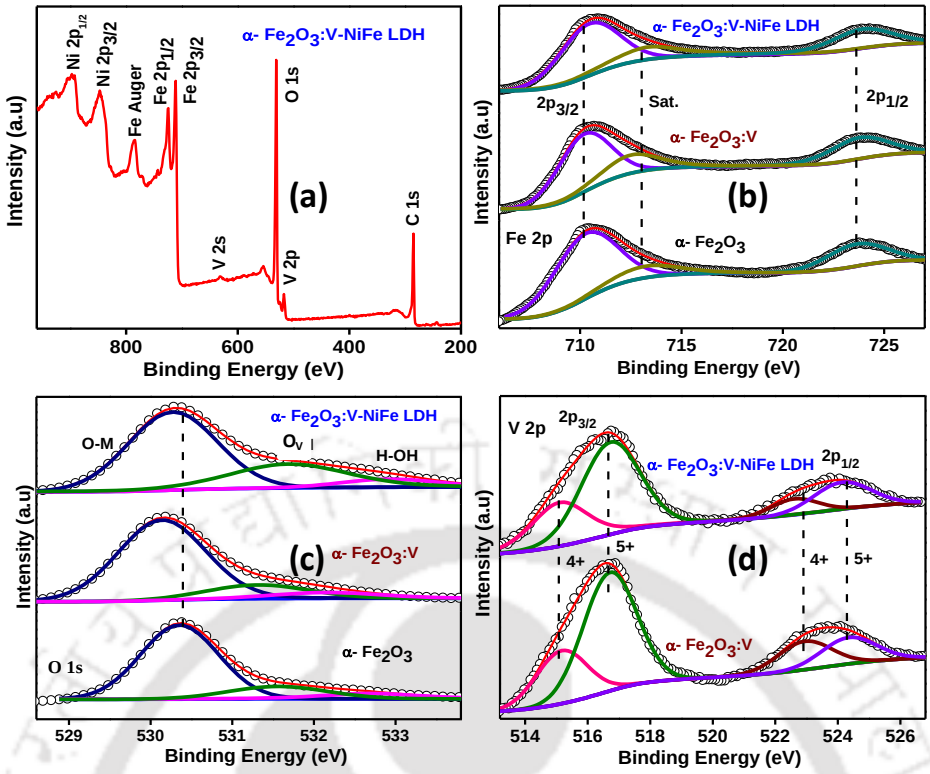

Figure 3.2 XPS survey spectra of (a) α- Fe_2O_3:V-NiFe LDH, high-resolution XPS spectra of (b) Fe 2p, (c) O 1s of α- Fe_2O_3, α- Fe_2O_3:V, α- Fe_2O_3:V-NiFe LDH and (d) V 2p spectra of α- Fe_2O_3:V, α- Fe_2O_3:V-NiFe LDH.

The surface and chemical state of the samples were examined by XPS analysis. Peaks were calibrated at 284.7 eV with respect to C1s. The survey spectrum of α- Fe_2O_3:V-NiFe LDH **(Figure 3.2 (a))** shows that all the elements were present in the composite. In **Figure 3.2 (b)**, two distinct peaks at 710.2 eV and 723.6 eV correspond to Fe $2p_{3/2}$ and Fe $2p_{1/2}$, with a shakeup satellite peak at 713.2 eV, which was characteristic peak for the presence of Fe^{3+} for Fe 2p core-level spectra of α- Fe_2O_3. The peaks of Fe 2p spectra for α- Fe_2O_3:V and α- Fe_2O_3:V-NiFe LDH **(Figure 3.2 (b))** were observed at 710.4 eV and 724.0 eV, corresponding to Fe $2p_{3/2}$ and Fe $2p_{1/2}$, respectively, with a satellite peak at 713.3 eV.[5,11]. The shift towards higher binding energy with vanadium doping demonstrate a reduced electron density at the Fe 2p center due to the electron transfer from Fe to V, which is in agreement with former reports.[10,13,23-26] The O 1s core-level spectrum of α- Fe_2O_3 shown in **Figure 3.2 (c)** was deconvoluted into peaks located at 530.3 eV, 531.5 eV and 532.7 eV, corresponding to lattice oxygen (M−O), O_x^- ions caused by defect sites due to oxygen vacancies (O_v), and a shoulder peak of surface adsorbed water

molecules, respectively. The peaks **(Figure 3.2 (c))** at binding energy of 530.2 eV, 531.4 eV and 532.3 eV were observed for O 1s core-level spectra of α- Fe_2O_3:V and α- Fe_2O_3:V-NiFe LDH.[5, 16] The O 1s spectra of α- Fe_2O_3:V and α- Fe_2O_3:V-NiFe LDH were shifted towards lower binding energies, which indicates an interaction between the dopants and α- Fe_2O_3. The peak area for oxygen defect sites increased by ~1.5 fold for α- Fe_2O_3:V compared to α- Fe_2O_3 caused by the non-stiochiometetry with V^{4+}/V^{5+} doping at Fe^{3+} site. The V 2p signals of α- Fe_2O_3:V **(Figure 3.2 (d))** for V^{4+} were observed at 515.2 eV and 523.0 eV and V^{5+} at 516.7 eV and 524.3 eV, which corresponds to V $2p_{3/2}$ and V $2p_{1/2}$ respectively. The binding energy values of V $2p_{3/2}$ and V $2p_{1/2}$ of V^{4+} at 515.1 eV and 522.6 eV and of V^{5+} at 516.6 eV and 524.1 eV, respectively, were observed for α- Fe_2O_3:V-NiFe LDH. The shifts towards lower binding energy in V 2p spectra with NiFe LDH deposition was an indication of electron transfers to the LDH surface facilitating a better water oxidation kinetics. [10, 23]

3.3.3 Morphological Analysis

Morphological analysis of hydrothermally grown α- Fe_2O_3 in **Figure 3.3 (a)** shows uniformly grown spherical nanoparticles onto carbon fiber of the substrate. **Figure 3.3 (b)** shows the FETEM images of the composite, α- Fe_2O_3:V-NiFe LDH, indicating that a layer of NiFe LDH covered α- Fe_2O_3 nanoparticles. In **Figure 3.3 (c)**, HRTEM image further confirms the presence of the components with distinct inter-planar d-spacing of 0.25 nm and 0.27 nm corresponding to (110) plane of α-Fe_2O_3 and (101) plane of NiFe LDH, respectively. **Figure 3.3 ((e)-(h))** shows the FETEM-EDS mapping, where the presence of elements, Fe, O, V and Ni were confirmed.[11,15]

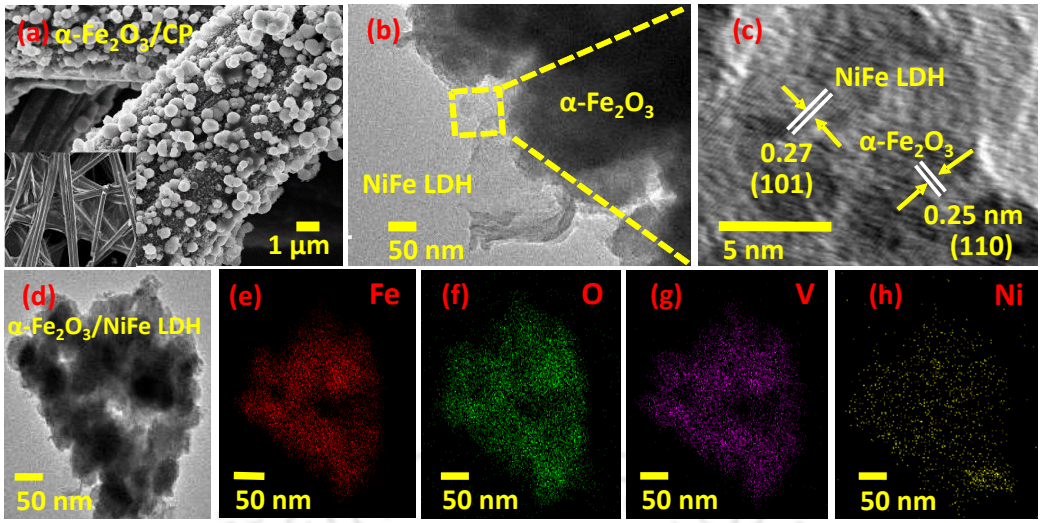

Figure 3.3 (a) Field Emission Scanning Electron Microscopy (FESEM) image of α- Fe_2O_3@carbon paper (b) Field Emission Transmission Electron Microscopy (FETEM) image of α- Fe_2O_3:V-NiFe LDH (c) High Resolution Transmission Electron Microscopy (HRTEM) images of α- Fe_2O_3:V-NiFe LDH, (d) FETEM image of α- Fe_2O_3:V-NiFe LDH and (e) – (h) corresponding EDS mapping analysis for α- Fe_2O_3:V-NiFe LDH composite

3.3.4 Electrochemical Measurements

The electrochemical OER performance of as-prepared electrocatalyst was examined via linear sweep voltammetry (LSV). From the polarization curve, the anodic current was measured at a scan rate of 10 mV/sec in a three-electrode configuration in 1M KOH. The electrolyte solution was continuously purged with N_2 gas for about 30 minutes to remove the dissolved oxygen, and the hydrothermally grown electrode material onto carbon paper was directly used as the working electrode. As shown in **Figure 3.4 (a)**, α- Fe_2O_3:V-NiFe LDH required 190 mV overpotential (η_{OER}) to drive 10 mA/cm^2 current density which was distinctly low compared to the bare α- Fe_2O_3 (420 mV), RuO_2 (360mV), α- Fe_2O_3:V (300 mV) and NiFe LDH (270 mV). OER performance of α- Fe_2O_3:V-NiFe LDH surpasses the best-reported complex oxide systems such as $CoFe_2O_4$ (270 mV) and NiFe LDH/FeOOH (208 mV), as shown in **Figure 3.4 (d)**.[18,27-36] Corresponding Tafel slopes were calculated to signify the intrinsic properties such as reaction kinetics of the electrocatalytic materials.[27] In **Figure 3.4 (b)** the Tafel slopes of 42 mV/dec,

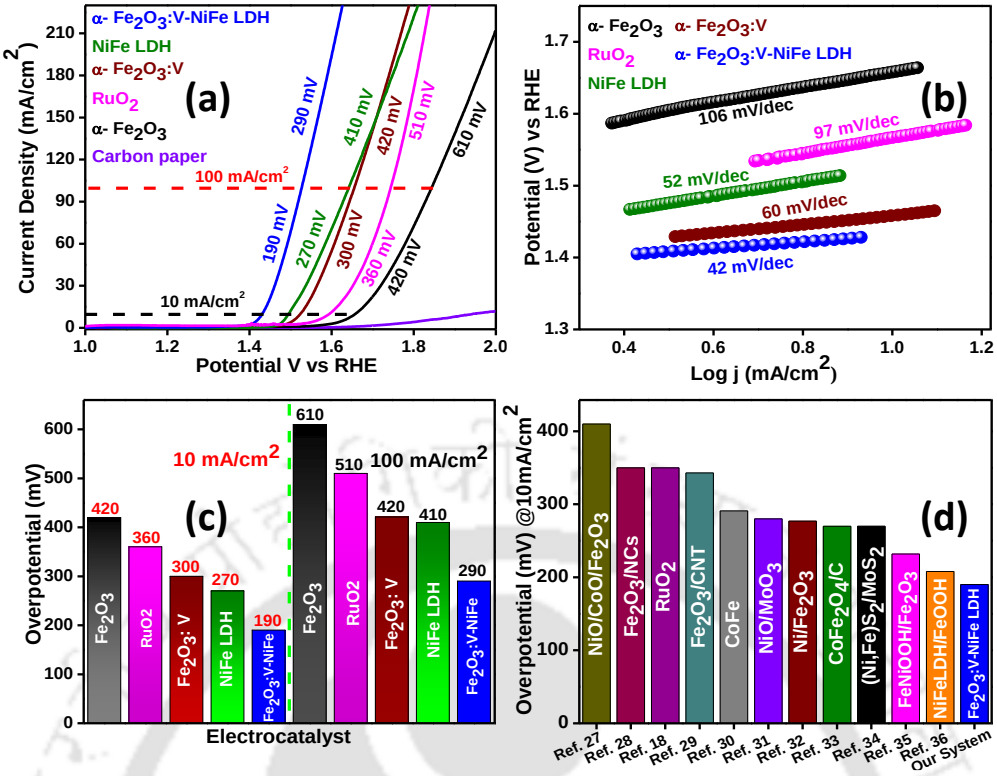

Figure 3.4 (a) Current density – Voltage (J-V) curve of α- Fe_2O_3, RuO_2, α- Fe_2O_3:V, NiFe LDH, α- Fe_2O_3:V-NiFe LDH at a scan rate of 10 mV/s in 1M KOH electrolyte solution and (b) Tafel slope of α- Fe_2O_3, RuO_2, α- Fe_2O_3:V, NiFe LDH, α- Fe_2O_3:V-NiFe LDH, (c) Comparison graph of as-prepared catalysts at 10 mA/cm^2 and 100 mA/cm^2 current density and (d) Comparison graph of overpotential for different electrocatalyst at 10mA/cm^2 current density.

52 mV/dec, 60 mV/dec, 97mV/dec and 106 mV/dec correspond to α- Fe_2O_3:V-NiFe LDH, NiFe LDH, α- Fe_2O_3:V, RuO_2 and α- Fe_2O_3, respectively, indicate faster oxidation kinetics in the composite as compared to the bare counterpart. The OER activity of bare carbon paper was found to be negligible (**Figure 3.4 (a)**). Vanadium doping in hematite enhanced charge carrier density and facilitates the charge transport throughout the film, and NiFe LDH with its rich ionic surface –OH group and inherent positive charge provides better electrostatic interaction.[23, 27-29] To further prove the kinetics of the electrode material, devices were probed at high current density (@ 100 mA/cm^2). Composite α- Fe_2O_3:V-NiFe LDH requires relatively small overpotential of 290 mV to drive 100 mA/cm^2, as compared to bare α- Fe_2O_3 (610 mV), α- Fe_2O_3:V (420 mV) and NiFe LDH (410 mV) as shown in **Figure 3.4 (c)**. These results indicate better kinetics of the electrode due to lower activation energies for the formation of reaction

intermediates. The OER performance of α- Fe_2O_3:V-NiFe LDH surpassed that of a noble metal oxide such as RuO_2 as shown in **Figure 3.4 (d)**. To understand the role of vanadium doping in hematite for an increased in current density, the polarization curve of undoped α- Fe_2O_3-NiFe LDH was measured.

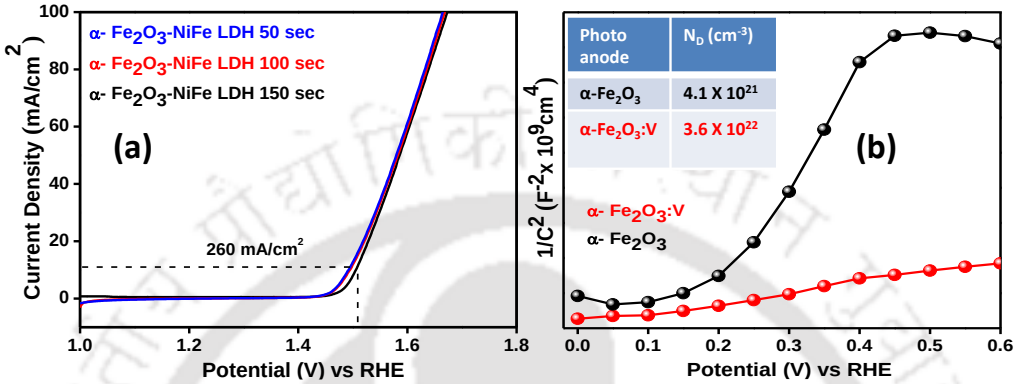

Figure 3.5 (a) Current Voltage curve of α- Fe_2O_3-NiFe LDH with different deposition time of NiFe LDH at 1.0 V vs Ag/AgCl and (b) Mott–Schottky plot documented in the dark for α- Fe_2O_3 and α- Fe_2O_3:V in 1M KOH.

As shown in **Figure 3.5 (a)**, α- Fe_2O_3-NiFe LDH required 260 mV to drive 10 mA/cm^2 current density, while vanadium doped α- Fe_2O_3:V-NiFe LDH required only 190 mV@ 10 mA/cm^2. Vanadium doping enhances charge carrier density on hematite, as doping with high valence state of vanadium in V^{4+} and V^{5+} oxidation states increase the electron concentration of α- Fe_2O_3, by acting as donor dopants.[30] To better understand the effects of vanadium doping on the electronic properties of α- Fe_2O_3, Mott‑Schottky (M‑S) measurements were carried for α- Fe_2O_3 and α- Fe_2O_3:V. As shown in **Figure 3.5 (b)**, both the films showed positive slopes, an indicative of n-type semiconductors with electrons as the majority charge carriers. The vanadium doped hematite with a smaller slope reflects higher carrier concentrations, donor densities calculated for α- Fe_2O_3 and α- Fe_2O_3:V were 4.1 x 10^{21} and 3.6 x 10^{22}, respectively. Thus, the increased activity α- Fe_2O_3:V could be attributed to the increase in carrier concentration and hence the enhanced OER performance.

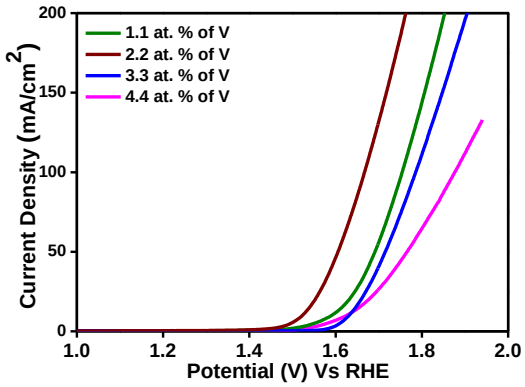

Figure 3.6 Current Voltage curve of α- Fe_2O_3:V with different atomic weight % of vanadium doping.

Figure 3.6 shows the optimization curve of different atomic weight % of the vanadium in bare hematite, in which there was a continuous increase in current density from 1.1 at. wt. % to 2.2 at. wt. % of vanadium doping. With a further increase in the concentration of vanadium doping to 3.3 at. wt. %, a decrease in current density was observed. The decreases in current density could be due to segregation of the dopant phase, which can serve as recombination centers and thus inhibits the electrochemical activity.[25]

3.3.5 Cyclic voltammetry (CV) and Electrochemical surface area (ECSA)

Electrochemical surface area (ECSA) reflects the adsorption/desorption abilities of an electrocatalyst and the exposure of active surface sites. ECSA of an electrocatalyst can be estimated by measuring the double-layer capacitance (C_{dl}) value. C_{dl} can be estimated from the difference in current densities between the anodic and cathodic sweeps (J_{anodic} - $J_{cathodic}$) at corresponding potential vs. RHE and plotted against the scan rate in which the resulting slope was equal to the twice of the C_{dl} value of the catalyst.[33-35]

CV measurements were done in the range of 0.98 V to 1.15 V vs. RHE at different scan rates ranging between 10 to 100 mV/sec in 1M KOH electrolyte solution, as shown in **Figure 3.7 ((a)-(c))**. In **Figure 3.7 (d)**, highest C_{dl} value was obtained for α- Fe_2O_3:V-NiFe LDH

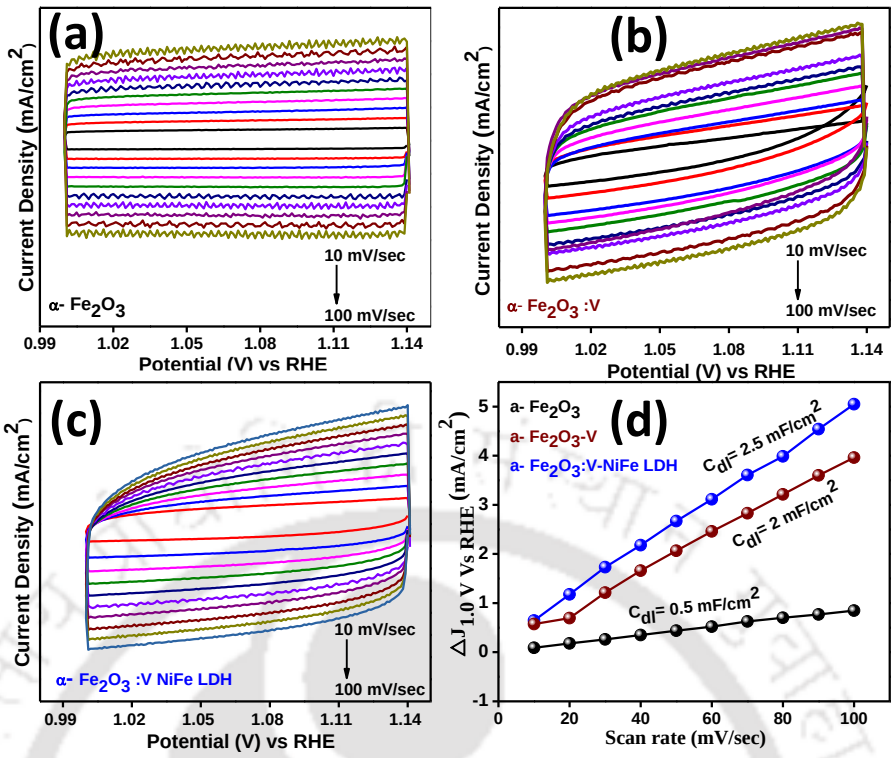

Figure 3.7 Cyclic voltammograms of (a) α- Fe_2O_3, (b) α- Fe_2O_3:V, (c) α- Fe_2O_3:V-NiFe LDH measured at different scan rate from 10 to 100 mV/sec in potential range of 0.98 V to 1.15 V vs RHE in 1M KOH electrolyte solution and (d) Plot of current density vs scan rate at 1.06 V vs RHE of α- Fe_2O_3, α- Fe_2O_3:V, α- Fe_2O_3:V- NiFe LDH.

electrode (2.5 mF/cm^2), compared to the bare α- Fe_2O_3 (0.5 mF/cm^2) and α- Fe_2O_3:V (2 mF/cm^2), respectively. The enhancement in C_{dl} values on vanadium doping and with the deposition of highly surface reactive NiFe LDH suggests an increased number of catalytic surface-active sites and better exposure of active sites at the surface. The large ECSA was beneficial for water molecule adsorption/desorption and close contact with the electrolyte, which accounts for the accelerated diffusion and adsorption of electrolytes and gaseous products, and facilitates the charge transfer.[32, 33]

3.3.6 Electrochemical Impedance Spectroscopy (EIS) and Turnover Frequency (TOF)

To further understand the oxidation kinetics of the electrocatalyst, electrochemical impedance spectroscopy (EIS) was performed, as shown in **Figure 3.8 (a)**. The Nyquist plots were fitted to an equivalent Randles circuit (**Figure 3.8 (a)**) and the desired parameters were

deduced. Smaller semicircle was for α- Fe_2O_3:V-NiFe LDH (3 Ω) electrode which exhibits a much lesser charge transfer resistant (R_{ct}) against α- Fe_2O_3 (115 Ω) and α- Fe_2O_3:V (56 Ω). Lower series resistant (R_s) value for α- Fe_2O_3:V-NiFe LDH indicates an excellent ohmic contact between the electrode and carbon paper.[30] The superior charge-transfer kinetics and enhancement in more surface active sites of α- Fe_2O_3:V-NiFe LDH contributes to the higher OER activity of the electrode.[23,34]

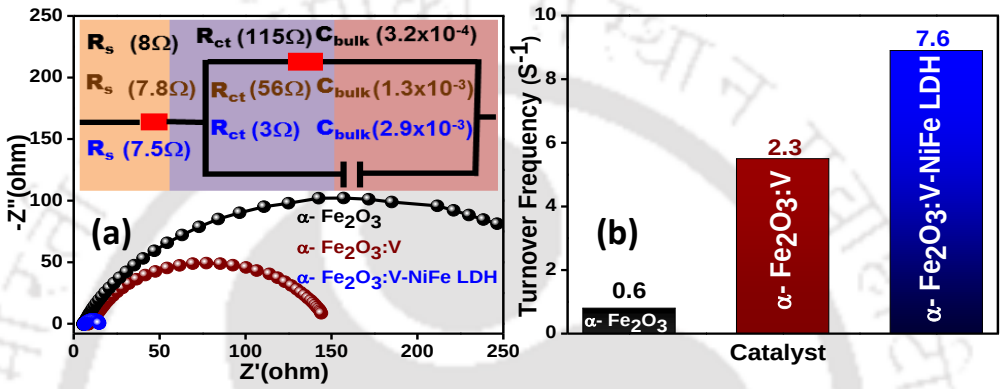

Figure 3.8 (a) Nyquist plots of α- Fe_2O_3, α- Fe_2O_3:V, α- Fe_2O_3:V-NiFe LDH in 1M KOH electrolyte solution and (b) Turnover frequency (TOF) of α- Fe_2O_3, α- Fe_2O_3:V, α- Fe_2O_3:V-NiFe LDH.

To better understand the intrinsic activity of the catalytic centers, turnover frequency (TOF) was measured. TOF was derived from the number of moles of O_2 produced per unit time per unit active site. The TOF was calculated using the following equation,

$$TOF = \frac{J \times A}{4 \times F \times N_S} \qquad \textbf{(3.3)}$$

Where, J correspond to current density at a certain overpotential (A/cm^2), A was the surface area of the working electrode (cm^2), F was the Faraday constant (96485 C/mol), and N_S was the concentration of active sites in the catalysts (mol/cm^2) calculated from cyclic voltammetry at different scan rates. The peak current was plotted against scan rate where the slope has a linear relationship,

$$Slope = n^2F^2AN_S/4RT \qquad \textbf{(3.4)}$$

where n, R, and T were, respectively, the number of electrons transferred, ideal gas constant and absolute temperature.[35,36]

The TOF values calculated at a current density of 1.6 V of α- Fe_2O_3:V-NiFe LDH (7.6/s) was much higher as compared to α- Fe_2O_3:V (2.3/s) and α- Fe_2O_3 (0.6/s) (**Figure 3.8 (b)**). The ~12 fold increase in TOF values from bare α- Fe_2O_3 to α- Fe_2O_3:V-NiFe LDH indicates efficient utilization of surface active sites between the NiFe LDH interlayers.[37] The upsurge in TOF value also shows that co-modification of bare hematite with vanadium doping and NiFe LDH deposition plays an essential role in facilitating the kinetics of OER and enhancing the intrinsic activity.[33]

3.3.7 Electrochemical Stability

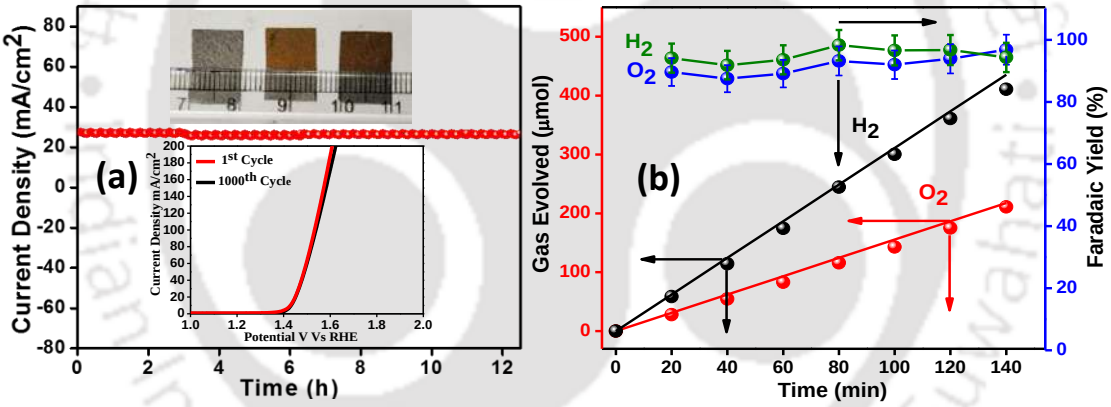

Figure 3.9 (a) Stability test of α- Fe_2O_3:V-NiFe LDH with the inset showing the LSV curve before and after 1000 CV cycles and the inset showing digital image of bare Carbon paper(Left), α- Fe_2O_3 (middle), α- Fe_2O_3:V-NiFe LDH (Right) and (b) Faradaic yield of α- Fe_2O_3:V-NiFe LDH measured using online gas chromatography at a current density of 10 mA/cm^2. In the graph (▬) symbolizes the theoretical yield of O_2 gas, (●) symbolizes the experimental yield, (▬) symbolizes the theoretical H_2 yield and (●) symbolizes the experimental yield of H_2 gas. The Faradaic yield of O_2 gas evolved was represented by (●) and that of H_2 by (●).

The durability and chemical stability of an electrocatalyst was a critical parameter in its practical applicability. **Figure 3.9 (a)** shows the durability of α- Fe_2O_3:V-NiFe LDH obtained from the chronoamperometry measurement, which was carried out for 12 hours at a fixed current density of 25 mA/cm^2. The inset in **Figure 3.9 (a)** shows the LSV curve before and

after subjecting to 1000 CV cycles where no significant changes in the polarization curve of α- Fe_2O_3:V-NiFe LDH was observed before and after the experiment, which further substantiates the stability of the system. Digital images of bare carbon paper, α- Fe_2O_3 and α- Fe_2O_3:V-NiFe LDH were shown in the inset of **Figure 3.9 (a)**. In-situ grown α- Fe_2O_3 shows a light-yellow color, and with NiFe LDH deposition, it shows a darker version of yellow. Faradaic yields were calculated using online gas chromatography to determine whether the gases coming from the material were purely due to water oxidation and not from the side reactions. The expected hydrogen (H_2) to oxygen (O_2) ratio of 2:1 was obtained, and the experimentally calculated Faradaic yield was about 93 % for oxygen evolution reaction (**Figure 3.9 (b)**).

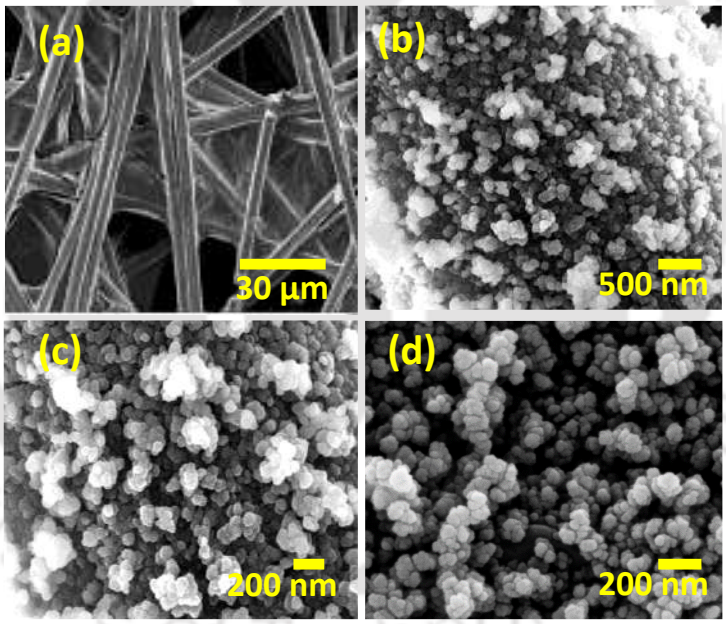

Figure 3.10 Field Emission Scanning Electron Microscopy (FESEM) image of (a) Bare Carbon cloth (b) α- Fe_2O_3:V (c) α- Fe_2O_3:V-NiFe LDH (Before stability test) (d) α- Fe_2O_3:V-NiFeLDH (After stability test).

Figure 3.10 ((a)-(c)) shows the FESEM image of bare carbon cloth, α- Fe_2O_3:V, α- Fe_2O_3:V-NiFe LDH respectively (before stability test), and **Figure 3.10 (d)** show FESEM image of α- Fe_2O_3:V-NiFeLDH after stability test. No significant morphological changes from bare α- Fe_2O_3 were observed with vanadium doping into the hematite (**Figure 3.10 (b)**) and

subsequent deposition of NiFe LDH onto the vanadium doped hematite particles (**Figure 3.10 (c)**). From **Figure 3.10 (c)-(d)**, no change in morphology before and after the electrochemical measurements were observed, which indicates the stability of the electrode.

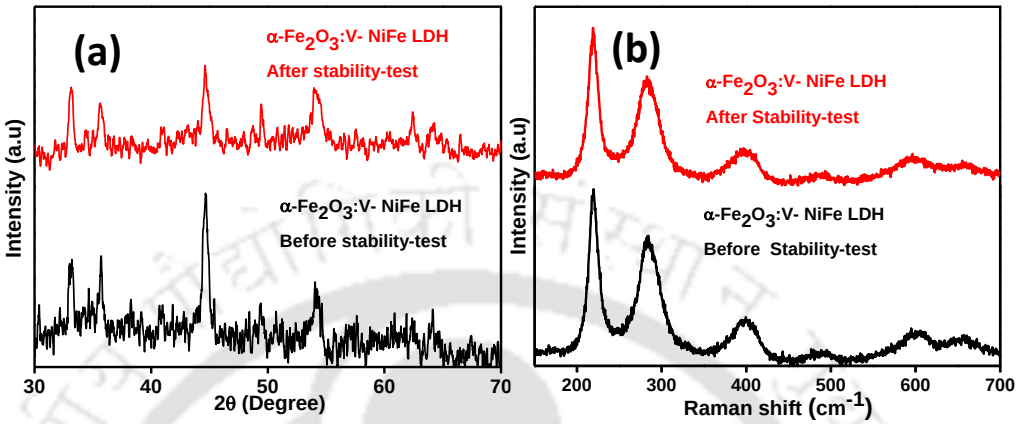

Figure 3.11 (a) XRD diffraction patterns of α- Fe_2O_3:V-NiFe LDH (Before and After stability-test) and (b) Raman spectra of α- Fe_2O_3:V-NiFe LDH (Before and After stability-test).

Figure 3.11((a)-(b)) shows the XRD and Raman spectra of the composite α- Fe_2O_3:V-NiFe LDH before and after durability test respectively. No changes in phase composition were observed in the composites before and after the durability test, which further substantiates the stability of the system.

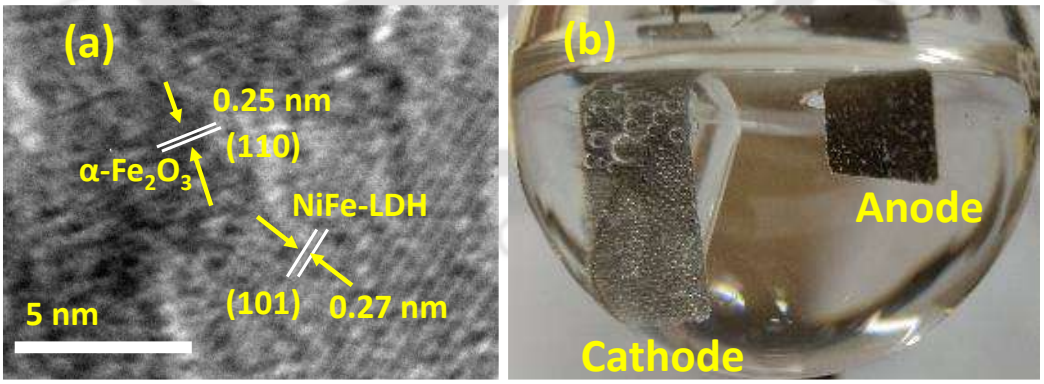

Figure 3.12 (a) High Resolution Transmission Electron Microscopy (HRTEM) images of α- Fe_2O_3:V-NiFe LDH (After stability test) and (b) Digital image of the set up for performing electrochemical measurements.

HRTEM image of α- Fe_2O_3:V-NiFe LDH **(Figure 3.12 (a))** after stability test, no change in d- spacing value of α- Fe_2O_3 (0.25 nm) and NiFe LDH (0.27 nm) were observed. The digital image of sets up for performing electrochemical measurements were shown in **(Figure 3.12 (b))** consisting of α- Fe_2O_3:V-NiFe LDH working electrode, Pt mesh counter electrode and Ag/Agcl reference electrode.

3.3.8 Inductively coupled plasma - optical emission spectrometry (ICP-OES)

ICP-OES (Inductively coupled plasma - optical emission spectrometry) measurement was performed to quantify the amount of catalyst loaded on the substrate. 1 cm^2 (1x1cm) catalyst electrode (α- Fe_2O_3:V and NiFe LDH) was dissolved in concentrated HCl and H_2SO_4 solution (1:1). Then, 1 mL of sample solution was further diluted to 20 mL with deionized water, and measured with ICP-OES.

Table 3.2. The prepared average mass loading of catalyst on carbon paper substrate.

Catalyst	**Mass Loading (mg/cm^2)**
α- Fe_2O_3	**~1.2**
α- Fe_2O_3:V	**~1.4**
NiFe LDH	**~0.4**

3.4 CONCLUSIONS

In summary, superior electrocatalytic activity of α- Fe_2O_3:V-NiFe LDH electrode could be attributed to the following factors: (1) the hydrothermally grown α- Fe_2O_3 directly onto carbon paper benefits the electrical conductivity and superior mechanical stability of the resulting electrode under gas evolution conditions, (2) vanadium doped hematite (α- Fe_2O_3:V) with deposition of NiFe LDH (α- Fe_2O_3:V-NiFe LDH), increased the number of charge carrier

density and electrocatalytically active sites and enhanced surface reaction kinetics for water oxidation, (3) superior contact between the electrocatalyst and electrolyte. The present system (α- Fe_2O_3:V-NiFe LDH) required only 190 mV overpotential to drive 10 mA/cm^2 current density, at a low Tafel slope value of 42 mV/dec with continuous stability for 12 hours.

3.5. REFERENCES

1. G. Chen, T. Wang, J. Zhang, P. Liu, H. Sun, X. Zhuang, M. Chen and X. Feng, *Adv. Mater*., 2018, **30**, 1706279.
2. H. Zhang, X. Li, A. Hähnel, V. Naumann, C. Lin, S. Azimi, S. L. Schweizer, A. W. Maijenburg and R. B. Wehrspohn, *Adv. Funct. Mater*., 2018, **28**, 1706847.
3. L. Yu, H. Zhou, J. Sun, F. Qin, F. Yu, J. Bao, Y. Yu, S. Chen and Z. Ren, *Energy Environ. Sci*., 2017, **10**, 1820.
4. Z. Qiu, C.-W. Tai, G. A. Niklasson and T. Edvinsson, *Energy Environ. Sci*., 2019, **12**, 572.
5. A. Samanta, S. Das and S. Jana, *ACS Sustainable Chem. Eng.* 2019, **7**, 12117.
6. X. Yu, J. Liu, W. Yin, T. Wang, L. Quan, Y. Ran, J. Cui, L. Wang and Y. Zhang, *Appl. Surf. Sci*., 2019, **492**, 264.
7. J. Chi, H. Yu, B. Qin, L. Fu, J. Jia, B. Yi and Z. Shao, *ACS Appl. Mater. Interfaces*, 2017, **9**, 464.
8. Y. B. Park, J. H. Kim, Y. J. Jang, J. H. Lee, M. H. Lee, B. J. Lee, D. H. Young and J. S. Lee, *ChemCatChem*, 2019, **11**, 443.
9. F. Malara, A. Minguzzi, M. Marelli, S. Morandi, R. Psaro, V. Dal Santo and A. Naldoni, *ACS Catal*., 2015, **5**, 5292.
10. Y. Yan, J. Lin, J. Cao, S. Guo, X. Zheng, J. Feng and J. Qi, *J. Mater. Chem. A*, 2019, **7**, 24486.

11. T. K. Sahu, A. K. Shah, A. Banik and M. Qureshi, *ACS Appl. Energy Mater*. 2019, **2**, 4325.
12. Y. Zhang, S. Jiang, W. Song, P. Zhou, H. Ji, W. Ma, W. Hao, C. Chen and J. Zhao, *Energy Environ. Sci*., 2015, **8**, 1231.
13. G. Liu, Y. Zhao, K. Wang, D. He, R. Yao and J. Li, *ACS Sustainable Chem. Eng*. 2018, **6**, 2353.
14. Z. Cai, X. Bu, P. Wang, J. C. Ho, J. Yang and X. Wang, *J. Mater. Chem. A*, 2019, **7**, 5069.
15. M. A. Mahadik, A. Subramanian, H.-S. Chung, M. Cho and J. S. Jang, *ChemSusChem*, 2017, **10**, 2030.
16. Z. Wu, Z. Zou, J. Huang and F. Gao, *ACS Appl. Mater. Interfaces* 2018, **10**, 26283.
17. P. F. Liu, S. Yang, B. Zhang and H. G. Yang, *ACS Appl. Mater. Interfaces*, 2016, **8**, 34474.
18. Q. Xiao, Y. Zhang, X. Guo, L. Jing, Z. Yang, Y. Xue, Y. -M. Yan and K. Sun, *Chem. Commun*., 2014, **50**, 13019.
19. F. Y. Ning, M. F. Shao, S. M. Xu, Y. Fu, R. K. Zhang, M. Wei, D. G. Evans and X. Duan, *Energy Environ. Sci*., 2016, **9**, 2633.
20. B. Z. Yu, X. L. Liu, H. G. Zhang, G. Y. Jing, P. Ma, Y. Luo, W. M. Xue, Z. Y. Ren and H. M. Fan, *J. Mater. Chem. A*, 2015, **3**, 16544.
21. R. Nikam, S. Rayaprol, S. Mukherjee, S.D. Kaushik, P.S. Goyal, P.D. Babu, S. Radha, V, Siruguri. *Phys. B (Amsterdam, Neth.)* 2019, **574**, 411663.
22. G. Goyal, A. Dogra, S. Rayaprol, S. D. Kaushik, V. Siruguri, H, Kishan. *Mater. Chem. Phys*., 2012, **134**, 133.
23. J. Jiang, F. Sun, S. Zhou, W. Hu, H. Zhang, J. Dong, Z. Jiang, J. Zhao, J. Li, W. Yan, M. Wang. *Nat. Commun*., 2018, **9**, 2885.

24. A. Annamalai, R. Sandström, E. Gracia-Espino, N. Boulanger, J-F Boily, I. Mühlbacher, A. Shchukarev, T. Wågberg, *ACS Appl. Mater. Interfaces*, 2018, **18**, 16467-164673.

25. X. Zhang, H. Li, S. Wang, F. R. F. Fan, A. J. Bard, *J. Phys. Chem. C*, 2014, **118,** 16842-16850.

26. M. Rioult, D. Stanescu, E. Fonda, A. Barbier, H. Magnan, *J. Phys. Chem. C*, 2016, **120**, 7482-7490.

27. S. Li, C. Xi, Y.-Z. Jin, D. Wu, J.-Q. Wang, T. Liu, H.-B. Wang, C.-K. Dong, H. Liu, S. A. Kulinich, X.-W. Du, *ACS Energy Lett.*, 2019, **4,** 1823-1829.

28. Q. Liu, J. Shi, J. Hu, A. M. Asiri, Y. Luo, X. Sun, *ACS Appl. Mater. Interfaces*, 2015, **7,** 3877– 3881.

29. Z. Gu, J. J. Atherton, Z. P. Xu, *Chem. Commun.*, 2015, **51,** 3024-3036.

30. S. Shen, J. Zhou, C. Dong, Y. Hu, E. N. Tseng, P. Guo, L. Guo, S. S. Mao, *Sci Rep*, 2015, **4,** 6627.

31. R. Li, Y. Wang, W. Li, S. Zhou, P. Tian, H. Gao, X. Liu and J. Zang, *Chem. Commun.*, 2019, **55**, 13370.

32. Y. Yang, L. Dang, M. J. Shearer, H. Sheng, W. Li, J. Chen, P. Xiao, Y. Zhang, R. J. Hamers and S. Jin, *Adv. Energy Mater.*, 2018, **8**, 1703189.

33. B. Chen, W. Fan, B. Mao, H. Shen and W. Shi, *Dalton Trans.*, 2017, **46**, 16050.

34. Z. Li, M. Shao, H. An, Z. Wang, S. Xu, M. Wei, D. G. Evans and X. Duan, *Chem. Sci.*, 2015, **6**, 6624.

35. M. W. Louie and A. T. Bell, *J. Am. Chem. Soc*. 2013, **135**, 12329.

36. S. Pintado, S. Goberna-Ferrón, E. C. Escudero-Adán and J. R. Galán-Mascarós, *J. Am. Chem. Soc*. 2013, **135**, 13270.

37. X. Li, X. Hao, Z. Wang, A. Abudula, G. Guan, *J. Power Sources*, 2017, **347**, 193.

CHAPTER 4

Hierarchical FeO(OH)/CoCeV (oxy)hydroxide as a water cleavage promoter

Search for a bifunctional electrocatalyst having water cleavage promoting ability along with the operational stability to efficiently generate oxygen and hydrogen for practical applications is the ongoing challenges. These fundamental ideas can be achieved by designing the morphology, tuning the electronic structure, and using dopants in their higher oxidation states. Herein, we have fabricated a binder-free FeO(OH)-CoCeV-layered triple hydroxide (LTH) bifunctional catalyst by a two-step hydrothermal method, in which the nanograin shaped FeO(OH) coupled with CoCeV-LTH nanoflakes provide more electro catalytically active sites and enhanced the charge transfer kinetics for hydrogen evolution reaction (HER) and oxygen evolution reaction (OER).

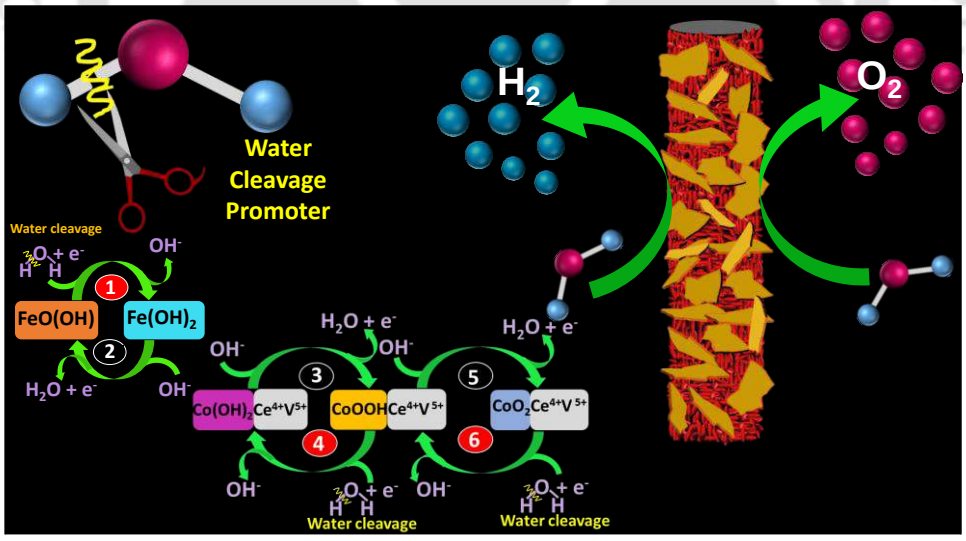

C. T. Moi et al., *ACS Appl. Mater. Interfaces,* 2021, **13**, 51151–51160

4.1 INTRODUCTION

With the projected depletion of fossil fuels and global warming, the consumption of energy generated from clean and renewable energy sources is expected to surge in the near future.[1, 2] Electrocatalytic splitting of water into molecular hydrogen and oxygen is considered to be a promising approach for generation, storage and usage of sustainable hydrogen production, rechargeable batteries and fuel cells, without giving harmful by-products.[3] At present, the state-of-the-art catalysts to split water at practical current densities are noble metals like Pt and RuO_2 for hydrogen evolution reaction (HER) and oxygen evolution reaction (OER), respectively. Their high cost and scarcity act as the major hurdles for their scale-up for practical applications.[4] For practical overall water splitting, coupling of electrodes in a common electrolyte is challenging, due to the mismatch of pH ranges in which both the catalysts are most stable and active. The drawbacks for efficient HER in the alkaline condition are its high water dissociation energy, while the multi-step proton-electron transfer involved in OER hinders its surface kinetics.[5] Therefore, to develop a bifunctional electrocatalyst with high activity towards both OER and HER in the same electrolyte is significant.[6]

Numerous efforts have been made on earth-abundant elements, such as transition-metal nitrides,[7] phosphides,[8] sulfides,[9] oxides[11] and oxy(hydroxides)[11]. Among them, earth-abundant iron-based catalysts such as iron oxide hydroxide (FeOOH) have been studied as a promising OER active material, due to its adsorption tendency to hydroxyl species and H_2O molecules.[12] FeOOH due to its low cost, natural abundance, open structure, environmentally benign and high activity in alkaline media favors its wide application.[12] However, the poor intrinsic conductivity ($\approx 10^{-5}$ S/cm) of FeOOH hinders its practical application for water splitting.[3, 13] Efforts have been made to improve the poor activity, including tuning of electronic structure, morphological control, composition, and interface engineering, which have been reported to increase the specific surface area and active sites.[14] To increase the water dissociation activity,

water cleavage "promoters" have been introduced to the electrocatalysis field. Among various contenders, hydroxides and oxides own good water affinity. Thus, the modification of the electrocatalysts with hydroxides and oxides is regarded as a promising way to promote the water dissociation ability of the electrocatalysts.[6,15]

The layered double hydroxides (LDHs) with positively charged metal hydroxide layers and intercalated anions have been widely studied for water splitting.[16-20] Based on the reported work, layered triple hydroxides (LTHs), like NiCoV LDH,[16] CoMoV LDH,[17] NiFeCr LDH,[18] NiFeV LDH,[19] and CoFeV LDH[20] have exhibited better catalytic activity than their counter LDHs, owing to enhanced synergistic activities between metal ions and their electronic structure.[16, 17] To improve the catalytic activity, the incorporation of heterogeneous metal atoms is an effective approach to obtain optimal adsorption energy of reaction intermediates.[18] According to reports, the optimal bond strength between the cations and water molecules can be obtained with metals having higher oxidation states, such as Cr^{4+}, Fe^{3+}, W^{6+}, and V^{5+}.[18, 20]

Herein, we have reported a multi-metallic heterostructure strategy for FeO(OH) nanograin coupled with CoCeV-LTH nanoflake arrays with multiple components for improved overall water splitting. The FeO(OH) provides better catalytic active sites and the CoCeV-LTH enhances the surface reaction kinetics. The FeO(OH) is hydrothermally grown directly onto the carbon paper substrate, with subsequent anchoring of CoCeV-LTH by two-step hydrothermal synthesis. The multi-metallic heterostructure FeO(OH)-CoCeV-LTH requires 53 mV for HER and 227 mV for OER to drive 10 mA/cm^2 current density in 1M KOH, with a corresponding Tafel slope of 70 mV/dec and 52 mV/dec, for HER and OER respectively. Benefiting from the binder-free and strong synergistic interaction, the FeO(OH)-CoCeV-LTH/CP shows superior HER and OER, with a continuous long-term stability test for 24 h. A detailed mechanistic study based on various characterization studies such as cyclic voltammetry, X-ray photoelectron spectroscopy and electrochemical impedance has been presented in the chapter.

4.2 EXPERIMENTAL SECTION

4.2.1 Carbon paper (CP) treatment

The commercial carbon paper (CP) is treated in a concentrated H_2SO_4–HNO_3 (2:1) mixture, and hydrothermally treated at 100 °C for 2 h. The treated CP is cleaned with deionized water and absolute ethyl alcohol for several times, then dried at 80 °C in a vacuum oven.

4.2.2 Synthesis of FeO(OH)/CP

$FeCl_3$ (0.4 mM) and NH_4F (2.4 mM) are dissolved in 25 ml of H_2O and hydrothermally treated at 160 °C in 50 ml Teflon autoclave with activated carbon paper as the substrate, with varying hydrothermal reaction time.[21] The synthesized product grown on the CP is cleaned with deionized water and absolute ethyl alcohol and dried overnight at an 80 °C vacuum oven. The carbon paper is sealed with polyamide tape during the hydrothermal synthesis except for 1x1 cm^2 area.

4.2.3 Synthesis of FeO(OH)-CoCeV-LTH-CP

The composite FeO(OH)-CoCeV-LTH-CP is prepared by taking different molar concentrations of $CoCl_2.6H_2O$ (0.5 mM), $Ce(NO_3).6H_2O$ (0.05 mM), NH_4VO_3 (0.15 mM)and Urea (CH_4N_2O) (2 mM), which are dissolved in 25 mL of H_2O and stirred for 30 minutes to give a homogenous solution. The hydrothermally grown FeO(OH)-CP film is used as the substrate and hydrothermally treated at 120 °C for 12 h. For bare CoCeV-LTH, the same procedure is followed except for the use of bare CP as the substrate.[20]

4.2.4 Preparation of benchmark 10 % Pt/C and RuO_2

The commercial RuO_2 and 10 % Pt/C powders are used as a benchmark for OER and HER respectively. For the electrode fabrication, 4 mg of RuO_2 or 10 % Pt/C is dispersed in the mixture of water (50 µL), ethanol (120 µL) and Nafion solution (20 µL), and the mixture is

ultrasonically treated for 30 min to obtain a homogeneous ink. Then, 60 µL of the ink is dropped cast on 1 × 1 cm^2 carbon paper and dried at 80 °C vacuum oven for 24 h. The loading amount of RuO_2 or 10% Pt/C on the CP is about ~1.2 mg/cm^2.

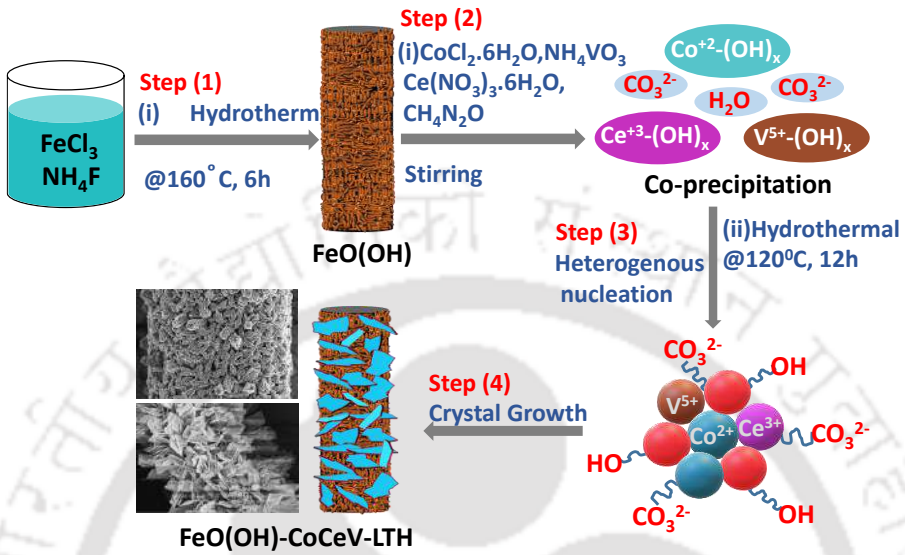

Scheme 4.1 Schematic Illustration of synthesis routes of FeO(OH)-CoCeV-LTH.

The heterostructure FeO(OH)-CoCeV-LTH is synthesized by a two-step hydrothermal method, the schematic illustration process is shown in **Scheme 4.1**. In step (1), the nanograin FeO(OH) is hydrothermally synthesized at 160 °C by using $FeCl_3$ and NH_4F as the starting materials. In step (2) growth of CoCeV species by precipitation of a mixture of metal precursors induced by slow hydrolysis of urea (urea releases carbonate ions, which helps in accelerating the kinetics of formation of nuclei) to form corresponding metal hydroxides $M(OH)_x$, in step (3) corresponding metal hydroxides, i.e. $Co(OH)_x$, $Ce(OH)_x$, and $V(OH)_x$, will aggregate to form LTH nuclei onto the FeO(OH)/CP substrate, i.e., through heterogeneous nucleation under hydrothermal condition at 120° C and in step (4) nuclei will transform into the crystalline LTH. Since the hydrothermal synthesis is driven under mild reaction conditions, the system remains close to its thermodynamic equilibrium. Therefore, LTH crystals tend to develop in their natural

habitat, getting a sheet-like morphology.[22,23] The left corner of **Scheme 4.1** shows the FESEM image of FeO(OH) (top left corner) and CoCeV-LTH (bottom left corner).

4.3 RESULTS AND DISCUSSIONS

4.3.1 Powder X-Ray Diffraction (PXRD) and Raman Analysis

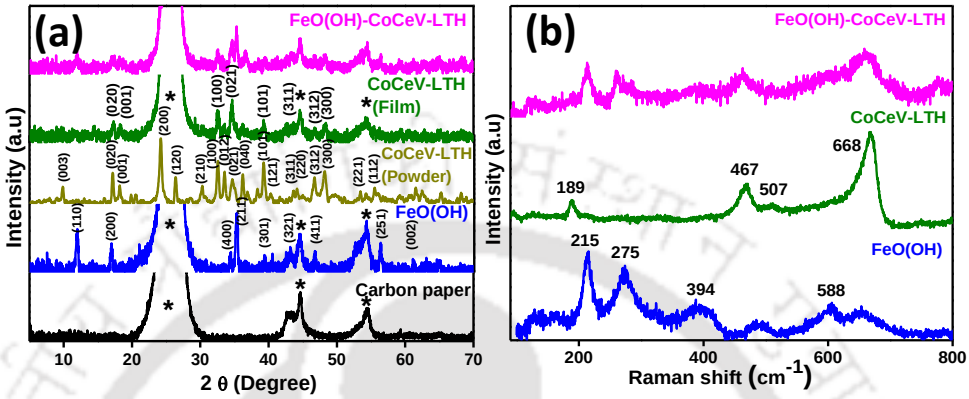

Figure 4.1 (a) XRD of substrate carbon paper, FeO(OH), CoCeV-LTH and FeO(OH)-CoCeV-LTH, ***** indicates the substrate carbon paper peaks, (b) Raman spectra of FeO(OH), CoCeV-LTH and FeO(OH)-CoCeV-LTH.

Figure 4.1 (a) shows X-ray diffraction (XRD) patterns of the as-prepared catalysts, FeO(OH), CoCeV-LTH and FeO(OH)-CoCeV-LTH, where peaks at 12.0°, 16.9°, 34.4°, 35.4°, 39.3°, 43.2°, 46.8° and 56.4° correspond to (110), (200), (400), (211), (301), (321), (411) and (521) planes of FeO(OH) (JCPDS No. 01-075-1594), respectively.[8] The XRD patterns of CoCeV-LTH, where peaks at 18.2°, 32.5° and 39.1° are indexable to $Co(OH)_2$ (JCPDS No. 00-002-0925), and $Ce(OH)_3$ peaks are observed at 42.7°, 46.7° and 48.3° (JCPDS No. 01-074-0665), and VOOH peaks are obtained at 17.2° and 34.5°(JCPDS No. 00-027-0946). The PXRD of CoCeV-LTH is given in **Figure 4.1 (a)**, where peaks of Co, Ce and V hydroxide are indexable, which confirms their presence. The diffraction peaks at 10.1° and 34.5° corresponds to (003) and (012) respectively showing typical diffraction peaks of the layered hydroxide structure. In **Figure 4.1 (b)**, the Raman spectrum exhibits four main peaks at 215, 275, 394 and 588 cm^{-1}, which can be assigned to the vibrational modes of FeO(OH).[12] The peak at 275 cm^{-1} is assigned to the vibrational E_g mode of the symmetric Fe-O bending. The Raman

peaks located at 189, 467, 507 and 668 cm^{-1} can be indexed to the characteristic bending and stretching vibrations of $Co(OH)_2$, the band at 467 cm^{-1} is assigned to O-Co-O bending mode, the bands at 507 and 668 cm^{-1} can be assigned to E_g and A_{1g} mode respectively.[24]

4.3.2 X-Ray Photoelectron Spectroscopy (XPS) Analysis

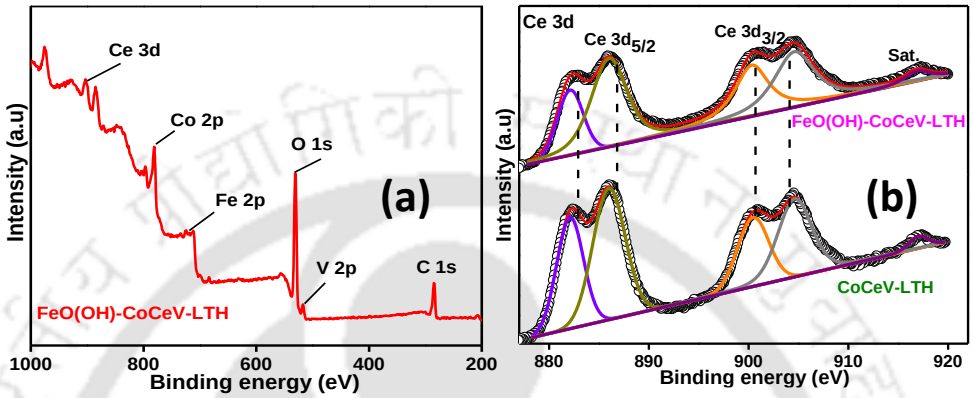

Figure 4.2 (a) XPS survey spectra of FeO(OH)-CoCeV-LTH and XPS spectra of (b) Ce 3d of CoCeV-LTH and FeO(OH)-CoCeV-LTH.

The chemical state and electronic interaction of prepared electrocatalysts are analyzed by performing XPS, in which peaks are calibrated with C1s spectra at 284.7 eV. **Figure 4.2 (a)** shows the XPS survey spectrum of FeO(OH)-CoCeV-LTH, which confirms the presence of Fe, O, Co, Ce and V elements in the composite. The Ce 3d XPS spectra are shown in **Figure 4.2 (b)**, the Ce $3d_{5/2}$ is deconvoluted into peaks at 882.1 eV and 886 eV which corresponds to Ce^{3+} and Ce^{4+} respectively and Ce $3d_{3/2}$ shows two main peaks at 900.45 eV and 904.61 eV, assignable to Ce^{3+} and Ce^{4+} respectively with a satellite peak at 917 eV for CoCeV-LTH. The high-resolution XPS spectra of Ce 3d of FeO(OH)-CoCeV-LTH exhibited two peaks at 900.3 eV and 904.6 eV, which could be assigned to Ce $3d_{3/2}$, and the peaks at 882.1 eV and 886 eV are attributable to Ce $3d_{5/2}$. These results indicated the coexistence of Ce^{3+} and Ce^{4+} in the FeO(OH)-CoCeV-LTH structure, however significant contribution could be coming in having higher valence state aiding the water cleavage process.[25]

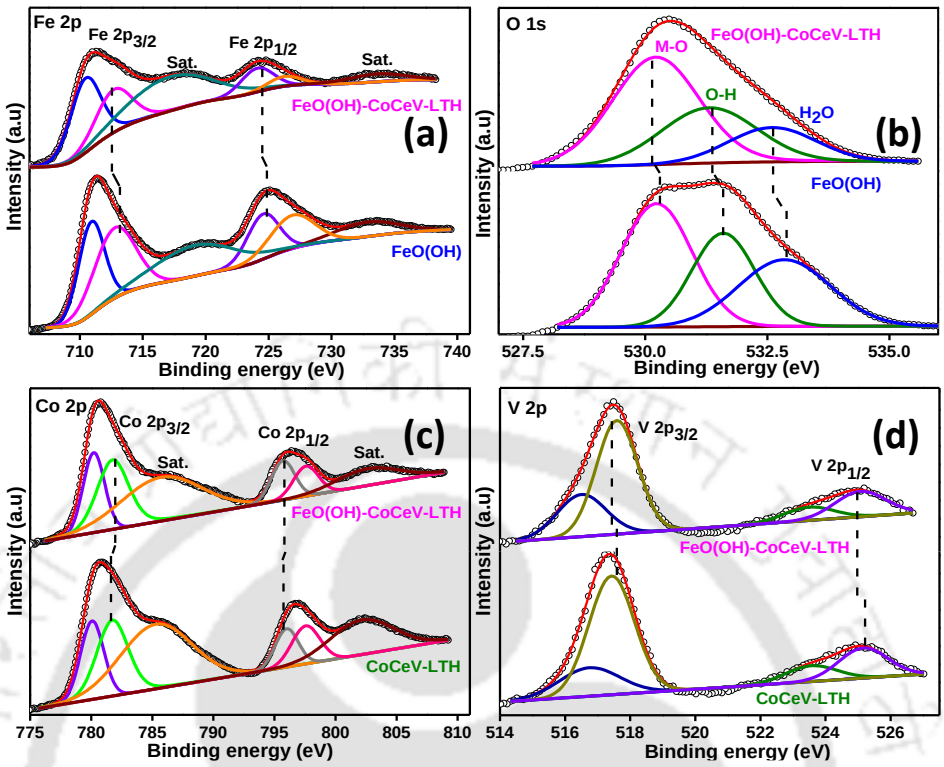

Figure 4.3 High resolution XPS spectra of (a) Fe 2p and (b) O 1s of FeO(OH) and FeO(OH)-CoCeV-LTH, (c) Co 2p and (d) V 2p of CoCeV-LTH and FeO(OH)-CoCeV-LTH.

In the Fe 2p spectra of FeO(OH)-CoCeV-LTH **(Figure 4.3 (a))**, peaks at 710.4 eV and 724.1 eV can be assigned to Fe $2p_{3/2}$ and Fe $2p_{1/2}$ respectively, which are associated with Fe^{3+}, with a shakeup satellite peak at 717.2 eV, confirming the presence of FeO(OH). Another two main peaks at 712.6 eV of Fe $2p_{3/2}$ and 726.2 eV of Fe $2p_{1/2}$ corresponds to Fe in +2 oxidation state, with satellite peak at 733.5 eV. The Fe 2p in FeO(OH)-CoCeV-LTH shows a redshift in binding energy (BE) by ~0.4 eV as compared to bare FeO(OH), suggesting a strong electronic interaction among Fe and Co at the interface which helps in the charge transfer process and improved HER and OER activity.[12, 26] The O 1s core-level spectra as shown in **Figure 4.3 (b)** of FeO(OH) can be deconvoluted into three main peaks, where peak at 530.2 eV corresponds to lattice oxygen (M−O), the peak at 531.6 eV is assignable to lattice OH group (M−OH) of the hydroxide or (oxy)hydroxide, and the peak at 532.9 eV is attributed to the surface-adsorbed

H_2O molecules. The O 1s core-level spectra of FeO(OH)- CoCeV-LTH shift to lower binding energy by ~0.3 eV as compared to pure FeO(OH), which indicates a strong electronic interaction between oxide hydroxide, FeO(OH) and CoCeV-LTH.[25-27] The XPS spectra of CoCeV-LTH **(Figure 4.3 (c))** exhibits two main peaks of Co $2p_{3/2}$ at 780.1 eV and 781.7 eV which corresponds to Co^{3+} and Co^{2+} respectively, with a satellite peak at 785.3 eV, and Co $2p_{1/2}$ peaks at 796.0 eV for Co^{3+} and 797.6 eV for Co^{2+} with a satellite peak of 802.2 eV. The Co $2p_{3/2}$ and Co $2p_{1/2}$ are energetically separated by about 15.9 eV.[16, 28] In the composite, the valence state of Co is shifted from Co^{2+} to Co^{3+}, a shift to higher binding energy by ~0.14 eV in Co 2p spectra are observed in the composite. The Fe 2p show a red shift in BE in the composite, resulting in changes in the electronic state of Co 2p after the electronic interaction with Fe 2p.[28] In the composite, electron transfer takes place from Co to Fe, indicating a partial change in oxidation states of Co and Fe to higher and lower oxidation states, respectively. The lower valence state of Fe^{2+} is favorable for H_2O molecule adsorption, while the higher valences states of Co^{3+}/Co^{4+} are more active for OER.[23, 28] The V 2p spectrum of CoCeV-LTH **(Figure 4.3 (d))** are deconvoluted into four peaks at 516.7 eV and 523.5 eV, assignable to V $2p_{3/2}$ and V $2p_{½}$, respectively of V^{4+}, and the V $2p_{3/2}$ peak at 517.4 eV and V $2p_{½}$ at 525.1 eV for V^{5+}. In FeO(OH)-CoCeV-LTH, two main peaks at 516.5 eV and 517.6 eV corresponds to V $2p_{3/2}$ assignable to V^{4+} and V^{5+} and peaks at 523.5 eV and 525.1 eV corresponds to V $2p_{½}$ of V^{4+} and V^{5+} respectively. The V 2p spectra of FeO(OH)-CoCeV-LTH shows a redshift in BE by ~0.2 eV, which indicates the presence of cations with higher oxidation states, and enhance the redox reactions during the OER.[17, 20, 23]

4.3.3 Morphological Analysis

Figure 4.4 (a) exhibits the FESEM image of FeO(OH) sample with a reaction time of 6 h, which shows the formation of uniformly distributed nanograin structures on the carbon paper (CP) substrate. Further, increase in the reaction time to 8 h and 10 h, there are no

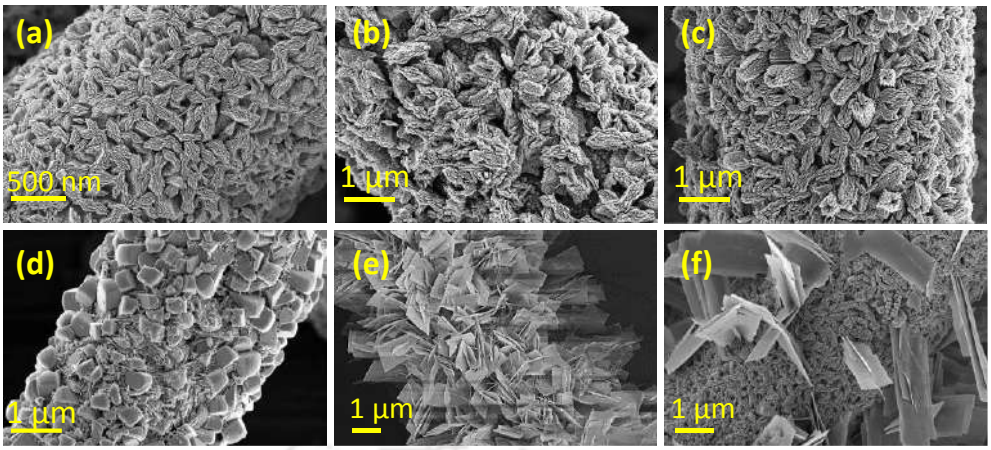

Figure 4.4 Field Emission Scanning Electron Microscopy (FESEM) images of (a-d) FeO(OH) for 6 h, 8 h, 10 h, and 12 h respectively, (e) CoCeV-LTH and (f) FeO(OH)-CoCeV-LTH.

significant morphological changes are observed **(Figure 4.4 (a-c))**. Upon increasing the reaction time to 12 h, the nanograin morphology transforms to a cube-kind of morphological structure **(Figure 4.4 (d))**. The morphology of CoCeV-LTH **(Figure 4.4 (e))** shows nanoflakes structure uniformly grown over the CP substrate, and in the composite **(Figure 4.4 (f))**, CoCeV-LTH nanoflakes are decorated on the surface of FeO(OH) nanograins.

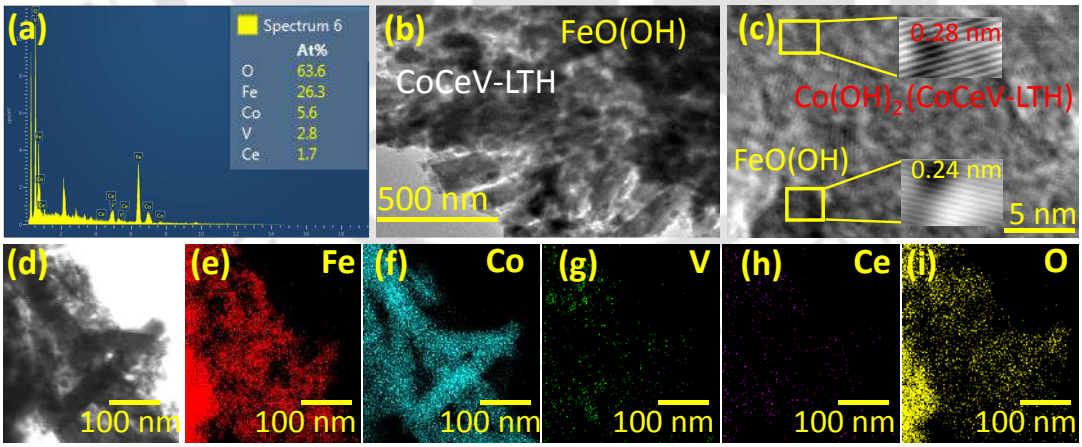

Figure 4.5 (a) EDX spectrum of FeO(OH)-CoCeV-LTH. Transmission Electron Microscopy (TEM) image of (b) FeO(OH)-CoCeV-LTH, and High Resolution Transmission Electron Microscopy (HRTEM) image of (c) FeO(OH)-CoCeV-LTH, Transmission Electron Microscopy (TEM) image of (d) FeO(OH)-CoCeV-LTH and (e)-(i) corresponding EDX elemental mapping analysis of the composite.

The EDX spectrum is recorded for the composites (FeO(OH)-CoCeV-LTH), which briefs the composition of the composite as shown in **Figure 4.5 (a)**. The composition studies confirm the presence of all elemental atoms (atomic percentage) in the composite: Fe (26.3), Co (5.6), Ce (1.7), V (2.8) and O (63.6). TEM measurements are performed (**Figure 4.5 (b))** to confirm the crystal structure of FeO(OH)-CoCeV-LTH, and the HRTEM in **Figure 4.5 (c)** (FeO(OH)-CoCeV-LTH) reveals the lattice fringes with an interplanar spacing of 0.24 nm and 0.28 nm, which corresponds to (211) crystal plane of FeO(OH) and (100) crystal plane of CoCeV-LTH, respectively. **Figure 4.5 (d)-(i)** shows the elemental mapping analysis of FeO(OH)-CoCeV-LTH, which confirms the presence of all elements Fe, Co, V, Ce, and O in the composite.

4.3.4 *J-V* Optimization Curve

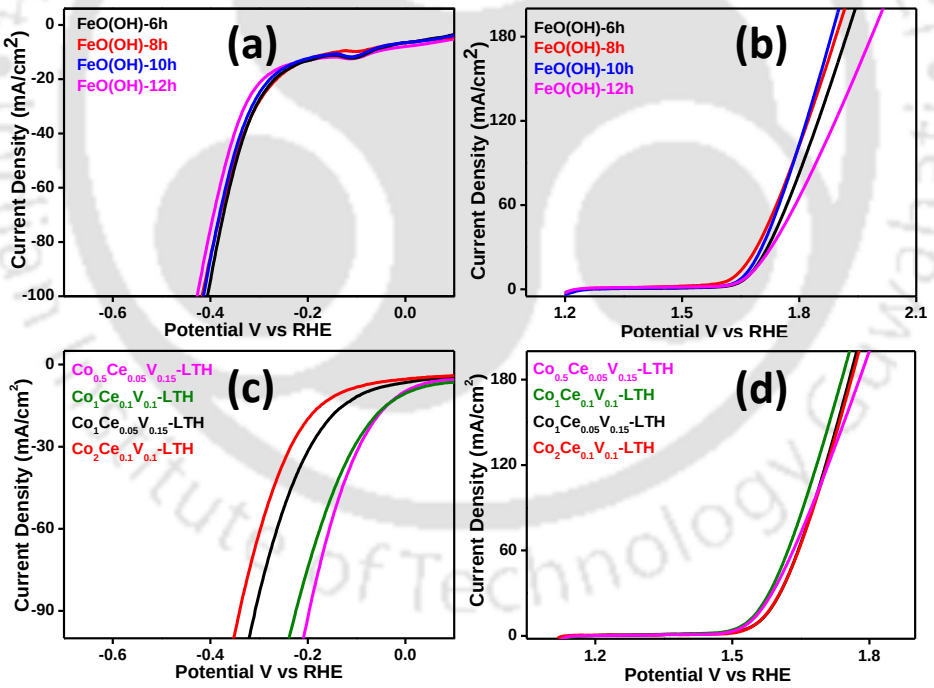

Figure 4.6 LSV Optimizations curve of (a)-(b) FeO(OH) and (c)-(d) CoCeV-LTH for HER and OER respectively at 5mV/sec in 1M KOH.

The electrocatalytic measurements of the prepared catalysts are performed in a standard three-electrode system at the scan rate of 5mV/sec in 1 M KOH. **Figure 4.6** shows the

optimization curve of an *in-situ* grown FeO(OH) and CoCeV-LTH onto carbon paper substrate in terms of reaction time and molar concentrations of CoCeV-LTH. **Figure 4.6 ((a)-(b))** shows the optimization curve of FeO(OH) substrate for 6 h, 8 h, 10 h, and 12 h for HER and OER, and 6 h reaction time is taken as the optimized reaction time for both HER and OER. Meanwhile, different molar concentrations of Co, Ce, and V have been taken to study the optimum concentration for the layered hydroxide. As shown in **Figure 4.6 ((c)-(d))**, the molar concentration of $Co_{0.5}Ce_{0.05}V_{0.15}$ is the optimized concentration for both HER and OER.

4.3.5 Cyclic Voltammogram (CV) Measurements

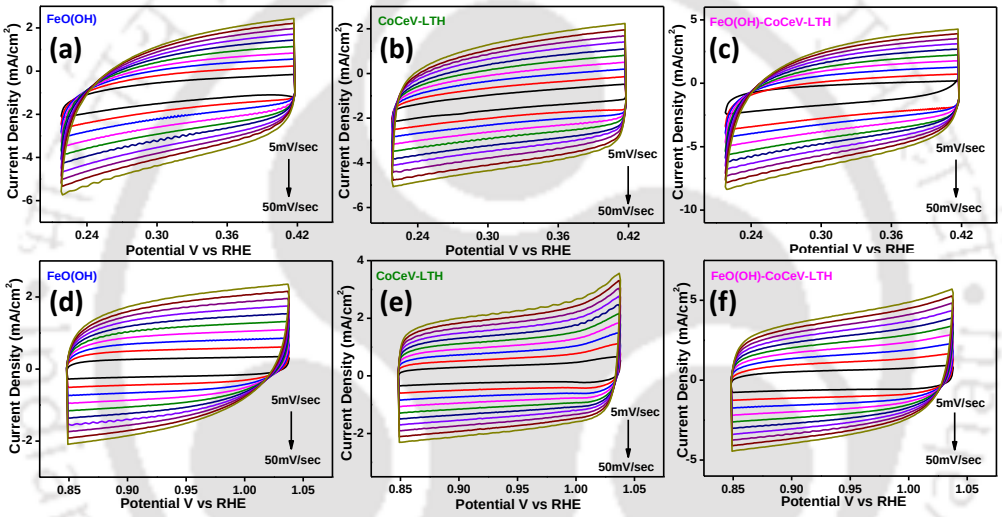

Figure 4.7 Cyclic voltammograms (CVs) curves of (a) FeO(OH), (b) CoCeV-LTH and (c) FeO(OH)-CoCeV-LTH measured at different scan rate from 5 mV to 50 mV/s within a potential windows of 0.23 V to 0.43 V in 1M KOH and (d) FeO(OH), (e) CoCeV-LTH and (f) FeO(OH)-CoCeV-LTH are CV curves measured between the potential range of 0.84 V to 1.06 V in 1M KOH.

The cyclic voltammogram (CV) of the as-prepared catalysts are shown in **Figure 4.7 ((a)-(f))**, which are scan in the non- faradaic region between the potential ranges of 0.23 V to 0.43 V for HER and 0.84 V to 1.06 V vs RHE for OER in 1M KOH electrolyte solution. The CV is scan starting from 5 mV/sec to 50 mV/sec, from which the C_{dl} values are obtained to determine the ECSA and TOF values of the electrocatalyst are also calculated from the CV.

4.3.6 Oxygen Evolution Reactions (OER)

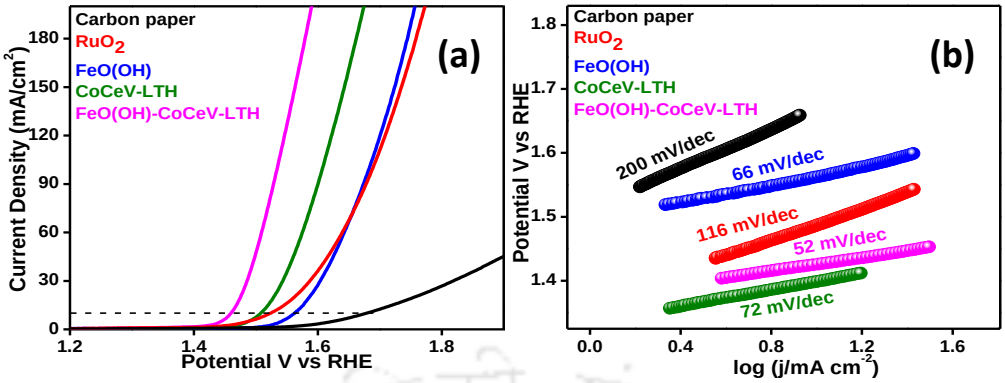

Figure 4.8 (a) LSV polarization curves and (b) Corresponding Tafel slope of carbon paper, RuO_2, FeO(OH), CoCeV-LTH and FeO(OH)-CoCeV-LTH at a sweep rate of 5 mV/s in 1M KOH.

The overpotential of the best-optimized composition along with the individual components are shown in the polarization curve **(Figure 4.8 (a))**. Overpotential of OER of FeO(OH)-CoCeV-LTH is found to be superior to that of the benchmark RuO_2 as shown in **Figure 4.8 (a)**. FeO(OH)-CoCeV-LTH requires only 227 mV to drive 10 mA/cm^2 current density, which is superior to individual catalysts, FeO(OH) (330 mV), CoCeV-LTH (278 mV), and the benchmark RuO_2 (294 mV). The Tafel slope is a significant parameter to understand the kinetics and intrinsic reaction path of the prepared catalyst, in which lower the Tafel slope indicate, faster is the reaction kinetics for water oxidation. As shown in **Figure 4.8 (b)**, a Tafel slope of 52 mV/dec is observed for FeO(OH)-CoCeV-LTH, which is lower than pristine FeO(OH) (66 mV/dec), CoCeV- LTH (72 mV/dec), and RuO_2 (116 mV/dec), which suggest a superior intrinsic catalytic oxidation kinetics for the as synthesize composite.

4.3.7 Hydrogen Evolution Reactions (HER)

Furthermore, the HER property of the prepared electrocatalyst is tested in 1M KOH, under the same experimental condition. In **Figure 4.9 (a)**, FeO(OH)-CoCeV-LTH requires an overpotential of 53 mV to drive 10 mA/cm^2 current density which is a much lower overpotential

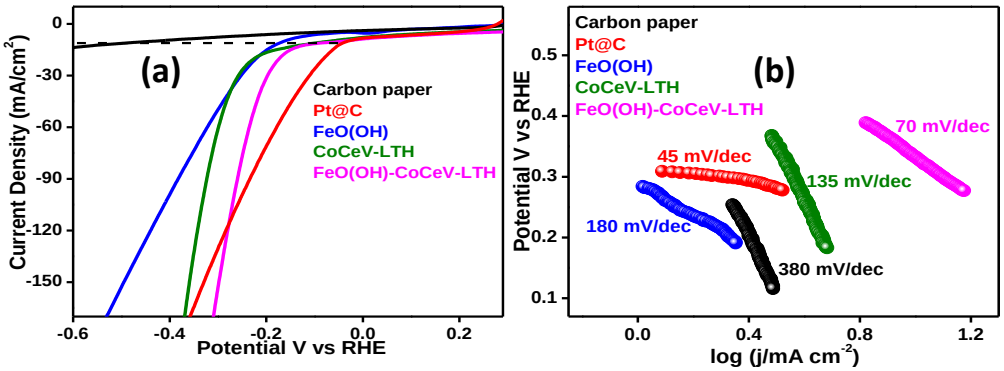

Figure 4.9 (a) LSV polarization curves and (b) Corresponding Tafel slope of carbon paper, Pt/C, FeO(OH), CoCeV-LTH and FeO(OH)-CoCeV-LTH at a sweep rate of 5 mV/s in 1M KOH,

value as compared to FeO(OH) (164 mV) and CoCeV-LTH (85mV). As expected, 10% Pt/C (36 mV) gives the best HER with a small Tafel slope value of 45 mV/dec. The corresponding Tafel slope in **Figure 4.9 (b)** shows FeO(OH)-CoCeV-LTH has a small Tafel slope of 70 mV/dec as compared to bare FeO(OH) (180 mV/dec) and CoCeV-LTH (135 mV/dec) and slightly higher to benchmark Pt/C (45 mV/dec). An increment in HER comes from enhanced surface reaction kinetics and an increase in surface active sites of the catalyst, which is proved by EIS and ECSA measurements.

4.3.8 Bar Diagrams of Oxygen Evolution Reactions (OER) and Hydrogen Evolution Reactions (HER)

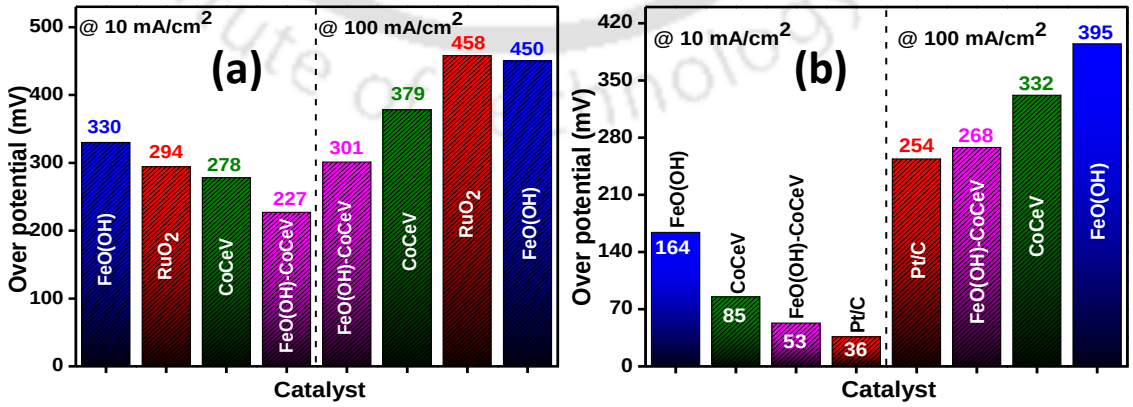

Figure 4.10 Bar diagrams showing catalytic activities at 10 mA/cm^2 and 100 mA/cm^2 for (a) OER and (b) HER.

The prepared catalysts are probed at high current density of 100 mA/cm^2 to assess the strength of their synergistic interactions and stabilities at higher current density.[29] In **Figure 4.10 (a)**, for OER, FeO(OH)-CoCeV-LTH required a low overpotential of 301 mV to drive 100 mA/cm^2 current density which is lower as compared to benchmark RuO_2 (458 mV). In **Figure 4.10 (b)**, the catalyst is probed at 100 mA/cm^2 for HER, in which the composite FeO(OH)-CoCeV-LTH required 268 mV which is close to benchmark 10% Pt/C (254 mV).

4.3.9 Electrochemically Active Surface Area (ECSA) and Turnover frequency (TOF)

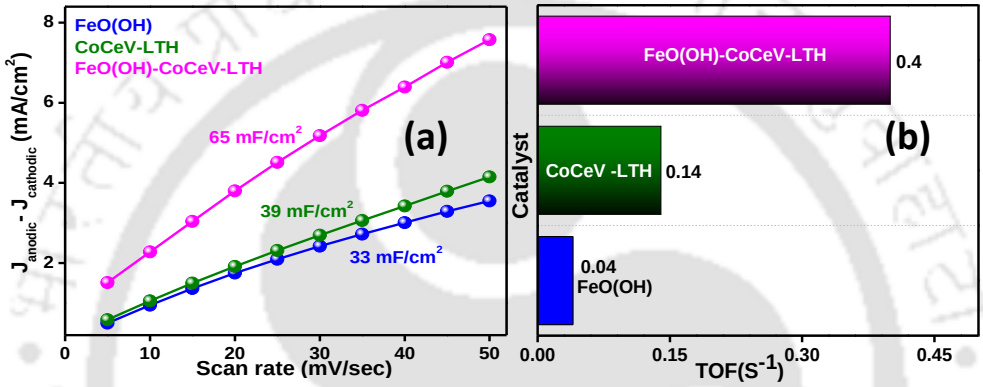

Figure 4.11 (a) $\Delta J(J_a - J_c)$ values plotted against the scanning rates and (d) Turnover frequency of FeO(OH), CoCeV-LTH and FeO(OH)-CoCeV-LTH in 1M KOH.

To better understand the source of superior activity of FeO(OH)-CoCeV-LTH, double-layer capacitance (C_{dl}) is measured in the non-faradaic potential region in 1M KOH to determine the electrochemically active surface area (ECSA) of the electrocatalyst. The C_{dl} value of the electrocatalysts are obtained from cyclic voltammograms (CV) at different scan rates (5 mV/sec to 50 mV/sec) as shown in **Figure 4.11 (a)**. The C_{dl} value of FeO(OH)-CoCeV-LTH calculated is 65 mF/cm^2, which is approximately 2 and 1.6 times higher than FeO(OH) (33 mF/cm^2) and CoCeV-LTH (39 mF/cm^2), respectively as shown in **Figure 4.11 (a)**. The higher ECSA value for the composites indicates better exposure of surface-active sites during the electrocatalytic process. The enhancement in the C_{dl} value indicates an improved synergistic interaction between the components, and better ions exchangeability between active

sites on the surface and electrolytes, leading to improved catalytic performance.[30] Turnover frequency (TOF) is calculated at 0.35 V vs RHE **(Figure 4.11 (b))**, in which FeO(OH)-CoCeV-LTH has the highest TOF value of 0.4 mF/cm^2, which is 10 and 2.8 times higher than FeO(OH) and CoCeV-LTH.

4.3.10 Electrochemical Impedance Spectroscopy (EIS) Measurements

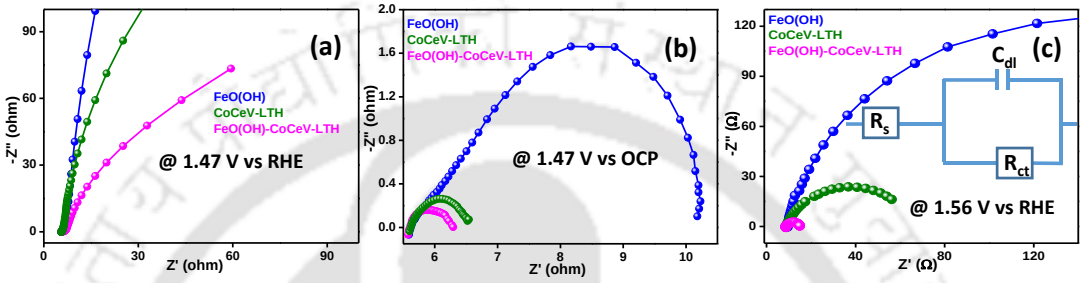

Figure 4.12 Nyquist plots of FeO(OH), CoCeV-LTH and FeO(OH)-CoCeV-LTH measured at (a) 1.47 V vs RHE, (b) 1.47 V vs OCP, (c) 1.56 V vs RHE (inset showing an equivalent circuit model).

The EIS measurements are performed to evaluate the charge transfer resistance (R_{ct}) of the electrocatalyst. In **Figure 4.12 (a)**, the smallest semicircle is obtained for FeO(OH)-CoCeV-LTH, showing the smallest R_{ct} values of 182 Ω in comparison to bare FeO(OH) (395 Ω) and CoCeV-LTH (227 Ω). The Nyquist plots are also measure at open circuit potential (OCP) in **Figure 4.12 (b)** to better understand the charge transfer kinetics. The composite (FeO(OH)/CoCeV-LTH) exhibits the lowest charge-transfer resistance (R_{ct} = 0.7 Ω), signifying the faster charge transport kinetics during the electrochemical processes. In **Figure 4.12 (c)**, EIS measurements are performed on applying higher overpotential at 1.56 V vs RHE (@100 mA/cm^2), FeO(OH)-CoCeV-LTH, shows the smallest R_{ct} values of 35 Ω in comparison to bare FeO(OH) (285 Ω) and CoCeV-LTH (227 Ω), indicating an enhancement in charge transfer kinetics of the electrocatalyst. Tabulation of the fitted parameters obtained from the Nyquist plots are shown in **Table 4.1**.

Table 4.1 Tabulation of parameters obtained from the Nyquist plots fitted to an equivalent circuit model of FeO(OH), CoCeV-LTH and FeO(OH)-CoCeV-LTH.

Catalyst	R_s (Ω)	R_{ct} (Ω)	Potential (E)
FeO(OH)	6.2	3.67	1.47 V vs OCP
	13.6	395	1.47 V vs RHE, @ 10 mA/cm^2
	12	285	1.55 V vs RHE, @ 100 mA/cm^2
CoCeV-LTH	5.7	1	1.47 V vs OCP
	11.3	260	1.47@ 10 mA/cm^2 , @ 10 mA/cm^2
	11.2	227	1.55@ 100 mA/cm^2 , @ 100 mA/cm^2
FeO(OH)-CoCeV-LTH	5.9	0.7	1.47 V vs OCP
	9.57	182	1.47@ 10 mA/cm^2 , @ 10 mA/cm^2
	9	35	1.55@ 100 mA/cm^2 , @ 100 mA/cm^2

4.3.11 Overall Water Splitting and Faradaic Yield Measurements

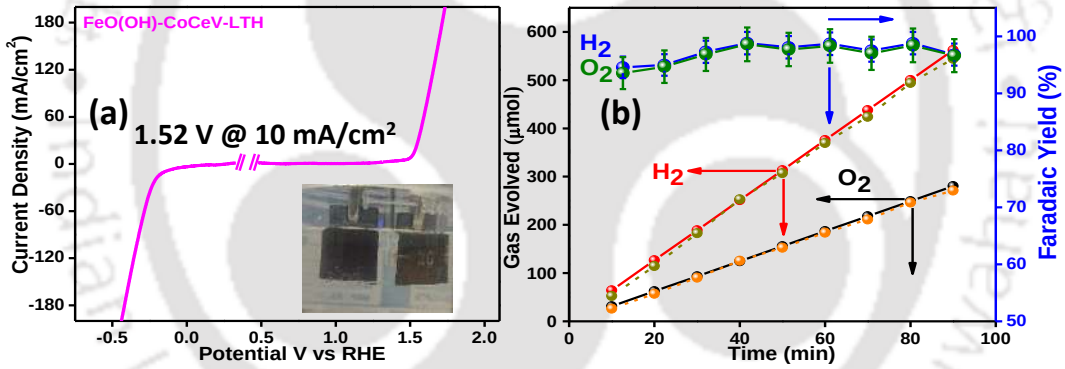

Figure 4.13 (a) LSV polarisation curve of FeO(OH)-CoCeV-LTH for overall water splitting at 5mV/sec and (b) Faradaic yield curve of FeO(OH)-CoCeV-LTH for O_2 and H_2 in 1M KOH. In the graph (red line and symbol) denotes the theoretical yield of H_2 gas, (dark yellow dotted line and symbol) denotes the experimental yield of H_2, (black line and symbol) denotes the theoretical O_2 yield and (orange dotted line and symbol) denotes the experimental yield of O_2 gas.

The prepared electrocatalyst is employed as both anode and cathode to check for overall water splitting. Notably, FeO(OH)-CoCeV-LTH exhibits a cell voltage of 1.52 V vs RHE to drive 10 mA/cm^2 in 1M KOH **(Figure 4.13 (a))**, with an inset showing the image of set up for performing the electrochemical experiment. Online gas chromatography (GC) measurements

are performed as shown in **Figure 4.13 (b)**, to calculate the Faradaic yields. The expected 2:1 ratio for H_2 to O_2 is obtained with a Faradaic yield of 98% (H_2) and 96% (O_2).

4.3.12 Role of Cerium and Vanadium in $Co(OH)_2$

To understand the role of Ce and V in the as-designed FeOOH/CoCeV LTH structure, we have synthesized FeO(OH)-$Co(OH)_2$ following the same experimental condition but without the addition of NH_4VO_3 and $Ce(NO_3)_3.6H_2O$. The as-synthesized FeO(OH)-$Co(OH)_2$ requires 249 mV to drive 10 mA current density with a corresponding Tafel slope value of 86 mV/dec, which is less efficient in comparison to our system FeO(OH)-CoCeV-LTH which requires an overpotential of 227 mV at 10 mA/ cm^2 with a much lower Tafel slope value of 52 mV/dec **(Figure 4.14 (a-b))**.

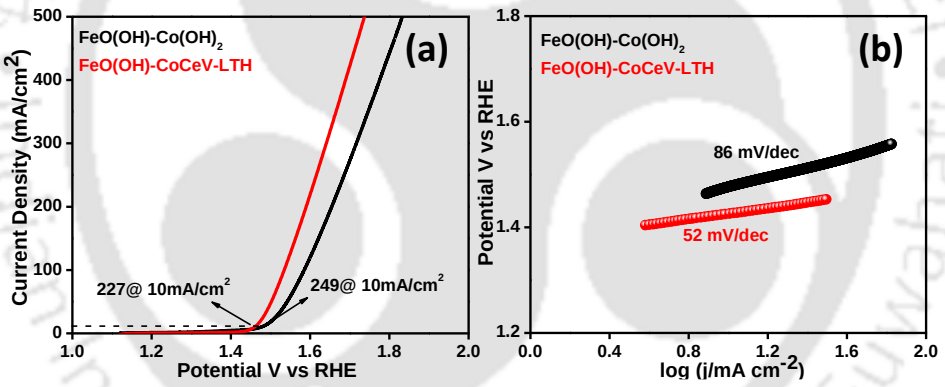

Figure 4.14 (a) LSV polarisation curves and (b) Tafel slope of FeO(OH)-$Co(OH)_2$ and FeO(OH)-CoCeV-LTH at a scan rate of 5mV/sec in 1M KOH.

4.3.13 Mechanistic Study

The cyclic voltammetry is measured taking mass activity into account, CV curve of FeO(OH) in **Figure 4.15 (a)** shows oxidation peaks at 0.25 V and reduction peak at -0.07 vs RHE at 5 mV/sec, corresponds to Fe^{2+}/ Fe^{3+} and Fe^{3+}/ Fe^{2+}, respectively. The composite FeO(OH)-CoCeV-LTH show a minor shift in oxidation and reduction peaks towards the direction of higher and lower potentials respectively, which is the result of the polarization

during a typical redox reaction.[31] Moreover, a relatively high redox current is observed for FeO(OH)-CoCeV-LTH, which indicates rapid redox reactions occur during the CV analysis.[32] As shown in **Figure 4.15 (b)**, CV curves are measured at a potential window of 0.7 to 1.6 V vs RHE, which exhibits two pairs of redox peaks, oxidation peaks at 1.1 V (P_1) and 1.43 V (P_2) and reduction peaks at 1.41 V (P_3) and 1.08 V (P_4).[33] These redox peaks P_3 and P_4 resulted from the reduction of Co(IV) to Co(III) and Co(III) to Co(II), respectively.[34, 35] In the composite FeO(OH)- CoCeV-LTH, the onset oxidation potential of Co^{3+}/Co^{4+} (1.41 V) is more negative as compared to CoCeV-LTH (1.43 V), signifying that Co^{3+} oxidation is more favorable on the composite. From reported literature, the higher oxidation states of Fe^{3+} and Co^{3+} species are known to contribute to an enhancement in HER and OER activity, which explains the higher activity of FeO(OH)-CoCeV-LTH towards the overall water splitting.[36-38] **Figure 4.15 (c)** represents the proposed redox reaction mechanism involved in FeO(OH) and CoCeV-LTH.

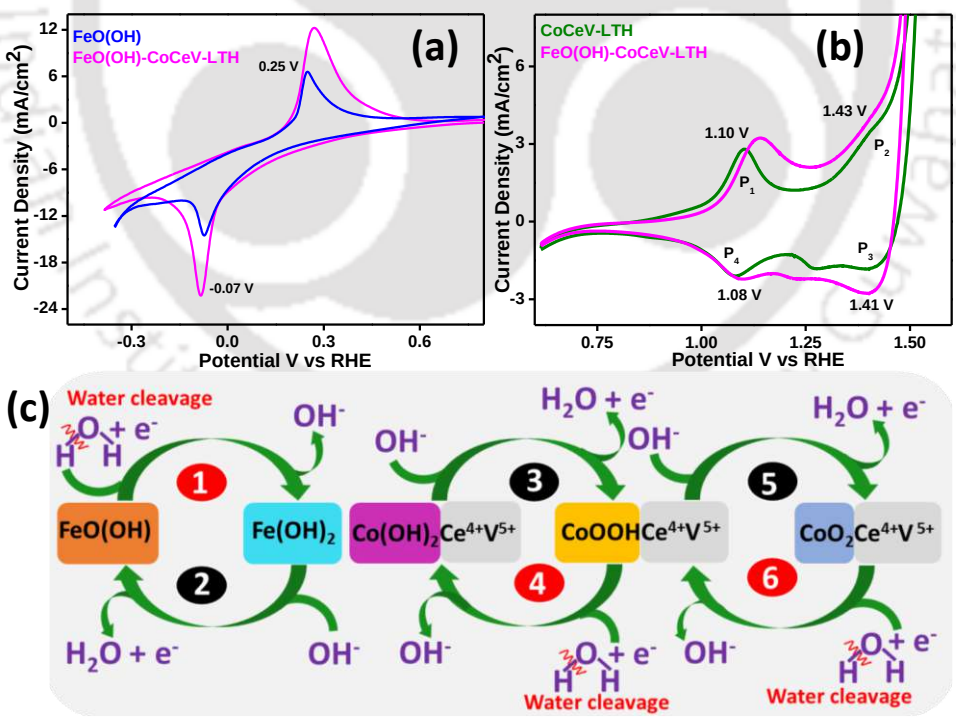

Figure 4.15 CV curves of (A) FeO(OH) and FeO(OH)-CoCeV-LTH, (B) CoCeV-LTH and FeO(OH)-CoCeV-LTH at the scan rate of 5mV/sec in 1M KOH taking mass activity into account. (C) Illustration of the possible reaction mechanism of FeO(OH) and CoCeV-LTH in 1M KOH.

In **step (1)** FeO(OH) by virtue of its water cleavage promoting OH attached to the metal center, which helps to keep the core metal center at its highest oxidation state, promotes the electron acceptor capability of Fe^{3+} and can get easily reduced to $Fe2^{+}$ ($Fe(OH)_2$) generating OH^-. In the subsequent reaction in **step (2)**, $Fe(OH)_2$ reacts with OH^- and regenerate FeO(OH), H_2O and e^- promoting water reduction to generate hydrogen. The redox process involved in **steps (1)** and **(2)** of **Figure 4.15 (c)** is shown in **equation (4.1)**:

$$FeO(OH) + H_2O + \bar{e} \rightleftarrows Fe(OH)_2 + OH^- \qquad \textbf{(4.1)}$$

In **step (3)**, Co^{2+} of $Co(OH)_2$ reacts with OH^- and gets oxidized to Co^{3+} (CoOOH) along with H_2O and e^-, and in the subsequent reduction process in **step (4)**, Co^{3+} of CoOOH accepts e^- to get reduced to Co^{2+} $Co(OH)_2$ with OH bond cleavage of H_2O to give OH^-. Lastly, in **step (5)**, Co^{3+} (CoOOH) gets oxidized to Co^{4+} (CoO_2) and give H_2O and e^-, and in the following redox process (**step (6)**), Co^{4+} (CoO_2) accepts e^- and get reduced to Co^{3+} (CoOOH) with another OH bond cleavage of H_2O molecule. **Equation (4.2)** and **(4.3)** represents the reaction process involved in **step (3) to (5):**

$$Co(OH)_2 + OH^- \rightleftarrows CoOOH + H_2O + \bar{e} \qquad \textbf{(4.2)}$$

$$CoOOH + OH^- \rightleftarrows CoO_2 + H_2O + \bar{e} \qquad \textbf{(4.3)}$$

The redox contributions of the cerium and vanadium are absent in the given potential range making them electrocatalytically inactive in the present system. However, their presence in the higher oxidation states makes hydroxides more active in the water cleavage processes. [39]

4.3.14 Long term operational stability

The long-term durability test for HER and OER of FeO(OH)-CoCeV-LTH is measured at a constant current density of 20 mA/cm^2 as shown in **Figure 4.16**. The result shows that

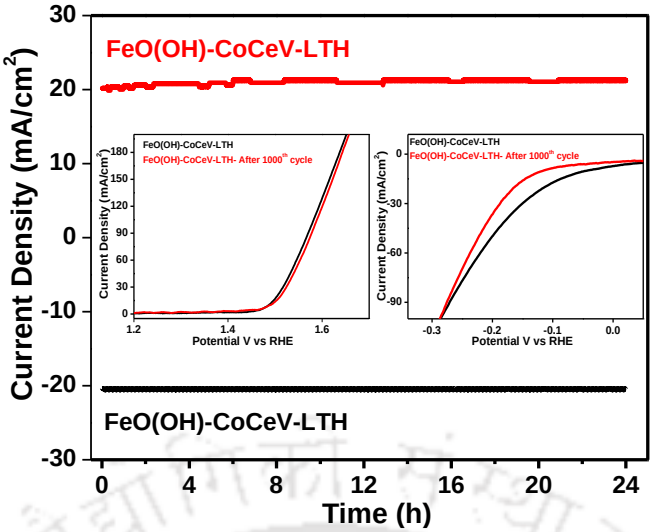

Figure 4.16 Chronoamperometric (i-t) curves of FeO(OH)-CoCeV-LTH at 20 mA/cm^2 for OER and HER, with an inset showing IV-curve before and after 1000th CV-cycle in 1M KOH.

FeO(OH)-CoCeV-LTH exhibits excellent electrochemical durability for 24 h of continuous operation, an inset in **Figure 4.16** shows that the LSV curves of FeO(OH)-CoCeV-LTH for OER shows negligible attenuation after subjecting to 1000 CV cycles, which further proof the stability of the system. Stability of FeO(OH)-CoCeV-LTH for HER in **Figure 4.16** shows an inset with polarization curve before and after subjecting to 1000 CV cycles. At lower current density, a small change in IV-curve is observed before and after CV measurement for HER, and at higher current density the IV-curve overlapped before and after CV cycle which proved the stability of the prepared catalyst.

To further understand the operational stability in terms of morphological and crystal structure of pre and post-electrochemical measurements, XRD, Raman and FESEM analysis are performed. The XRD pattern in **Figure 4.17 (a)** and Raman spectra **(Figure 4.17 (b))** indicates no change in crystalline structure during the HER and OER processes. The FESEM and HRTEM image (**Figure 4.17 (c-d)**) shows retention of the nanograin and nanoflakes structure post-analysis.

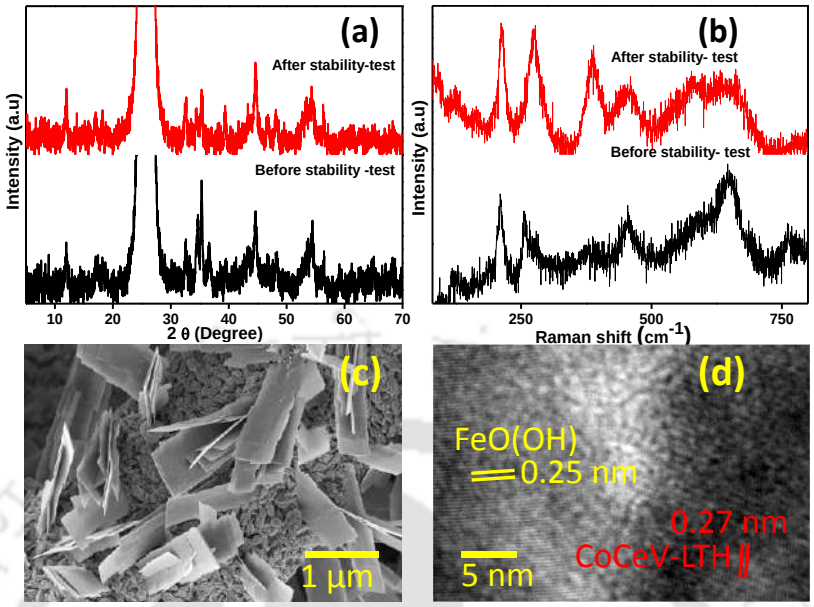

Figure 4.17 (a) XRD and (b) Raman spectral of FeO(OH)-CoCeV-LTH before and after stability test respectively, (c)Field Emission Scanning Electron Microscopy **(**FESEM) images and (d) High Resolution Transmission Electron Microscopy (HRTEM) image of FeO(OH)-CoCeV-LTH (after the stability-test).

4.4 CONCLUSION

In conclusion, the as fabricated FeO(OH)-CoCeV-LTH shows enhanced overall water splitting due to (i) Hierarchical FeO(OH) structures modified with CoCeV-LTH nanoflakes generating abundant electrochemical surface area and active sites (ii) The robust synergistic interaction between FeO(OH) and CoCeV-LTH accelerating the charge transfer and mass transport properties. (iii) The *in-situ* grown FeO(OH)-CoCeV-LTH directly onto carbon paper providing better mechanical adhesion and electrical conductivity. (iv) Highly open hierarchical structure facilitating the gas release during the HER and OER processes. (v) The increase in synergistic effect between FeO(OH) and CoCeV-LTH mainly contributes to the enhanced OER and HER activity.

4.5 REFERENCES

1. A. Sivanantham, P. Ganesan, A. Vinu, S. Shanmugam, *ACS Catal.*, 2020, **10**, 463– 493.
2. P. Du, R. Eisenberg, *Energy Environ. Sci.*, 2012, **5**, 6012– 602.
3. J. X. Feng, H. Xu, Y. T. Dong, S. H. Ye, Y. X. Tong, G. R. Li, *Angew. chem., Int. Ed.*, 2016, **55**, 3694– 3698.
4. H. Wang, H. Lee, Y. Deng, Z. Lu, P. Hsu, Y. Liu, D. Lin, Y. Cui, *Nat. Commun*., 2015, **6**, 7261.
5. M. Kuang, J. Zhang, D. Liu, H. Tan, K.- N. Dinh, L. Yang, H. Ren, W. Huang, W. Fang, J. Yao, X. Hao, J. Xu, C. Liu, L. Song, B. Liu, Q. Yan, *Adv. Energy Mater.*, 2020, **10,** 2002215.
6. C. Lv, X. Wang, L. Gao, A. Wang, S. Wang, R. Wang, X. Ning, Y. Li, D. W. Boukhvalov, Z. Huang, C. Zhang, *ACS Catal.*, 2020, **10**, 13323– 13333.
7. J. Guan, C. Li, J. Zhao, Y. Yang, W. Zhou, Y. Wang, G.-R. Li, *Appl. Catal. B: Environ.*, 2020, **269**, 118600.
8. Z. Zhao, W. Jin, L. Xu, C. Wang, Y. Zhang, Z. Wu, *J. Mater. Chem. A*, 2021, **9**, 12074.
9. X. Ji, C. Cheng, Z. Zang, L. Li, X. Li, Y. Cheng, X. Yang, X. Yu, Z. Lu, X. Zhang, H. Liu, *J. Mater. Chem. A*, 2020, **8**, 21199– 21207.
10. W. Xu, B. Wang, X. Ni, H. Lui, W. Wang, L. Zhang, H. Zhang, Z. Peng, Z. Liu, *ACS Appl. Mater. Interfaces*, 2021, **13**, 13838–13847.
11. Y. Liu, F. Le Formal, F. Boudoire, N. Guijarro, *ACS Appl. Energy Mater*., 2019, **2**, 6825– 6833.
12. Z. H. Zhang, B. B. He, L. J. Chen, H. W. Wang, R. Wang, L. Zhao, Y. S. Gong, *ACS Appl. Mater. Interfaces*, 2018, **10**, 38032– 38041.
13. J. Hu, S. W. Li, J. Y. Chu, S. Q. Niu, J. Wang, Y. C. Du, Z. H. Li, X. J. Han, P. Xu, *ACS Catal.*, 2019, **9**, 10705– 10711.

14. C. Feng, M. B. Faheem, J. Fu, Y. Xiao, C. Li, Y. Li, *ACS Catal.*, 2020, **10**, 4019– 4047.
15. J. Hu, C. Zhang, L. Jiang, H. Lin, Y. An, D. Zhou, M. K. H. Leung, S. Yang, *Joule*, 2017, **1**, 383– 393.
16. Q. Liu, J. Huang, X. Zhang, L. Cao, D. Yang, J.-H. Kim, L. Feng, *ACS Sustainable Chem. Eng.*, 2020, **8**, 16091 —16096.
17. J. Bao, Z. Wang, J. Xie, L. Xu, F. Lei, M. Guan, Y. Zhao, Y. Huang, H. Li, *Chem. Commun.*, 2019, **55**, 3521– 3524.
18. Y. Yang, L. N. Dang, M. J. Shearer, H. Y. Sheng, W. J. Li, J. Chen, P. Xiao, Y. H. Zhang, R. J. Hamers, S. Jin, *Adv. Energy Mater.*, 2018, **8**, 1703189.
19. K. Dinh, P. Zheng, Z. Dai, Y. Zhang, R. Dangol, Y. Zheng, B. Li, Y. Zong, Q. Yan, *Small*, 2018, **14**, 1703257.
20. Y. Hu, Z. Wang, W. Liu, L. Xu, M. Guan, Y. Huang, Y. Zhao, J. Bao, H.-M. Li, *ACS Sustainable Chem. Eng.*, 2019, **7**, 16828– 16834.
21. T. Wang, Z. Jiang, K. H. Chu, D. Wu, B. Wang, H. Sun, H. Y. Yip, T. An, H. Zhao, P. K. Wong, *ChemSusChem*, 2018, **11**, 1365– 1373.
22. M. S. P.-Chana, U. S.-Kuri, R. S.-Zeferino, I. I. R.-Lópeza, A. E.-Morales, *Appl. Clay Sci.*, 2021, **210**, 106159.
23. X. Guo, F. Zhang, D. G. Evans, X. Duan, *Chem. Commun.*, (Cambridge, U. K.) 2010, **46**, 5197– 5210.
24. M. A. Sayeed, A. P. O'Mullane, *J. Mater. Chem. A*, 2017, **5**, 23776– 23784.
25. F. N. I. Sari, S. Abdillah, J.-M. Ting. *Chem. Eng. J.*, 2021, **416**, 129165.
26. J. Hu, S. W. Li, J. Y. Chu, S. Q. Niu, J. Wang, Y. C. Du, Z. H. Li, X. J. Han, P. Xu, *ACS Catal.*, 2019, **9**, 10705– 10711.
27. J. L. Xia, H.-Y. Zhao, B. L. Huang, L. Xu, M. Luo, J. Wang, F. Luo, Y. P. Du, C. H. Yan, *Adv. Funct. Mater.*, 2020, **30**, 1908367.

28. P. F. Liu, S. Yang, B. Zhang, H. G. Yang, *ACS Appl. Mater. Interfaces*, 2016, **8**, 34474– 34481.
29. J. Chen, F. Zheng, S.-J. Zhang, A. Fisher, Y. Zhou, Z. Wang, Y. Li, B.-B. Xu, J.-T. Li, S.-G. Sun, *ACS Catal.*, 2018, **8**, 11342– 11351.
30. S. Hao, L. Chen, C. Yu, B. Yang, Z. Li, Y. Hou, L. Lei, X. Zhang, *ACS Energy Lett.*, 2019, **4**, 952– 959.
31. S. Chen, G. Yang, H. Zheng, *Electrochim. Acta*, 2016, **220**, 296– 303.
32. G. Nagaraju, G. S. R. Raju, Y. H. Ko, J. S. Yu, *Nanoscale*, 2016, **8**, 812– 825.
33. M. Fracchia, A. Visibile, E. Ahlberg, A. Vertova, A. Minguzzi, P. Ghigna, S. Rondinini, *ACS Appl. Energy Mater.*, 2018, **1**, 1716– 1725.
34. B. Guo, T. Li, H. Hu, *J. Appl. Electrochem.*, 2016, **46**, 403– 421.
35. A. Moysiadou, S. Lee, C.-S. Hsu, H. M. Chen, X. Hu, *J. Am. Chem. Soc.*, 2020, **142**, 11901– 11914.
36. J. Chen, J. Xu, S. Zhou, N. Zhao, C.-P. Wong *Nano Energy*, 2016, **21**, 145– 153.
37. H. -J. Zhang, C. Cai, S. Zhang, Z. –F. Ma, Y. Xue, W. Yan, J. Zhang, *ACS Appl. Energy Mater*., 2021, **4**, 4165–4172.
38. P. Li, X. Duan, Y. Kuang, Y. Li, G. Zhang, W. Liu, X. Sun, *Adv. Energy Mater.*, 2018, **8**, 1703341, DOI: 10.1002/aenm.201703341
39. H. Xu, C. Shan, X. Wu, M. Sun, B. Huang, Y. Tang, C.-H. Yan, *Energy Environ. Sci.*, 2020, **13**, 2949– 2956.

CHAPTER 5

Tapping the potential of high-valent Mo and W metal centres for dynamic electronic structure in multi-metallic FeVO(OH)/Ni(OH)$_2$ for water splitting

Rationally designing a noble metal-free electrocatalyst for OER and HER is pivotal for large-scale energy generation via water splitting. Multi-metallic electrocatalyst FeVO(OH)/Ni$_{0.86}$Mo$_{0.07}$W$_{0.07}$(OH)$_2$ aiming at tuning the electronic structure is fabricated, gives a huge improvement in water splitting reaction kinetics. By taking the advantage of (ē–ē) repulsions at t_{2g} level, we have introduced high-valent Mo and W to provide a viable path for π–electron donation from oxygen 2p orbitals to vacant Mo and W orbitals for a dynamic electronic structure and interfacial synergistic effect. The hybrid catalyst FeVO(OH)/NiMoW(OH)$_2$ shows an intrinsic activity and durability towards OER and HER.

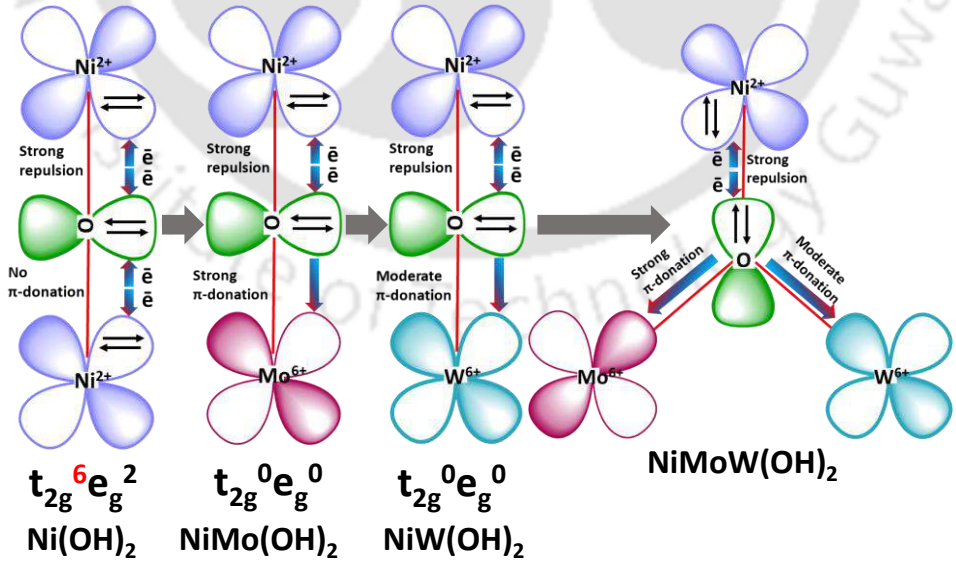

(Manuscript under preparation)

5.1 INTRODUCTION

With low CO_2 emission and high energy density, hydrogen fuel is considered a cleaned and sustainable alternative source to the traditional fossil fuels.[1] Electrocatalytic overall water splitting is pondered among the most promising, efficient, and stable strategies to generate clean and renewable hydrogen and oxygen fuels.[2] Electrocatalytic overall water splitting (OWS) is a kinetically sluggish and thermodynamically an uphill process, in which hydrogen evolution reaction (HER) involves two-electron transfer and oxygen evolution reaction (OER) involves a multi-step four consecutive electron transfer processes.[3] In an alkaline medium, HER is a limiting factor which involves adsorption of water molecules and successive O-H bond breaking with the release of one electron via Volmer reaction, and the subsequent hydrogen generation proceeds either through a Tafel or Heyrovsky step. For an efficient HER electrocatalyst, the Gibb's free energy change (ΔG_{H^*}) should be close to zero to have optimum adsorption and desorption of H and H_2.[4,5] Notably, a noble metal-based catalyst such as RuO_2/IrO_2 for OER and Pt/C for HER remain the most efficient electrocatalyst due to their high current density and low energy barrier. However, the high cost and scarcity of noble metal-based catalysts make it unfavourable for their widespread practical applications.[6-8]

Over the past decades, researchers have explored catalytically active, cheap, abundant, and robust non-precious electrocatalysts to replace noble metals for electrocatalytic overall water splitting. The first row of transition-metal oxide (α- Fe_2O_3:V-NiFe LDH),[9] (oxy)hydroxide (FeOOH@$NiCo_2O_4$),[10] phosphide (FeP/FeOOH),[11] sulfide (FeOOH/Ni_3S_2)[12] and nitride (FeOOH/Ni_3N)[13] based systems have attracted attention for their low cost, easy availability, earth abundance, durability and chemical stability to replace precious metals.[9-13] Recent studies reported that bi or trimetallic system exhibits better intrinsic catalytic properties, resulting from the redistribution of the electrons.[14] For practical applications, Fe-based oxyhydroxide has great potential due to its low cost and abundance, especially bimetallic iron

oxyhydroxide such as FeNiOOH, and FeCoOOH exhibits excellent electrocatalytic properties.[8] Besides, the Fe-based system with its variable oxidation states readily adsorbs OH^- species and possesses high intrinsic electrocatalytic activity.[8, 15] However, Fe based catalyst suffers from poor intrinsic conductivity and sluggish oxidation kinetics.[8, 9] Numerous strategies have been developed like surface modification, doping of metal atom, morphological variation, phase transition, heterostructure formation for improving the electrocatalytic activities.[3, 10, 14]

Multi-metallic transition metal oxides and hydroxides with their unique electronic configuration have been reported to show higher OER performance. Doping with transition metal atoms having empty or partially filled d orbitals is known to improve the π- electron back donation causing the active bond to be easily available to participate in the electrocatalytic activity there by increasing the performance.[3] Dual metal doping is found to efficiently change the electronic structural environment as compared to single metal doping, causes a reduction in the water dissociation energy and optimizes the adsorption energy for the reaction intermediates during the HER and OER processes.[17] The d^0 transition metals (such as W^{6+}, Ni^{4+}, V^{5+}, Fe^{4+}, Mo^{+5}) with high oxidation states can accommodate incoming electrons are found to generate optimal bond length for reaction intermediates, which accelerates the overall water splitting.[18, 19] Doping of molybdenum (Mo) is reported to enhance catalytically surface-active sites and decreases the path of ionic transport which facilitates the HER.[5] Meanwhile, the higher oxidation state of W^{6+} acts as a strong Lewis acid and withdraws electron from the neighbouring atom to generate additional active centers.[20] Another important strategy to enhance electrocatalytic performance is designing of heterostructure, to generate a catalytically active centre, by modification of electronic structure to facilitate charge-transfer kinetics.[3]

Inspired by the aforementioned virtues, we have designed a binder-free heterostructure strategy utilizing FeVO(OH)/$Ni_{0.86}Mo_{0.07}W_{0.07}(OH)_2$ onto a commercial carbon paper (CP) substrate via a two-step hydrothermal synthesis, in which the CP offers better electrical

conductivity and faster electron transport between the electrode and the active sites. The dual-metal doping of Mo and W into $Ni(OH)_2$ facilitates a synergistic effect for long-term durability and generates additional active centres, thereby, increasing the electrocatalytic activity.[21] The co-doping provides optimum adsorption energies for reaction intermediates, thereby decreasing the kinetic energy barrier for HER and OER. The experimental data shows that the hybrid heterostructure $FeVO(OH)/Ni_{0.86}Mo_{0.07}W_{0.07}(OH)_2$ requires 231 mV for OER and 156 mV for HER to drive 20 mA/cm^2 with a corresponding Tafel slope value of 24 mV/dec for OER and 67 mV/dec for HER respectively. The heterostructure $FeVO(OH)/Ni_{0.86}Mo_{0.07}W_{0.07}(OH)_2$ displays a potential of 1.48 V @ 20 mA/cm^2 for overall water splitting, with long-term durability for about 48 h.

5.2 EXPERIMENTAL SECTION

5.2.1 Carbon paper (CP) treatment

The substrate carbon paper (CP) is pre-treated hydrothermally in a solution mixture of nitric acid and sulphuric acid (2:1) at 100° C for 2 h to enhance the hydrophilicity and removed impurities. Then, subsequent washing of CP is done with distilled water, acetone, and ethanol respectively. The cleaned CP is dried at 70 °C in a vacuum oven overnight.

5.2.2 Fabrication of FeVO(OH)@CP

$FeCl_3$ (1mM), NH_4F (1mM), and CH_4N_2O (3 mM) are dissolved in 15 ml of distilled H_2O under magnetic stirring to obtain solution A. Then, in another beaker NH_4VO_3 (1mM) is dispersed in 10 ml of H_2O and magnetically stirred at 80 °C for 5 min which is denoted as solution B. Then, the above two solutions are mixed together and transferred to a 50 ml Teflon-lined stainless-steel autoclave jacket with carbon paper (CP) as the substrate which are places at a certain angle, and is hydrothermally reacted at 150 °C for 4 h. Finally, the as synthesize

product FeVO(OH)@CP is cleaned subsequently with deionized water and ethanol and dried at 70 °C in a vacuum oven for overnight.

5.2.3 Fabrication of NiMoW/CP and FeVO(OH)/NiMoW/CP

Different molar concentrations of $Ni(NO_3)_2$. $6H_2O$, WCl_6, $(NH_4)_6Mo_7O_{24}\cdot 4H_2O$, and CH_4N_2O (3 mM) are dissolved in 25 ml of deionized H_2O and magnetically stirred for 30 min. Then, the homogenous solution is transferred to an autoclave reactor and hydrothermally treated at 120 °C for 12 h with carbon paper substrate. Finally, NiMoW/CP is subsequently cleaned with H_2O and ethanol and vacuum dried at 70 °C for 12 h. The composite sample FeVO(OH)/NiMoW/CP is synthesized following the same reaction condition, and used as synthesized FeVO(OH)@CP as the substrate instead of CP.

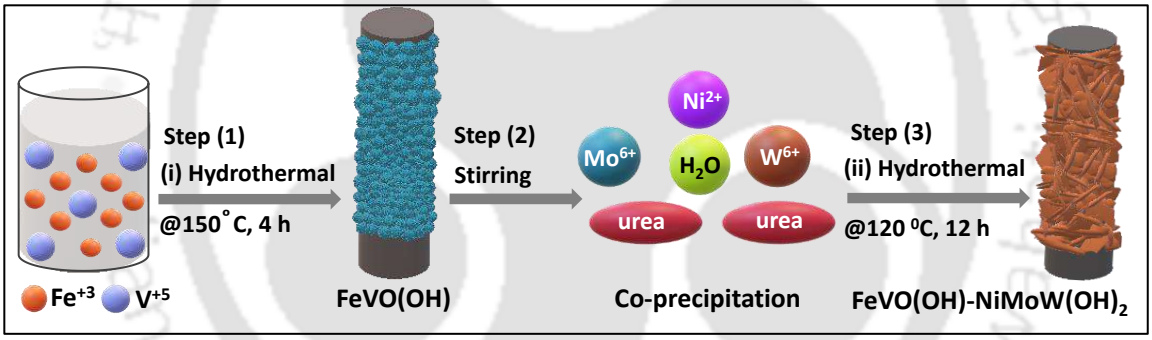

Scheme 5.1 Illustration of the fabrication process of FeVO(OH)/NiMoW(OH)$_2$ onto carbon paper (CP).

Hierarchical FeVO(OH)/NiMoW(OH)$_2$ heterostructure is synthesized via a two-step hydrothermal method onto the bare carbon paper (CP) substrate as shown in **Scheme 5.1**. The Fe and V precursors are first grown onto CP to form cauliflower-like FeVO(OH) at 150℃ for 4 h (step (1)), and in step (2) FeVO(OH)/CP served as a template to grow NiMoW(OH)$_2$ nanosheets at 120℃ for 12 h.

5.3 RESULTS AND DISCUSSIONS

5.3.1 Powder X-Ray Diffraction (PXRD) and Raman Analysis

The crystallinity of the as-synthesized samples is shown in **Figure 5.1 (a)**. The XRD peaks at 2θ value of 35.5, 40.6, 61.3, and 64.0 correspond to (023), (123), (153), and (006) lattices plane of $FeV_2O_6H_{0.5}$ (JCPDS-No-01-071-1320) which is assigned as FeVO(OH). **Figure 5.1 (a)** shows the XRD peaks of $Ni_{0.86}Mo_{0.07}W_{0.07}(OH)_2$ assigned as $NiMoW(OH)_2$, which shows a diffraction plane of (100), (101), (102), and (111) at 2θ value of 34.75, 39.85,

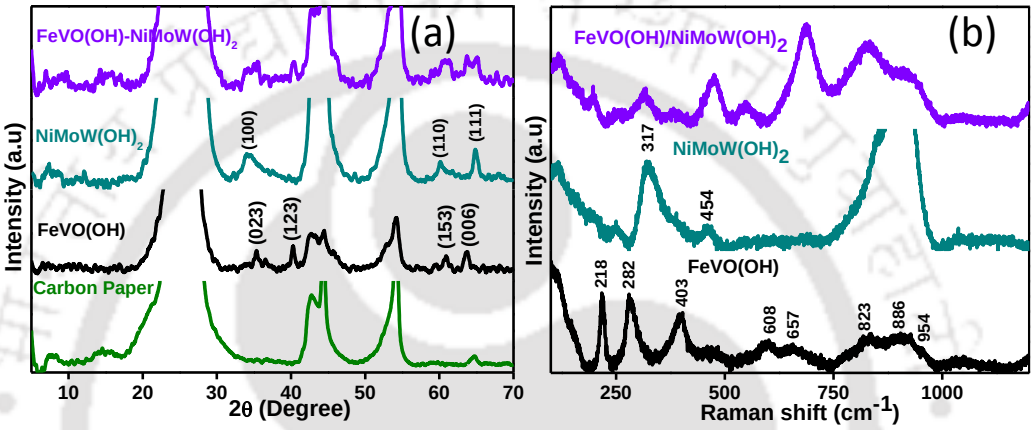

Figure 5.1 (a) XRD and (b) Raman spectra of FeVO(OH), $NiMoW(OH)_2$, and $FeVO(OH)/NiMoW(OH)_2$

53.03 and 62.7 respectively of β-$Ni(OH)_2$ (PDF#14-0117).[14] Raman spectra are performed to understand the elemental composition of the as-synthesized sample as shown in **Figure 5.1 (b).** The Raman scattering peaks at 218, 282, 403, 608, and 657 cm^{-1} in FeVO(OH) are assignable to FeOOH. The Raman peaks observed at 282 and 657 cm^{-1} in FeVO(OH) and $FeVO(OH)/NiMoW(OH)_2$ designates the presence of layered structure and the asymmetric stretching vibration of metal and hydroxide group respectively. The Raman peaks at 823 cm^{-1} correspond to the inactive mode of the V-O stretching bond and peaks at 886 and 954 cm^{-1} indicate the presence of hydrated vanadium oxide.[19] For $NiMoW(OH)_2$, the characteristic Raman bands at 317 and 454 cm^{-1} for $E_{g(T)}$ and A_{1g} mode correspond to translational lattice and stretching vibration of Ni–OH in $Ni(OH)_2$ respectively.[20, 21]

5.3.2 X-Ray Photoelectron Spectroscopy (XPS) Analysis

X-ray photoelectron spectroscopy (XPS) is performed to understand the surface composition and electronic states of the core levels of the elements of the as-prepared electrocatalysts, and all peaks are calibrated with C 1s spectra at 284.7 eV. As shown in **Figure 5.2 (a)**, each peak of the V 2p spectrum of FeVO(OH) can be deconvoluted into a doublet, the BE of the first doublet of V $2p_{3/2}$ is at 516.94 eV and 516.46 eV of V assignable to +4 and +5 oxidation state respectively. The second doublet of V $2p_{1/2}$ is located at 523.52 eV and 524.52 eV of V in +4 and +5 oxidation states, confirming that vanadium exists in mixed-valent state in the composite.[22] The V 2p XPS spectrum of FeVO(OH)/NiMoW(OH)$_2$ has peaks located at 516.46 eV (V $2p_{3/2}$) and 523.81 eV (V $2p_{1/2}$) of V (+4), and peaks at 517.11 eV (V $2p_{3/2}$) and 524.89 eV (V $2p_{1/2}$) corresponds to V (+5) respectively. In the composite, the V 2p show a positive shift in BE due to an electronic interaction between FeVO(OH) and

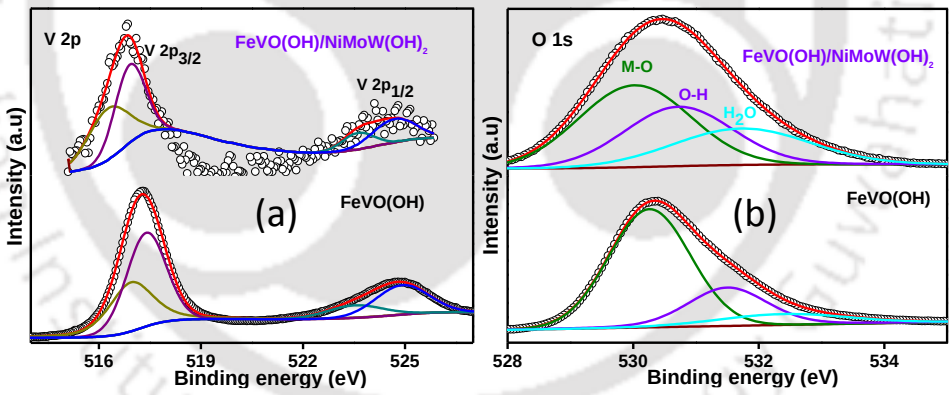

Figure 5.2 X-ray photoelectron spectroscopy (XPS) spectra of (a) V 2p and (b) O 1s of FeVO(OH) and FeVO(OH)/NiMoW(OH)$_2$.

FeVO(OH)/NiMoW(OH)$_2$.[22, 23] The O 1s in **Figure 5.2 (b)** of FeVO(OH) can be deconvoluted into three peaks located at 530.3 eV, 531.5 eV, and 532.4, which are assignable to the lattice oxygen (M–O), lattice OH group (M–OH) and adsorbed H_2O molecules respectively. In the composite FeVO(OH)/NiMoW(OH)$_2$, the O 1s core-level spectra show a negative shift in BE, which indicates an electronic interaction between the pristine FeVO(OH) and NiMoW(OH)$_2$.[22]

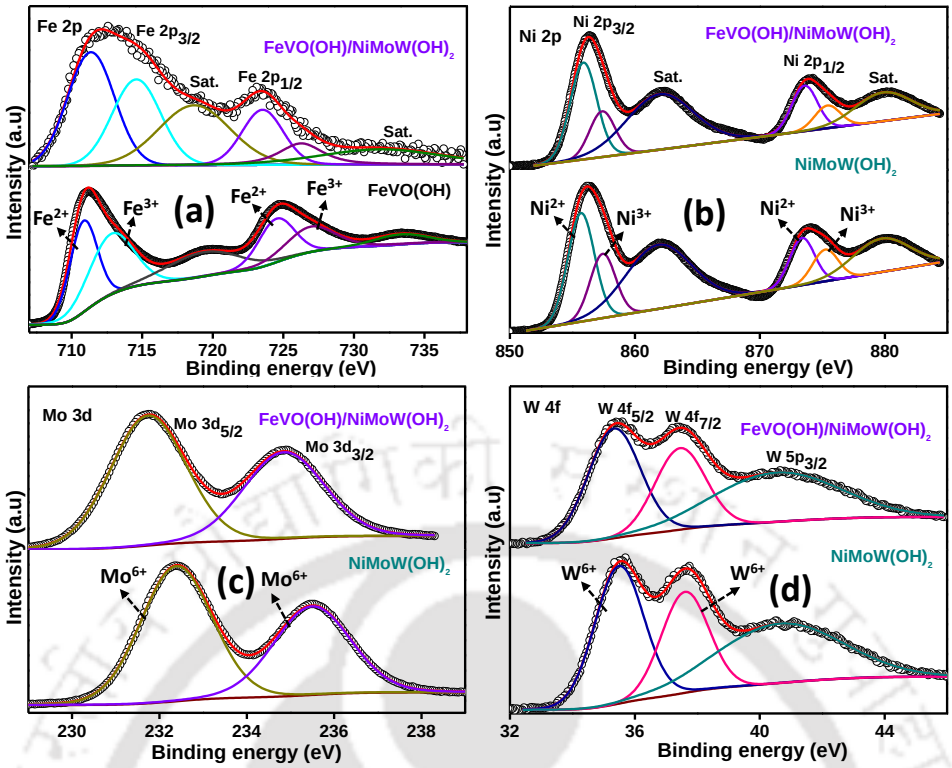

Figure 5.3 X-ray photoelectron spectroscopy (XPS) spectra of (a) Fe 2p of FeVO(OH) and FeVO(OH)/NiMoW(OH)$_2$, and XPS spectra of (b) Ni 2p of Ni(OH)$_2$, NiW(OH)$_2$, NiMo(OH)$_2$ and NiMoW(OH)$_2$, (c) Mo 3d and (d) W 4f of NiMoW(OH)$_2$ and FeVO(OH)/NiMoW(OH)$_2$.

The Fe 2p XPS spectra of FeVO(OH) are displayed in **Figure 5.3 (a)**, with binding energy (BE) at 710.8 eV ($2p_{3/2}$) and 724.5 eV ($2p_{1/2}$) corresponding to Fe in +3 oxidation state with a satellite peak at 719.34 eV. The XPS peaks located at 712.8 eV ($2p_{3/2}$) and 726.9 ($2p_{1/2}$) eV are assignable to Fe^{2+}.[22] The Fe 2p XPS spectra of FeVO(OH)/NiMoW(OH)$_2$ shows a red shift in BE by ~ 0.3 eV from FeVO(OH), suggesting a change in the electronic structure environment of Fe 2p after modification with NiMoW(OH)$_2$.[13,22]

The Ni 2p XPS spectra of pristine Ni(OH)$_2$ in **Figure 5.3 (b)** can be deconvoluted into two binding energies at 855.12 eV (Ni $2p_{3/2}$) and 872.64 eV (Ni $2p_{1/2}$) which corresponds to Ni^{2+} with a shakeup satellite peak at 861.0 eV. The Ni $2p_{3/2}$ peak located at 856.36 eV and Ni $2p_{1/2}$ at 874.13 eV indicate the presence of Ni in +3 oxidation state with a corresponding broad satellite peak at 879.05 eV of Ni(OH)$_2$. As shown in **Figure 5.3 (b)**, the introduction of individual $W^{6+}$and Mo^{6+} shift the Ni 2p peak towards higher BE by ~0.4 eV and ~0.7 eV of

$NiW(OH)_2$ and $NiMo(OH)_2$ respectively, which symbolise a strong electronic interaction between W^{6+}, Mo^{6+} and pristine $Ni(OH)_2$. The strong electronic interaction is beneficial for charge transfer during the electrochemical reactions. Meanwhile, the shift toward higher BE energy signify the existence of Ni in mixed oxidation state, which allow Mo and W to exist in high oxidation states of +6 with empty d-orbital, which optimized adsorption energy of reactions intermediate, thereby enhancing the electrocatalytic processes.[20, 24, 25]

The Mo 3d XPS spectra is shown in **Figure 5.3 (c)**. Two well-defined peaks are due to spin-orbit splitting of Mo $3d_{5/2}$ and $3d_{3/2}$ at 232.4 eV and 235.5 eV respectively with no-satellite signature indicating the presence of Mo^{6+} in d^0 ($t_{2g}^0e_g^0$) system in $NiMoW(OH)_2$. The Mo 3d core-level spectra of $FeVO(OH)/NiMoW(OH)_2$ shows two major peaks centred at 232.0 eV ($3d_{5/2}$) and 235.15 eV ($3d_{3/2}$).[15, 21] The W 4f XPS spectrum of $NiMoW(OH)_2$ in **Figure 5.3 (d)** exhibits two peaks at 35.5 eV ($4f_{7/2}$) and 37.61 eV ($4f_{5/2}$), showing the presence of W^{+6} of d^0 ($t_{2g}^0e_g^0$) system in the doped sample. In the composite, Mo 3d and W 4f show a negative shift in BE which indicates an electronic interaction between $NiMoW(OH)_2$ and pristine FeVO(OH).

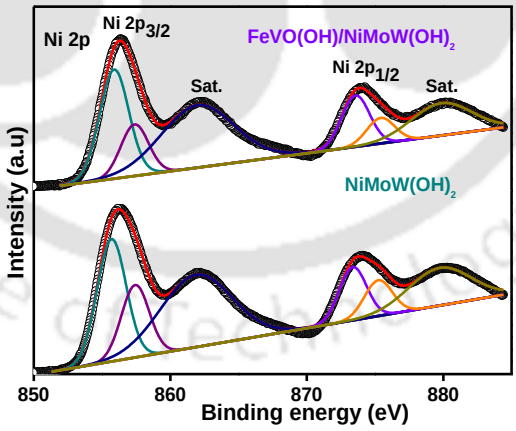

Figure 5.4 X-ray photoelectron spectroscopy (XPS) spectra of Ni 2p of $NiMoW(OH)_2$ and $FeVO(OH)/NiMoW(OH)_2$.

The Ni 2p XPS spectrum **(Figure 5.4)** of Mo^{6+} and W^{6+} co-doped $Ni(OH)_2$ can be deconvoluted into two peaks with the binding energy of Ni $2p_{3/2}$ located at 855.48 eV and Ni

$2p_{1/2}$ at 873.27 eV corresponds to divalent nickel. The XPS peak fitting with the BE of 857.15 eV ($2p_{3/2}$) and 875.13 eV ($2p_{1/2}$) can be ascribed to Ni^{3+} of $NiMoW(OH)_2$ along with their corresponding "shake up" satellite peaks at 861.8 eV and 879.6 eV.[14, 23] For the composite $FeVO(OH)/NiMoW(OH)_2$, the Ni 2p XPS spectra shifts to higher binding energy by ~ 0.3 eV signifying the existence of Ni in mixed oxidation state, and a change in charge density and strong interfacial interaction between $NiMoW(OH)_2$ and FeVO(OH), and concomitant increases in OER activity.[16, 21, 24, 25]

5.3.3 Electronic Coupling Study

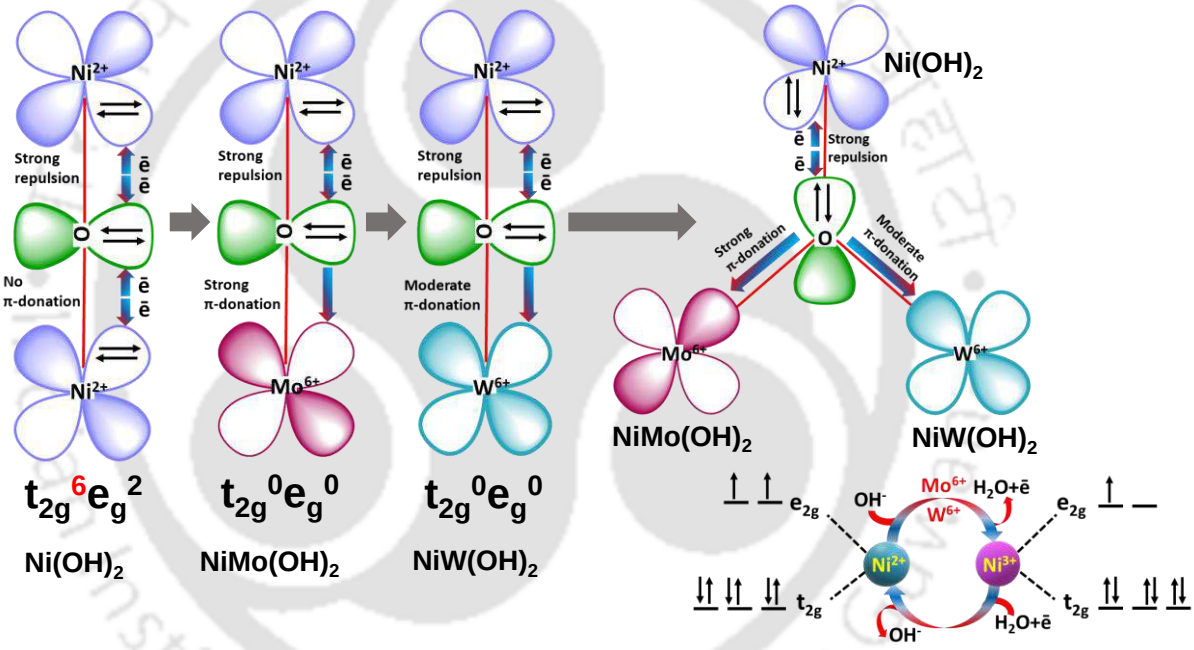

Figure 5.5 Schematic illustrations of the electronic coupling between Ni^{2+}, Mo^{6+} and W^{6+}.

From the XPS analysis it is clear that the valence electronic configuration of Ni^{2+} and Ni^{3+} are $3d^8$ ($t_{2g}^6e_g^2$) and $3d^7$ ($t_{2g}^6e_g^1$) respectively, and the electronic configurations of Mo^{6+} and W^{6+} are $4d^0$ ($t_{2g}^0e_g^0$) and $5d^0$ ($t_{2g}^0e_g^0$) respectively. The proposed electronic coupling at the interface between Ni, Mo, W, and O is illustrated in **Figure 5.5**.[26-31] The Ni^{2+} with its completely occupied 3d orbital (t_{2g}) exhibits strong ē-ē repulsions between filled t_{2g}^6 electron of Ni^{2+} and lone pair electrons on the bridged O^{2-}. Therefore, a partial electron transfer

inevitably occurs from the occupied t_{2g} orbital of Ni^{2+} to empty 4d/5d orbitals of Mo^{6+} and W^{6+} via strong π-donation of the bridged O^{2-}.[26- 31] The strong π-electron donation from O^{2-} to unoccupied d-orbital weakens the ē-ē repulsion between t_{2g}-electrons of Ni^{2+} and the bridge π-electrons of O^{2-} ions, facilitating the electron transfer from Ni^{2+} to Mo^{6+} and W^{6+} via bridged orbital of O^{2-}.[30] The increase in electron density around Mo^{6+} optimize the Ni-O bond strength and accelerate HER. The delocalization of electrons with the incorporation of Mo^{6+} into $Ni(OH)_2$ crystal structure optimize the free energy of formation of reaction intermediates and accelerate the OER kinetics.[29] The d^0 system of W^{6+} can act as a strong Lewis acid and draw neighbouring electrons from Ni, which allows Ni to exist in variable oxidation states in the system and enhanced the water oxidation.[20] The electronic coupling optimized redistribution of π-symmetry electron among Ni^{2+}, Mo^{6+} and W^{6+} at the interface, which results to a favourable adsorption/desorption of reaction intermediates and facilitates the OER and HER reactions.[26,29] The high valence state of Mo^{6+} and W^{6+} stabilize the active Ni redox species and accelerates the overall water splitting kinetics.[27]

5.3.4 Morphological Analysis

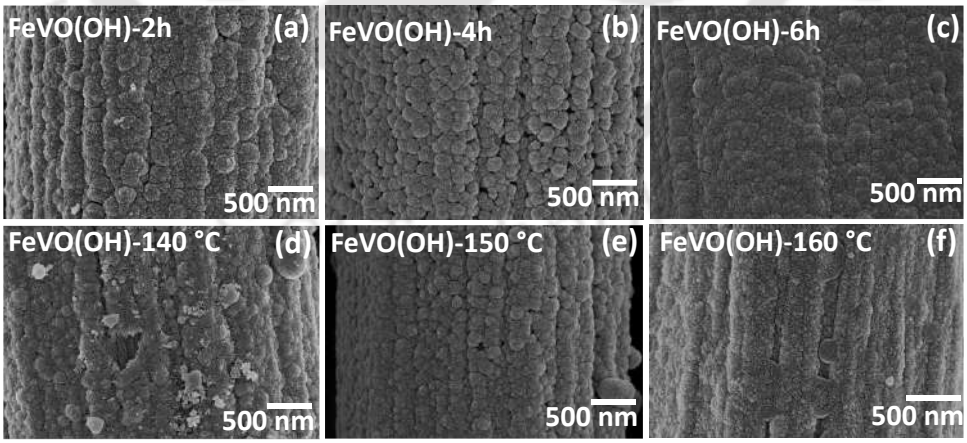

Figure 5.6 Field Emission Scanning Electron Microscopy (FESEM) images of (a-c) FeVO(OH) for 2h, 4h and 6h, and (d-f) FeVO(OH) for 140° C, 150° C and 160° C respectively.

Figure 5.6 (a)-(c) shows the change in morphology of FeVO(OH) with time variation, in which the nano particles grow more compact with increases in time from 2 h to 6 h. The effect of temperature on the morphology of FeVO(OH) is also studied. As shown in **Figure 5.6 (d)-(f)**, by increasing the hydrothermal reaction temperature from 140° C to 160° C, the cauliflower morphology of FeVO(OH) diminish to form densely packed nanoparticles.

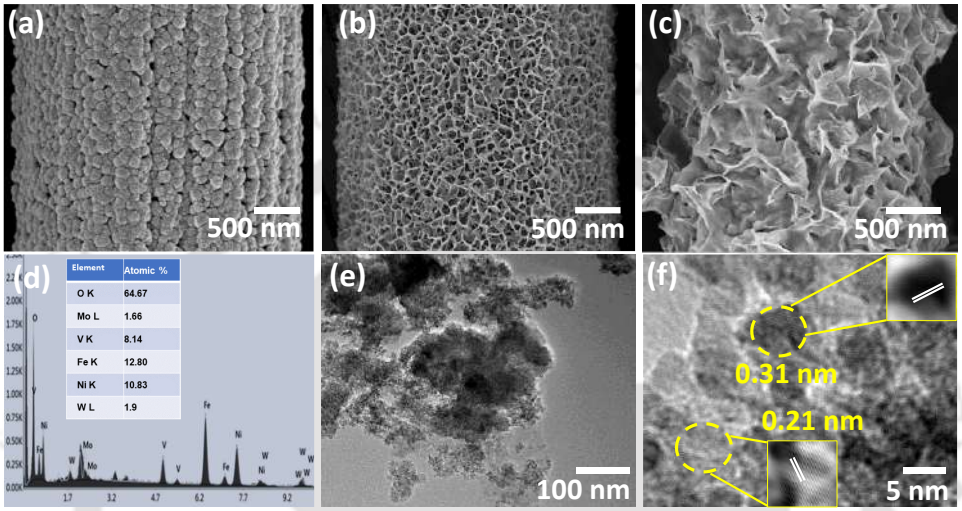

Figure 5.7 Field Emission Scanning Electron Microscopy (FESEM) images of (a) FeVO(OH) for 4h, (b) NiMoW(OH)$_2$, (c) FeVO(OH)/NiMoW(OH)$_2$, and (d) electron-dispersive X-ray (EDX) spectrum of FeVO(OH)/NiMoW(OH)$_2$. Transmission Electron Microscopy (TEM) image of (e) FeVO(OH)/NiMoW(OH)$_2$, and High-Resolution Transmission Electron Microscopy (HRTEM) image of (f) FeVO(OH)/NiMoW(OH)$_2$.

The morphology and elemental composition of the as-synthesized electrocatalyst are characterized by field emission scanning electron microscopy (FESEM) and transmission electron microscopy (TEM). FESEM results as shown in **Figure 5.7 (a)** demonstrates the pristine FeVO(OH) anchored onto CP substrate in cauliflower-like arrays. The morphology of NiMoW(OH)$_2$ in **Figure 5.7 (b)** shows 3-D interconnected nanosheets uniformly distributed over the CP substrate. In the composite FeVO(OH)/NiMoW(OH)$_2$ (**Figure 5.7 (c)**), NiMoW(OH)$_2$ nanosheets partially covered the surface of FeVO(OH)/CP nanoarrays. The interconnected NiMoW(OH)$_2$ nanosheets allows a favorable electrolyte diffusion between the

nanosheets, and shorten the diffusion length of ionic transport to enhance the electrochemical reactions.[14, 16] The hybrid heterostructure FeVO(OH)/NiMoW(OH)$_2$ facilitates the electrode/electrolyte diffusion and enhances the charge transfer kinetics. The energy dispersive X-ray (EDX) analysis of FeVO(OH)/NiMoW(OH)$_2$ in **Figure 5.7 (d)** displays the presence of all elemental atoms (at.%): Fe (12.8 %), V (8.14 %), Ni (10.83 %), Mo (1.66 %), W (1.9 %), O (64.67 %). The EDX further confirms the elemental ratio of dopants in Ni(OH)$_2$, which is consistent with the precursors added during the hydrothermal synthesis with in the experimental error. The transmission electron microscopy (TEM) image **(Figure 5.7 (e))**, demonstrates the presence of FeVO(OH) nanoarrays and NiMoW(OH)$_2$ nanosheets. The high-resolution transmission electron microscopy (HRTEM) image of FeVO(OH)/NiMoW(OH)$_2$ in **Figure 5.7 (f)** displays interplanar distances of 0.31 nm and 0.21 nm indexed to the (110) and (101) planes of FeVO(OH) and NiMoW(OH)$_2$ respectively.[16] Furthermore, the scanning transmission electron microscopy (STEM) image (**Figure 5.8 (a)**) and the corresponding elemental mapping shows the presence and uniform distribution of Fe, V, Ni, Mo, W, and O elements in the composite (**Figure 5.8 (b)-(g)**).

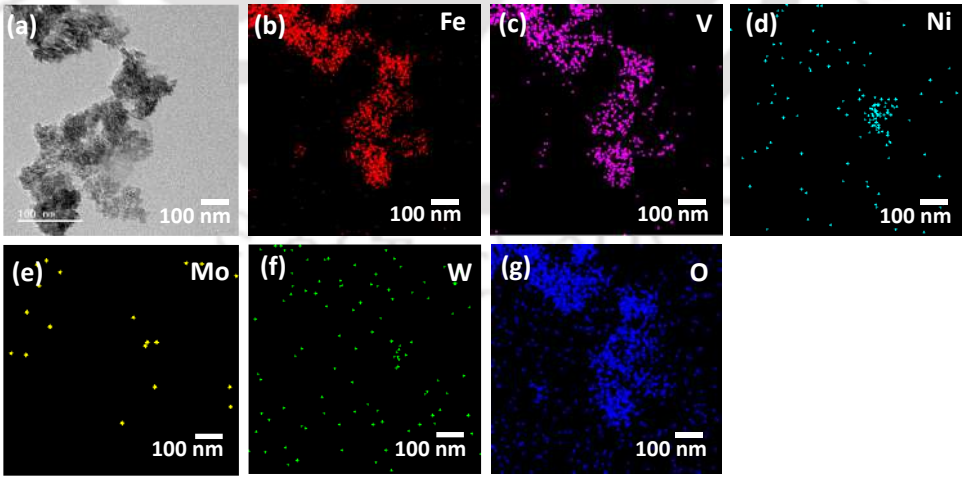

Figure 5.8 Scanning Transmission Electron Microscopy (STEM) image and the corresponding EDX elemental mapping of FeVO(OH)/NiMoW(OH)$_2$ (i)-(n).

5.3.5 *J-V* Optimization Curve

To understand the role of hydrothermal reaction time and reaction temperature on the electrocatalytic activity of FeVO(OH), we have studied the OER and HER activity of pristine FeVO(OH). As shown in **Figure 5.9 (a)-(b)**, FeVO(OH) synthesizes with a hydrothermal reaction temperature of 150° C show best electrocatalytic properties for both HER and OER, followed by reaction temperature of 140° C, 180° C and 130° C respectively. The influence of hydrothermal reaction time has also been studies as shown in **Figure 5.9 (c)-(d),** and a reaction time of 4 h gives the best OER and HER activity.

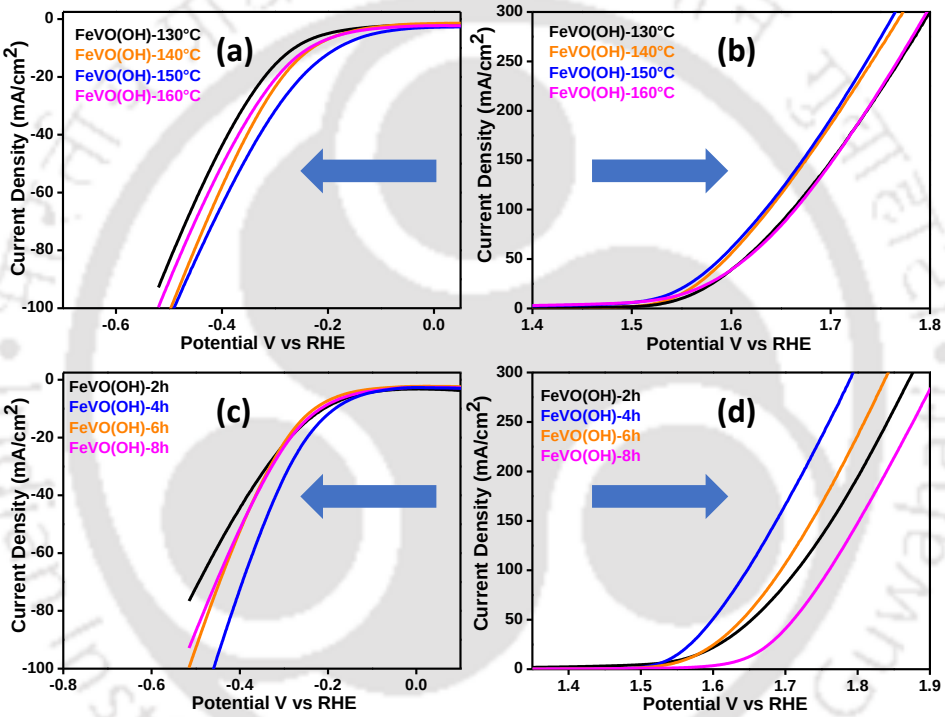

Figure 5.9 (a)-(b) Temperature optimization and (c)-(d) time optimization LSV curves of FeVO(OH) for HER and OER respectively in 1M KOH.

The doping concentration of Mo^{6+} and W^{6+} plays a crucial role in the electrocatalytic activity for overall water splitting. To evaluate the effect of the molar concentration of Ni, Mo and W, we have studied the HER and OER activity with different molar concentrations as shown in **Figure 5.10 (a)-(b)**. The highest catalytic activity is shown by molar concentration of $Ni_{0.86}Mo_{0.07}W_{0.07}(OH)_2$, too high or too low concentration is not favourable to enhance the overall water splitting.

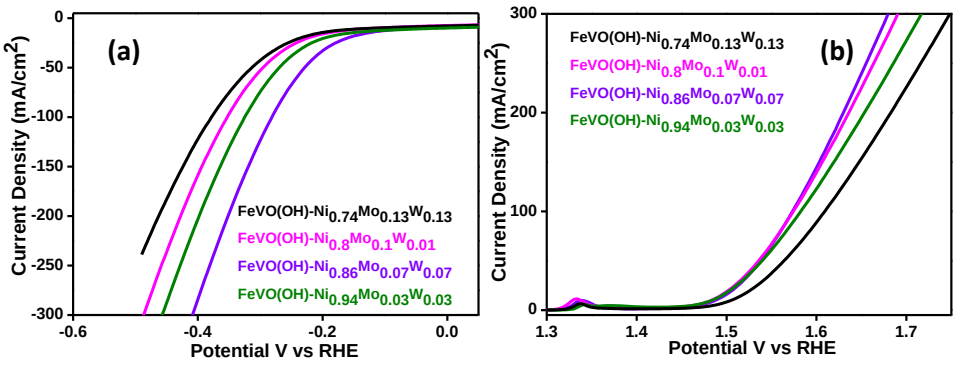

Figure 5.10 LSV curves of FeVO(OH)/NiMoW(OH)$_2$ with different concentrations of Ni, Mo and W (a) for HER and (b) OER respectively.

5.3.6 Cyclic Voltammogram (CV) Measurements

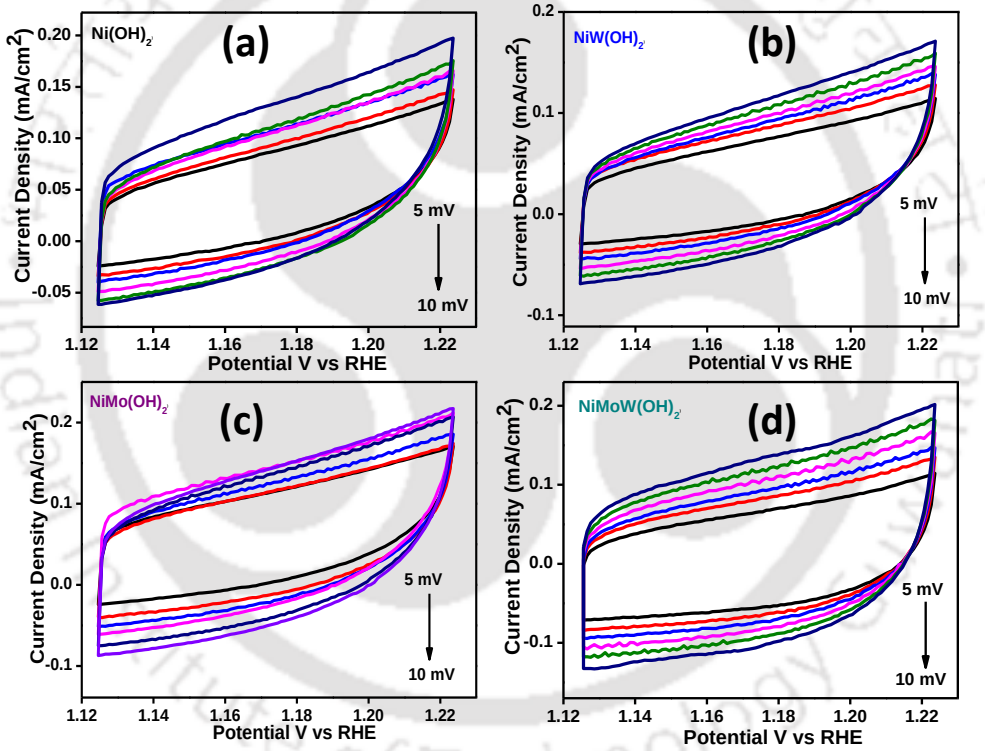

Figure 5.11 Cyclic voltammetry (CV) curves at a various scan rates of (a) Ni(OH)$_2$, (b) NiW(OH)$_2$, (c) NiMo(OH)$_2$ and (d) NiMoW(OH)$_2$ in 1M KOH.

Cyclic Voltammogram (CV) Measurements are performed at different scan rate starting from 5 mV to 10 mV within the potential window of 1.12 V to 1.22 V vs RHE in 1 M KOH electrolyte solution of Ni(OH)$_2$, NiW(OH)$_2$, NiMo(OH)$_2$ and NiMoW(OH)$_2$ as indicated in **Figure 5.11 (a-d)**. The CV curves of FeVO(OH), NiMoW(OH)$_2$

and FeVO(OH)/NiMoW(OH)$_2$ are performed in 1M KOH electrolyte solution at various scan rates from 5 mV to 10 mV within the potential range of 1.04 V to 1.14 V vs RHE as shown in **Figure 5.12 (a-c).** From CV measurement, we can deduced the double-layer capacity (C_{dl}) and Turnover Frequency (TOF) values from it.

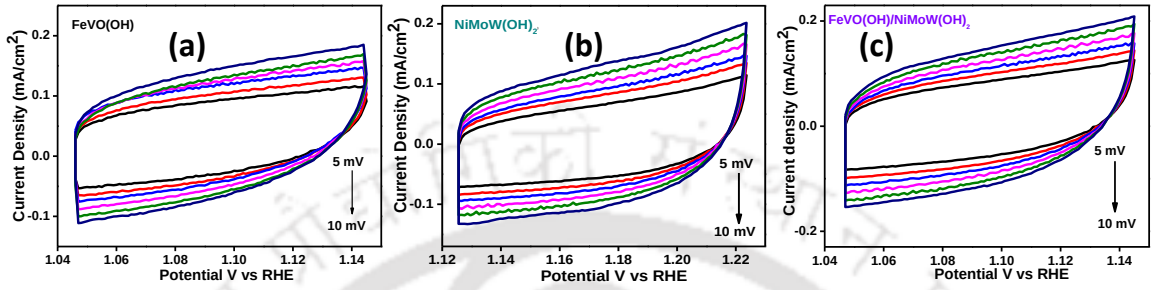

Figure 5.12 Cyclic voltammetry (CV) curves at a various scan rates of (a) FeVO(OH), (b) NiMoW(OH)$_2$ and (c) FeVO(OH)/NiMoW(OH)$_2$ in 1M KOH electrolyte solution.

5.3.7 Oxygen Evolution Reactions (OER)

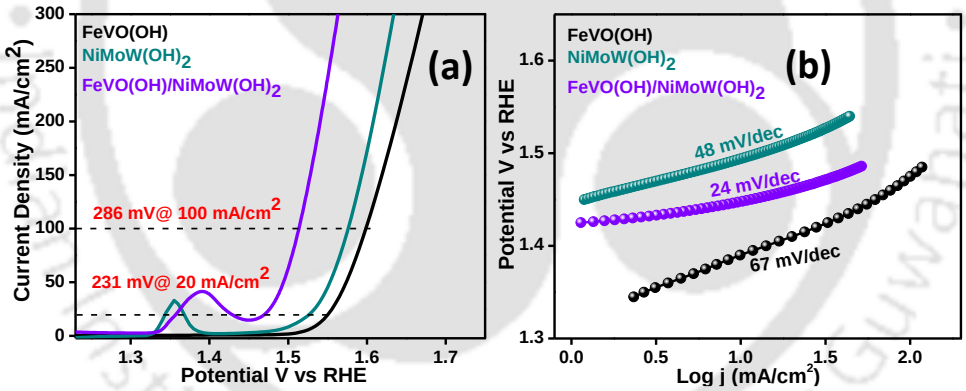

Figure 5.13 (a) LSV polarization curves of OER and (b) Corresponding Tafel slope of FeVO(OH), NiMoW(OH)$_2$, and FeVO(OH)/NiMoW(OH)$_2$ at a scan rate of 5 mV/sec in 1 M KOH.

All the electrochemical measurements are performed in 1 M KOH saturated with nitrogen by purging it before the measurements. To avoid the interference of the nickel oxidation and reduction currents in the OER and HER, the corresponding Tafel slopes are extracted from the reverse LSV scans. A systematic synthetic protocol is executed to achieve

the best possible composition in-terms of reaction times and temperatures in hydrothermal conditions.

The hybrid catalyst in **Figure 5.13 (a)**, FeVO(OH)/NiMoW(OH)$_2$ requires 231 mV to reach **20** mA/cm^2 as compared to pristine FeVO(OH) (320 mV) and NiMoW(OH)$_2$ (290 mV) at the same current density for oxygen evolution reaction (OER). Analyzing the Tafel slope gives an estimate of the reaction kinetics of the prepared electrocatalyst, thereby offers the best combination of electrocatalyst composition. The lowest Tafel slope value of 24 mV/dec is obtained for the hybrid catalyst FeVO(OH)/NiMoW(OH)$_2$ as compared to pristine FeVO(OH) (67 mV/dec) and NiMoW(OH)$_2$ (48 mV/dec), signifying better intrinsic reaction kinetics as shown in **Figure 5.13 (b)**. This experimental result validates that the co-doping of high valent Mo^{6+} and W^{6+} improves the reaction rate and kinetics for water oxidation reactions.[25]

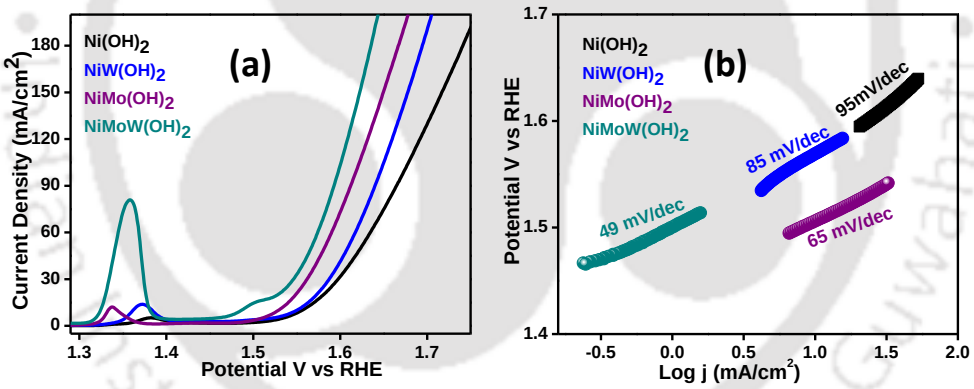

Figure 5.14 (a) Polarization curves and (b) Corresponding Tafel plots of Ni(OH)$_2$, NiW(OH)$_2$, NiMo(OH)$_2$ and NiMoW(OH)$_2$ respectively.

In **Figure 5.14 (a)**, the high oxidation peak observe between 1.3-1.4 V vs RHE in the LSV curve is due to the transition of Ni from a lower to a higher oxidation state (Ni^{2+}/Ni^{3+}). The overpotential to reach 20 mA/cm^2 current density for OER performance is 300 mV for high valent Mo^{6+} and W^{6+} co-doped NiMoW(OH)$_2$, which is lower as compared to single doping of NiMo(OH)$_2$ (330 mV), NiW(OH)$_2$ (357 mV), and pristine Ni(OH)$_2$ (365 mV). The reduction in Tafel slope value of 49 mV/dec of NiMoW(OH)$_2$ as compared to 65 mV/dec of NiMo(OH)$_2$,

85 mV/dec of NiW(OH)$_2$, and 95 mV/dec of Ni(OH)$_2$ **(Figure 5.14 (b))** at same current density confirm the synergistic effect of high valent Mo and W co-doped on the catalytic activity and kinetics for water splitting.[32] The relatively higher anodic oxidation peak of Ni for Mo and W co-doped Ni(OH)$_2$ suggests the electron-withdrawing effect of Mo and W, with increases in generation of NiOOH active species, which causes an increases in OER activity.[19, 20]

5.3.8 Hydrogen Evolution Reactions (HER)

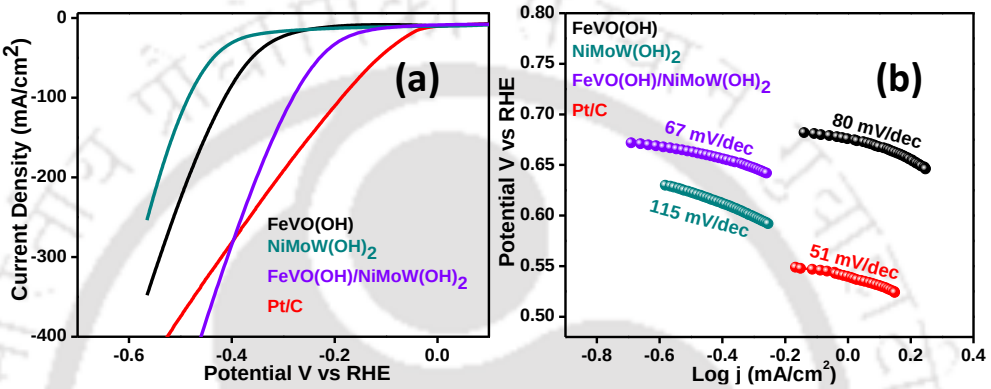

Figure 5.15 (a) LSV polarization curves of OER and (b) Corresponding Tafel slope of FeVO(OH), NiMoW(OH)$_2$, and FeVO(OH)/NiMoW(OH)$_2$ at a scan rate of 5 mV/sec in 1 M KOH.

The HER performance of all samples is measured at a sweep rate of 5 mV/sec in 1M KOH solution. The hybrid catalyst FeVO(OH)/NiMoW(OH)$_2$ as indicated in **Figure 5.15 (a)** required an overpotential of 156 mV to drive at 20 mA current density, outperforming the pristine FeVO(OH) (286 mV) and NiMoW(OH)$_2$ (342 mV). The benchmark Pt/C drop-casted on carbon paper substrate gives the best HER performance, which requires only 49 mV to drive 20 mA/cm^2 with a corresponding low Tafel slope value of 51 mV/dec. The corresponding Tafel slope as shown in **Figure 5.15 (b)** derived from the reverse LSV scan indicates better electron transport for hybrid catalyst FeVO(OH)/NiMoW(OH)$_2$, with corresponding small Tafel slope values of 67 mV/dec as compared to pristine FeVO(OH) (80 mV/dec) and NiMoW(OH)$_2$ (115 mV/dec).

5.3.9 Bar Diagrams Showing Oxygen Evolution Reactions (OER) and Hydrogen Evolution Reactions (HER)

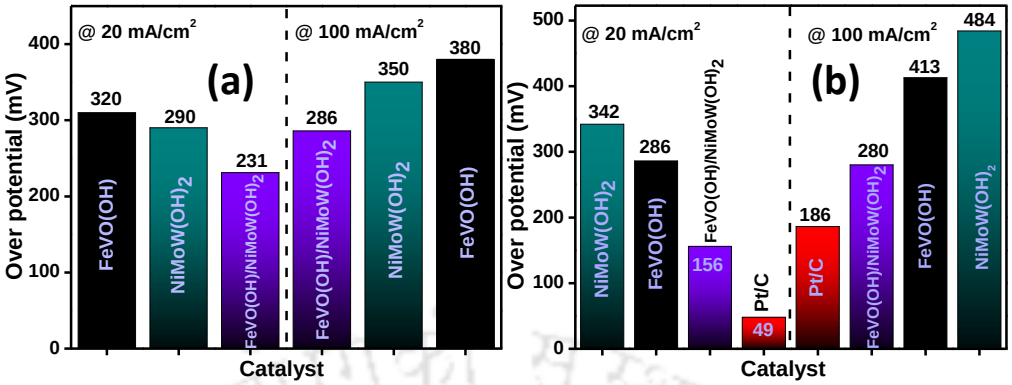

Figure 5.16 Bar diagrams showing catalytic activities at 20 mA/cm^2 and 100 mA/cm^2 for (a) OER and (b) HER of all prepared catalyst.

The catalysts are also probed at high current density as shown in **Figure 5.16 (a)-(b)** for OER and HER. FeVO(OH)/NiMoW(OH)$_2$ required a low overpotential of 286 mV for OER at 100 mA/cm^2 as compared to its bare counterpart FeVO(OH) (380 mV) and NiMoW(OH)$_2$ (350 mV) at the same current density. For HER, as shown in **Figure 5.16 (b)**, at high current density, FeVO(OH)/NiMoW(OH)$_2$ exhibits the lowest overpotential of 280 mV @ 100 mA/cm^2 as compared to pristine FeVO(OH) (413 mV) and NiMoW(OH)$_2$ (484 mV), which could be attributed to synergistic effect and increase in catalytically active surface area.[18]

5.3.10 Electrochemically Active Surface Area (ECSA) and Turnover frequency (TOF)

To further understand the intrinsic catalytic activities of the prepared catalyst, electrochemically active surface area (ECSA) is estimated as shown in **Figure 5.17 (a)**. Cyclic voltammetry (CV) measurements are performed at 5 mV/sec to 10 mV/sec scan rates as shown in **Figure 5.12 (a-c)** to obtain the estimate of double-layer capacitance (C_{dl}), and the calculated (C_{dl}) values are 10.8 mF/cm^2, 7.5 mF/cm^2 and 5.9 mF/cm^2 of FeVO(OH)/NiMoW(OH)$_2$, NiMoW(OH)$_2$ and FeVO(OH) respectively. The highest C_{dl} values for FeVO(OH)/NiMoW(OH)$_2$, signify the abundance of active sites and a better exposure of

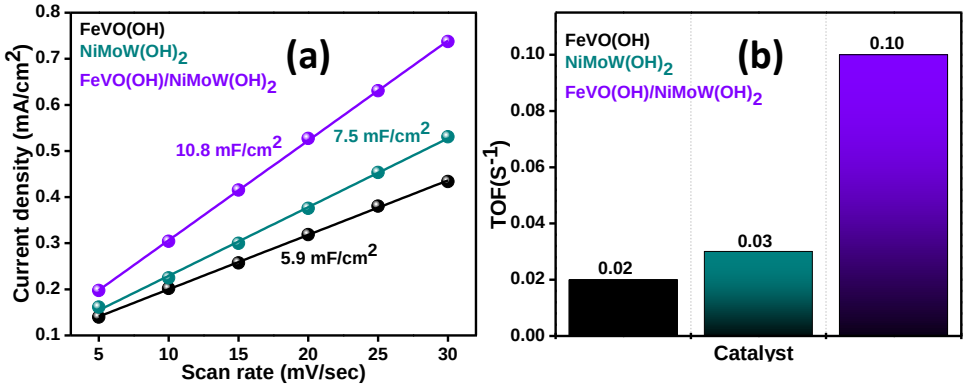

Figure 5.17 (a) $\Delta J(J_a - J_c)$ values plotted against the scanning rates and (d) Turnover frequency of FeVO(OH), NiMoW(OH)$_2$, and FeVO(OH)/NiMoW(OH)$_2$ in 1 M KOH.

surface-active sites for overall water splitting.[32, 33] Turnover Frequency (TOF) gives information about the intrinsic catalytic activity of active sites. The calculated TOF values of FeVO(OH)/NiMoW(OH)$_2$ give 0.10/s, which is 3 and 5 fold higher as compared to NiMoW(OH)$_2$ (0.03/s) and FeVO(OH) (0.02/s) respectively, implying better electrocatalytic activity **(Figure 5.17 (b))**.

5.3.11 Electrochemically Active Surface Area (ECSA) and Electrochemical Impedance Spectroscopy (EIS) Measurements

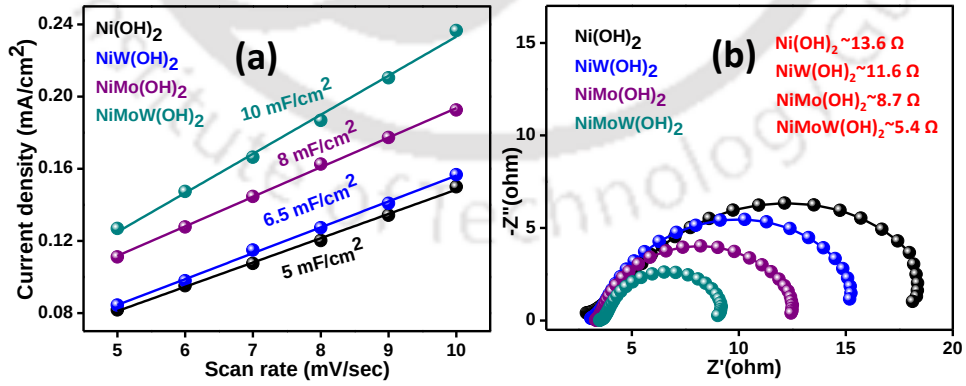

Figure 5.18 ((b) C_{dl} measurements and (a) Nyquist plots of Ni(OH)$_2$, NiW(OH)$_2$, NiMo(OH)$_2$ and NiMoW(OH)$_2$ respectively.

Highest C_{dl} values of NiMoW(OH)$_2$ is 10 mF/cm^2, which is 1.2, 1.5 and 2 folds of NiMo(OH)$_2$ (8 mF/cm^2), NiW(OH)$_2$ (6.5 mF/cm^2) and Ni(OH)$_2$ (5 mF/cm^2) respectively **(Figure 5.18 (a))**. The presence of Mo and W can enhance the catalytic activity and generates better exposure of surface-active sites.[32] Electrochemical impedance spectroscopy (EIS) measurements are also performed to assess the charge transfer kinetics **(Figure 5.18 (b))**. In the high-frequency region smallest semi-circle is obtained for NiMoW(OH)$_2$ (R_{ct} ~ 5.4 Ω) as compared to NiMo(OH)$_2$ (R_{ct} ~8.7 Ω) and NiW(OH)$_2$ (R_{ct} ~11.6 Ω), signifying a rapid charge transfer kinetics, which could be due to the effect of the unsymmetrical distribution of electrons with heteroatom doping.[17] The enhancement in the catalytic activity of NiMoW(OH)$_2$ could be attributed to the electronic modulation effect of Mo^{6+} and W^{6+} into Ni sites to facilitate the water dissociation.[33]

5.3.12 Electrochemical Impedance Spectroscopy (EIS) Measurements

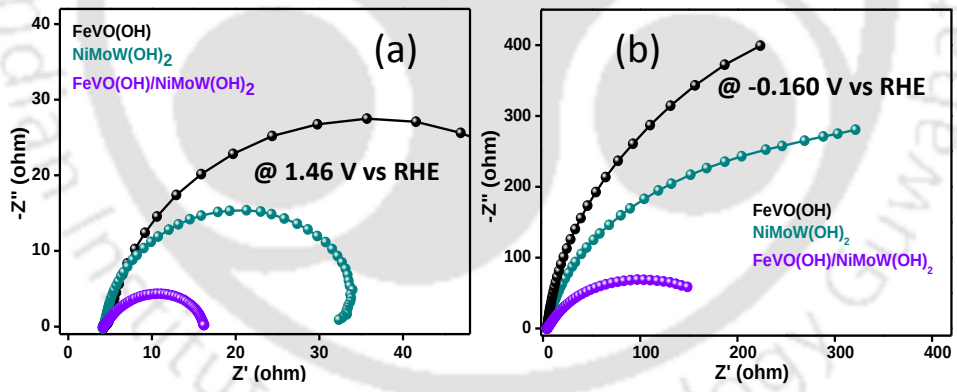

Figure 5.19 Nyquist plots of FeVO(OH), NiMoW(OH)$_2$, and FeVO(OH)/NiMoW(OH)$_2$ measured at (a) 1.46 V vs RHE, (b) -0.16 V vs RHE.

In addition, electrochemical impedance spectroscopy (EIS) is performed to study the charge transfer kinetics of synthesized catalysts in the frequency range of 0.1 Hz to 10^5 Hz with an amplitude of 10 mV. **Figure 5.19 (a)** shows the Nyquist plots of all samples. The experimental data are fitted to an equivalent Randle circuit model and the parameters are shown

in **Table 5.1**. The Nyquist plots demonstrate the smallest semicircle diameter for the composite (FeVO(OH)/NiMoW(OH)$_2$), with minimal charge transfer resistance (R_{ct}) values of 1.4 Ω, as compared to pristine FeVO(OH) (23.3 Ω) and NiMoW(OH)$_2$ (5.4 Ω). The hybrid catalyst with co-doping of Mo^{6+} and W^{6+} shows a better charge transfer kinetics, indicating accelerated Faradaic response, improved electrical conductivity and rapid charge transport to facilitate the OER kinetics.[32] The Nyquist analysis is also performed @ –0.16 V for HER to better understand the charge transfer kinetics of the reaction as shown in **Figure 5.19 (b)**. The Nyquist plot show lowest R_{ct} values of 364.5 Ω for FeVO(OH)/NiMoW(OH)$_2$ which display faster electron transport kinetics as compared to its bare conterpart.[22] The fitted parameters deduced from the Nyquist plots of FeVO(OH), NiMoW(OH)2 and FeVO(OH)/NiMoW(OH)2 are tabulated in **Table 5.1**.

Table 5.1 Tabulation of parameters obtained from the Nyquist plots fitted to an equivalent circuit model of FeO(OH), CoCeV-LTH and FeO(OH)-CoCeV-LTH.

Catalyst	R_s (Ω)	R_{ct} (Ω)	Potential (V)	R_S (Ω)	R_{ct} (Ω)	Potential (V)
FeVO(OH)	4.0	**23.3**	1.46 V vs RHE	4.13	**544.3**	-0.16 V vs RHE
NiMoW(OH)$_2$	3.6	**5.4**	1.46 V vs RHE	4.10	**426.4**	-0.16 V vs RHE
FeVO(OH)/ NiMoW(OH)$_2$	3.3	**1.4**	1.46 V vs RHE	3.72	**364.5**	-0.16 V vs RHE

5.3.13 Overall Water Splitting Measurements

For examining the overall water splitting properties as shown in **Figure 5.20 (a)**, the hybrid catalyst FeVO(OH)/NiMoW(OH)$_2$ is employed as both the anode and cathode in 1 M KOH, which exhibits a cell voltage of 1.48 V vs RHE @ 20 mA/cm^2, and the inset in **Figure 5.20 (a)** shows the digital image of the prepared electrocatalyst. The dark grey color is the bare

carbon paper (CP) substrate and the brown color represent the *insitu* grown catalyst over the CP substrate.

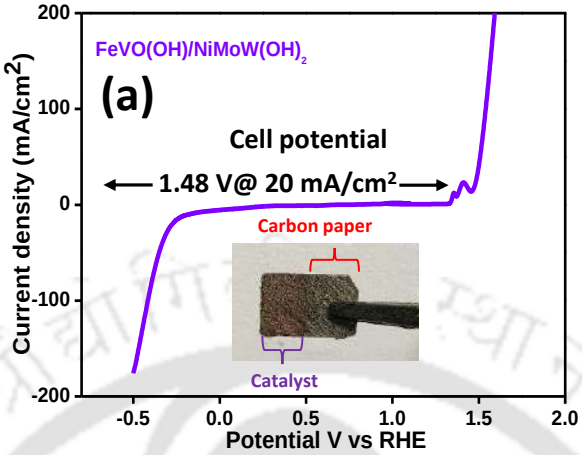

Figure 5.20 (a) Overall water splitting LSV curve of FeVO(OH)/NiMoW(OH)$_2$ at 1.48 V vs RHE with an inset showing the digital image of the prepared electrocatalyst.

5.3.14 Mechanistic Study

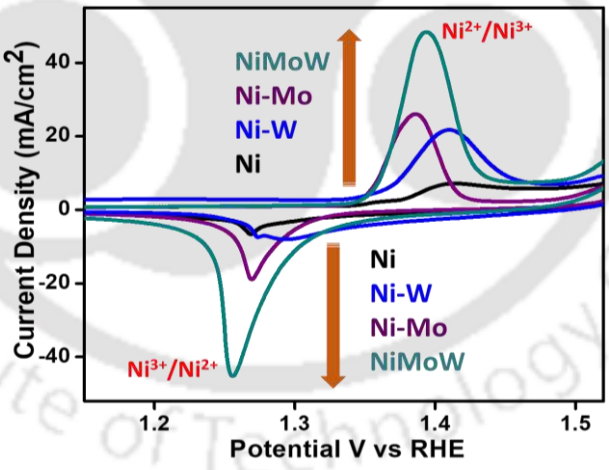

Figure 5.21 Cyclic voltammetry curves of Ni(OH)$_2$, NiW(OH)$_2$, NiMo(OH)$_2$ and NiMoW(OH)$_2$.

In **Figure 5.21**, cyclic voltammetry (CV) measurements show the change in the redox potential of Ni in Ni(OH)$_2$ with the doping of Mo^{6+} and W^{6+}. As shown in **Figure 5.21**, the redox peaks shifts from 1.42 V of Ni(OH)$_2$ to 1.38 V, 1.41 eV and 1.39 eV vs RHE of NiMo(OH)$_2$, NiW(OH)$_2$ and NiMoW(OH)$_2$ respectively.[18, 19, 21] The negative shift in potential

with individual and co-doping of Mo^{6+} and W^{6+} in comparison to bare $Ni(OH)_2$ indicates the favourable oxidation of Ni^{2+} to Ni^{3+} in forming NiOOH intermediate.[34, 35, 36]

Figure 5.22 (a) shows the CV curves of FeVO(OH) and FeVO(OH)/NiMoW(OH)$_2$ measured at 10 mV/sec in a potential window of -0.35 to 1.0 V vs RHE in 1M KOH electrolyte solution. The CV curves show two oxidation peaks at 0.25 V (Fe^{2+}/Fe^{3+}) and 0.85 V (V^{4+}/V^{5+}) and the corresponding reduction peaks at -0.06 V (Fe^{3+}/Fe^{2+}) and 0.67 V (V^{5+}/V^{4+}) of FeVO(OH). In the composite FeVO(OH)/NiMoW(OH)$_2$, the redox peaks shift to higher

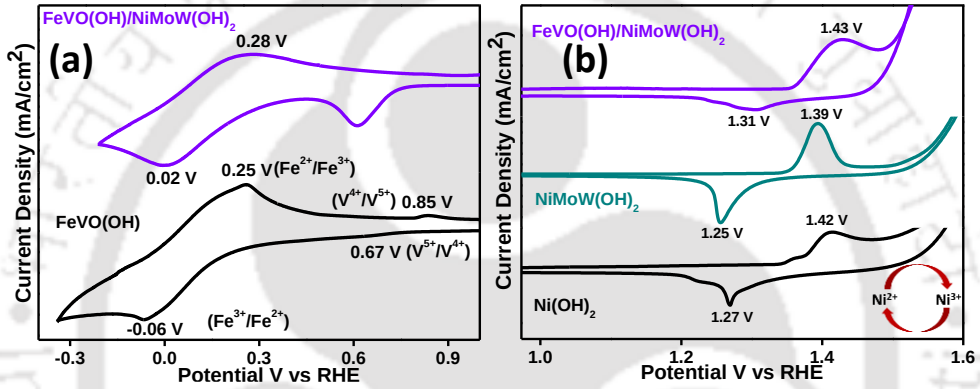

Figure 5.22 Cyclic voltammetry (CV) curves of (a) FeVO(OH) and FeVO(OH)/NiMoW(OH)$_2$ and (b) NiMoW(OH)$_2$ and FeVO(OH)/NiMoW(OH)$_2$ at a scan rate of 10 mV/sec in 1M KOH.

potential, which suggests a facile oxidation of Ni^{2+}/Ni^{3+} and the reduction of Ni^{3+}/Ni^{2+} during the CV measurements.[22, 34] The role of Mo^{6+} and W^{6+} co-doping in $Ni(OH)_2$ is studied by cyclic voltammetry (CV) measurements as shown in **Figure 5.22 (b)**. For pristine $Ni(OH)_2$, the oxidation and reduction peak is at 1.42 V (Ni^{2+}/Ni^{3+}) and 1.27 V (Ni^{2+}/Ni^{3+}) respectively, while for Mo^{6+} and W^{6+} co-doped $Ni(OH)_2$, the oxidation peak is at 1.39 V (Ni^{2+}/Ni^{3+}) and the reduction peak at 1.25 V (Ni^{3+}/Ni^{2+}). In **Figure 5.22 (b)**, comparing the redox peaks of $Ni(OH)_2$ with NiMoW(OH)$_2$ the redox peaks shift from 1.27 V to 1.25 V vs RHE, which displays the successful influence of Mo and W in $Ni(OH)_2$. The negative shift in potential with Mo and W doping in comparison to bare $Ni(OH)_2$ indicates the favourable oxidation of Ni^{2+} to Ni^{3+} to form NiOOH.[34, 35] The redox peak separation between oxidation and reduction potential of co-

doping of Mo^{6+} and W^{6+} in $Ni(OH)_2$ is smaller than pristine $Ni(OH)_2$, indicative of negative shift in potential with doping.[37] In the hybrid catalyst FeVO(OH)/NiMoW(OH)$_2$, the oxidation peaks show a positive shift with co-doping of high valence state of Mo^{6+} and W^{6+}.

The schematic illustration of the proposed reaction mechanism is shown in **Figure 5.23 (a)-(b)**. In **step (1)**, in alkaline medium, OH^- will get adsorbed onto the $Ni(OH)_2$ and gets oxidized to $Ni^{3+}$of NiOOH with the generation of an ē. Meanwhile, in **step (2)**, $Ni^{3+}$of NiOOH accepts ē and itself gets reduced to $Ni^{2+}$of $Ni(OH)_2$ with the release of OH^- ions **Figure 5.23 (a)**. The presence of Mo^{6+} and W^{6+} in its higher oxidation state as shown in **steps (3)** and **(4)**, favours the simultaneous accelerated oxidation of Ni^{2+}/Ni^{3+} and the reduction of Ni^{3+}/Ni^{2+} to accelerate the overall water splitting as shown in **Figure 5.23 (b)**.[20] The redox cyclic process involve in **Figure 5.23 (a)** is given below;

$$Ni\ (II)(OH)_2 + OH^- \longleftrightarrow Ni(III)OOH + H_2O + \bar{e} \qquad \textbf{(5.1)}$$

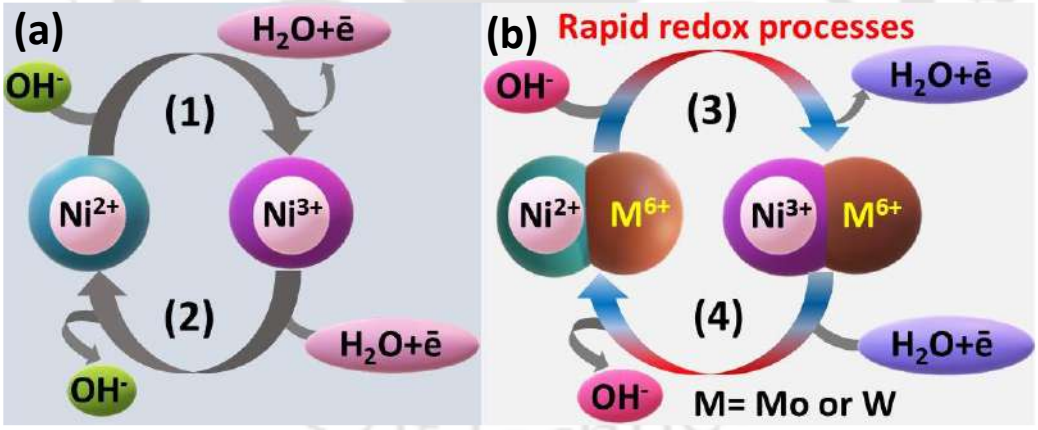

Figure 5.23 Schematic illustration of the proposed reaction mechanism of (a) $Ni(OH)_2$ and (b) co-doping of Mo^{6+} and W^{6+} in $Ni(OH)_2$.

The effect of co-doping of Mo^{6+} and W^{6+} in $Ni(OH)_2$ in enhancing the redox process is given in **equation (5.2)** which represent the reaction involved in steps (3) and (4) of **Figure 5.23 (b)**.

$$M(VI)\,OH + Ni\,(II)(OH)_2 + OH^- \longleftrightarrow M(VI)OH + Ni\,(III)OOH + H_2O + \bar{e}$$

(5.2) (M= Mo^{6+}/W^{6+})

5.3.15 Long term operational stability

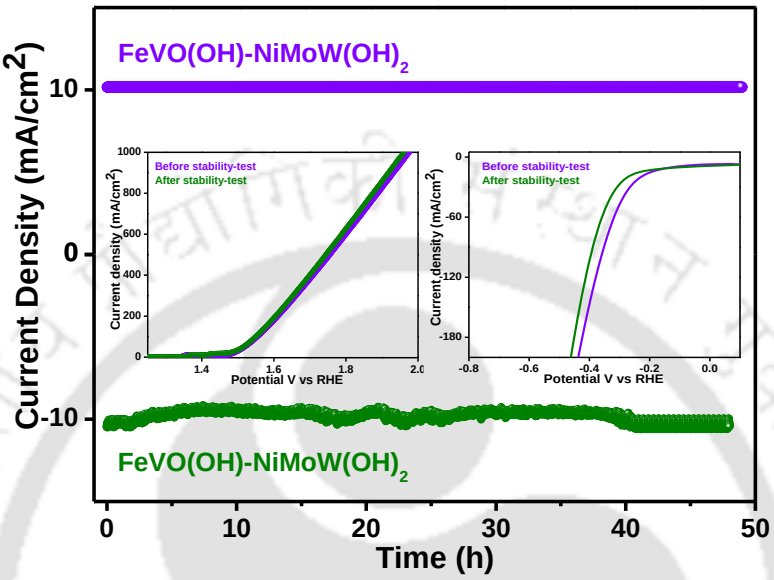

Figure 5.24 Chronoamperometry (*i-t*) curves of FeVO(OH)/NiMoW(OH)$_2$, with an inset showing the LSV curve before and after stability-test for HER and OER of FeVO(OH)/NiMoW(OH)$_2$ in 1M KOH.

Long-term operational stability is an important parameter for practical water splitting. **Figures 5.24** shows the chronoamperometry (*i-t*) curves of FeVO(OH)/NiMoW(OH)$_2$ for HER and OER for 48 h, with an inset showing the polarization curves before and after the stability test. The LSV curve of HER in **Figure 5.24** shows a negligible change in current density after subjecting to a continuous 48 h. In **Figure 5.24**, FeVO(OH)/NiMoW(OH)$_2$ for OER shows negligible attenuation after the durability test, which indicates the stability of the system. To better understand the durability of the system, FESEM, HRTEM, XRD, and EIS are performed pre and post-electrochemical measurements. The hybrid catalyst FeVO(OH)/NiMoW(OH)$_2$ shows retention in morphology and interplanar spacing post electrochemical measurements **(Figure 5.25 (a)-(b))**. The experimental result in **Figure 5.25 (c)** indicates an increase in charge transfer kinetics during the electrochemical measurements, and XRD **(Figure 5.25 (d))** shows

no change in crystalline structure which further substantiates the stability of the prepared catalyst.

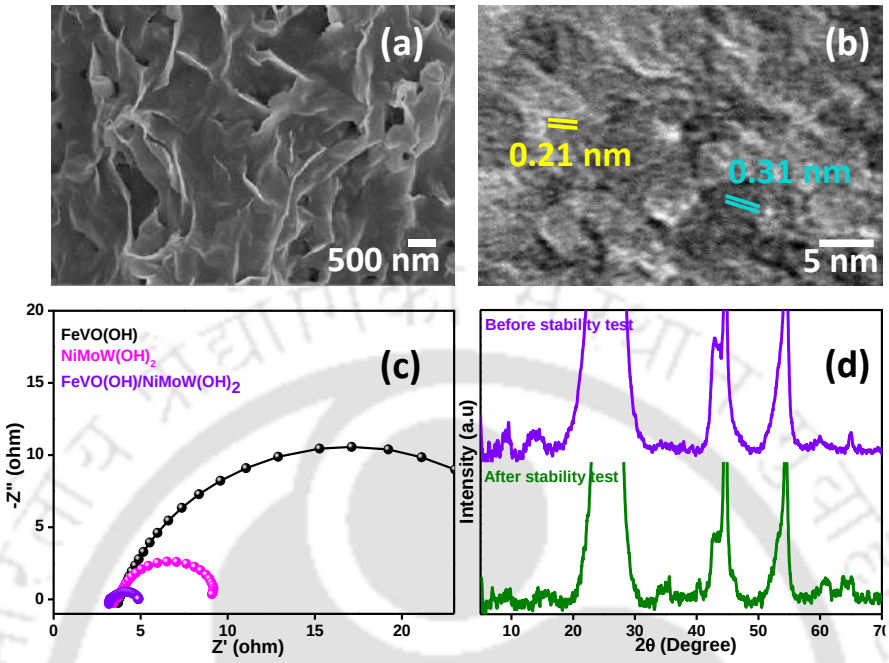

Figure 5.25 (a) Field Emission Scanning Electron Microscopy (FESEM) images and (b) High-Resolution Transmission Electron Microscopy (HRTEM) image of FeVO(OH)/NiMoW(OH)$_2$ after stability-test, (c) Nyquist plots of FeVO(OH), NiMoW(OH)$_2$, FeVO(OH)/NiMoW(OH)$_2$ after stability-test and XRD of FeVO(OH)/NiMoW(OH)$_2$ before and after stability-test.

5.4 CONCLUSION

In summary, we have designed a binder-free hybrid catalyst FeVO(OH)/NiMoW(OH)$_2$ for HER and OER via a two-step hydrothermal process. The as-synthesized electrocatalyst exhibits a low overpotential of 231 mV for OER and 156 mV for HER at a current density of 20 mA/cm^2 with a small Tafel slope value of 24 mV/dec for OER and 67 mV/dec for HER respectively in an alkaline medium. The FeVO(OH) nanoparticles and NiMoW(OH)$_2$ nanosheets enhance electrolyte diffusion and accelerate the water splitting kinetics. The hybrid catalyst FeVO(OH)/NiMoW(OH)$_2$ can be employed as a promising electrocatalyst to replace noble metal catalysts for a long-term and practical overall water splitting device.

5.5 REFERENCES

1. Y. Wang, D. Yan, S. El Hankari, Y. Zou, S. Wang, *Adv. Sci.*, 2018, **5**, 1800064.
2. J. Hou, Y. Wu, B. Zhang, S. Cao, Z. Li, L. Sun, *Adv. Funct. Mater.*, 2019, **29**, 1808367.
3. X. Du, J. Huang, J. Zhang, Y. Yan, C. Wu, Y. Hu, C. Yan, T. Lei, W. Chen, C. Fan, J. Xiong, *Angew. Chem., Int. Ed.*, 2019, **58**, 4484.
4. C.-Z. Yuan, K. S. Hui, H. Yin, S. Zhu, J. Zhang, X.-L. Wu, X. Hong, W. Zhou, X. Fan, F. Bin, F. Chen, K. N. Hui, *ACS Mater. Lett.*, 2021, **3**, 752– 780.
5. J. Wang, T. Liao, Z. Wei, J. Sun, J. Guo, Z. Sun, *Small Methods*, 2021, **5**, 2000988.
6. J. Yan, L. Kong, Y. Ji, J. White, Y. Li, J. Zhang, P. An, S. Liu, S. T. Lee, T. Ma, *Nat. Commun.*, 2019, **10**, 2149.
7. M. I. Jamesh, X. Sun, *ChemCatChem*, 2019, **11**, 1550– 1575.
8. Y. Hu, J. Zhou, L. Li, Z. Hu, T. Yuan, C. Jing, R. Liu, S. Xi, H. Jiang, J-Q. Wang and L. Zhang, *J. Mater. Chem. A*, 2022, **10**, 602-610.
9. C.T. Moi, S. Bhowmick, T.K. Sahu, M. Qureshi, *Electrochim. Acta*., 2021, **370**, 137726.
10. X. Cao, Y. Sang, L. Wang, G. Ding, R. Yu and B. Geng, *Nanoscale*, 2020, **12**, 19404 —19412.
11. X. Ji, C. Cheng, Z. Zang, L. Li, X. Li, Y. Cheng, X. Yang, X. Yu, Z. Lu, X. Zhang and H. Liu, *J. Mater. Chem. A*, 2021, **9**, 12074 —12079.
12. X. Ji, C.-Q. Cheng, Z. Zang, L. Li, X. Li, Y. Cheng, X. Yang, X. Yu, Z. Lu, X. Zhang and H. Liu, *J. Mater. Chem. A*, 2020, **8**, 21199 —21207.

13. J. Guan, C. Li, J. Zhao, Y. Yang, W. Zhou, Y. Wang, G. R. Li, *Appl. Catal., B*, 2020, **269**, 118600.

14. Q. H. Cao, M. Luo, Y. T. Huang, Q. Liu, X. X. Kong, J. L. Lei, Z. Jiang, J. H. Wang, *Sustainable Energy Fuels*, 2020, **4**, 1522.

15. J. Luo, X-H. Wang, L. Shen, H-C. Fu, X-H. Chen, L-L. Wu, Q. Zhang, H-Q. Luo, N-B. Li, *ACS Sustainable Chem. Eng.*, 2021, **9**, 12233–12241.

16. X. Qiao, H. Kang, Y. Li, K. Cui, X. Jia, H. Liu, W. Qin, M. Pupucevski, G. Wu, *ACS Appl. Mater. Interfaces*, 2020, **12**, 36208.

17. Y. Song, J. Cheng, J. Liu, Q. Ye, X. Gao, J. Lu and Y. Cheng, *Appl. Catal., B*, 2021, **298**, 120488.

18. S. S. Lu, L. M. Zhang, Y. W. Dong, J. Q. Zhang, X. T. Yan, D. F. Sun, X. Shang, J. Q. Chi, Y. M. Chai, B. Dong, *J. Mater. Chem. A*, 2019, **7**, 16859.

19. Q. Wang, H. Zhao, F. Li, W. She, X. Wang, L. Xu, H. Jiao, *J. Mater. Chem. A*, 2019, **7**, 7636.

20. D. Rathore, A. Banerjee, S. Pande, *ACS Appl. Nano Mater.*, 2022, **5**, 2664–2677.

21. Y. S. Jin, S. L. Huang, X. Yue, H. Y. Du, P. K. Shen, *ACS Catal.*, 2018, **8**, 2359.

22. C.T. Moi, S. Bhowmick, T.K. Sahu, M. Qureshi, *Electrochim. Acta*. *ACS Appl. Mater. Interfaces*, 2021, **13**, 51151–51160.

23. K. Fan, Y. Ji, H. Zou, J. Zhang, B. Zhu, H. Chen, Q. Daniel, Y. Luo, J. Yu and L. Sun, *Angew. Chem., Int. Ed. Engl.*, 2017, **56**, 3289 —3293.

24. H. Xu, Y. Liao, Z. F. Gao, Y. Qing, Y. Q. Wu, L. Y. Xia, *J. Mater. Chem. A*, 2021, **9**, 3418.

25. X. Luo, P. Ji, P. Wang, R. Cheng, D. Chen, C. Lin, J. Zhang, J. He, Z. Shi, N. Li, S. Xiao, S. Mu, *Adv. Energy Mater.*, 2020, **10**, 1903891.

26. J. Li, H. Sun, L. Lv, Z. Li, X. Ao, C. Xu, Y. Li and C. Wang, *ACS Appl. Mater. Interfaces*, 2019, **11**, 8106 —811.

27. J. Jiang, F. Sun, S. Zhou, W. Hu, H. Zhang, J. Dong, Z. Jiang, J. Zhao, J. Li, W. Yan, M. Wang, *Nat. Commun.*, 2018, **9**, 2885-2896.

28. X. Wang, Y. Tuo, Y. Zhou, D. Wang, S. Wang, J. Zhang, *Chem. Eng. J.*, 2021, **403**, 126297.

29. B. Singh, A. K. Patel, A. Indra, *Mater. Today*, 2022, **25**, 100930.

30. H. Sun, J. G. Li, L. Lv, Z. Li, X. Ao, C. Xu, X. Xue, G. Hong, C. Wang, *J. Power Sources*, 2019, **425**, 138– 146.

31. X. Shen, M. Zhang, M. S. Sudi, W. Zhao, Q. Wang, J. Ren, L. Zhao, A. Wang, W. Zhu, *Chem. Commun.*, 2021, **57**, 12516– 12519.

32. X. Guo, M. Li, L. He, S. Geng, F. Tian, Y. Song, W. Yang, Y. Yu, *Nanoscale*, 2021, **13**, 14179.

33. S. S. Xiong, S. T. Weng, Y. Tang, L. Qian, Y. Q. Xu, X. F. Li, H. J. Lin, Y. C. Xu, Y. Jiao and J. R. Chen, *J. Colloid Interface Sci.*, 2021, **602**, 355.

34. B. Zhang, L. Wang, Z. Cao, S. M. Kozlov, F. P. García de Arquer, C. T. Dinh, J. Li, Z. Wang, X. Zheng, L. Zhang, Y. Wen, O. Voznyy, R. Comin, P. De Luna, T. Regier, W. Bi, E. E. Alp, C. W. Pao, L. Zheng, Y. Hu, Y. Ji, Y. Li, Y. Zhang, L. Cavallo, H. Peng, E. H. Sargent, *Nat. Catal.*, 2020, **3**, 985.

35. J. M. P. Martirez, E. A. Carter, *ACS Catal.*, 2020, **10**, 2720.

36. W. Lai, L. Ge, H. Yang, Y. Deng, H. Li, B. Ouyang, L. Xu, J. Bao, *J. Mater. Chem. A*, 2021, **10**, 10525-10539.

37. Z. Zhang, H. Huo, L. Wang, S. Lou, L. Xiang, B. Xie, Q. Wang, C. Du, J. Wang, G. Yin, *Chem. Eng. J.*, 2021, **412**, 128617.

CHAPTER 6

Noble metal free hierarchical VS_2 onto WO_3 nanoflakes as heterojunction strategy for photoelectrochemical water oxidation

Chapter 6 *describe about the design of highly surface reactive and noble metal free* VS_2 *nanoflowers onto in situ grown* WO_3 *photoanode as a heterojunction strategy for efficient charge separation. The main drawback of* WO_3 *is slow surface reaction kinetics leading to an undesired carrier recombination.* VS_2*, with active sites both on the edge and basal plane, reduce the surface charge recombination and enhance the kinetics of* O_2 *evolution reaction. The current chapter study about the charge carrier density, charge transfer kinetic and durability of the prepared catalyst for PEC water oxidation.*

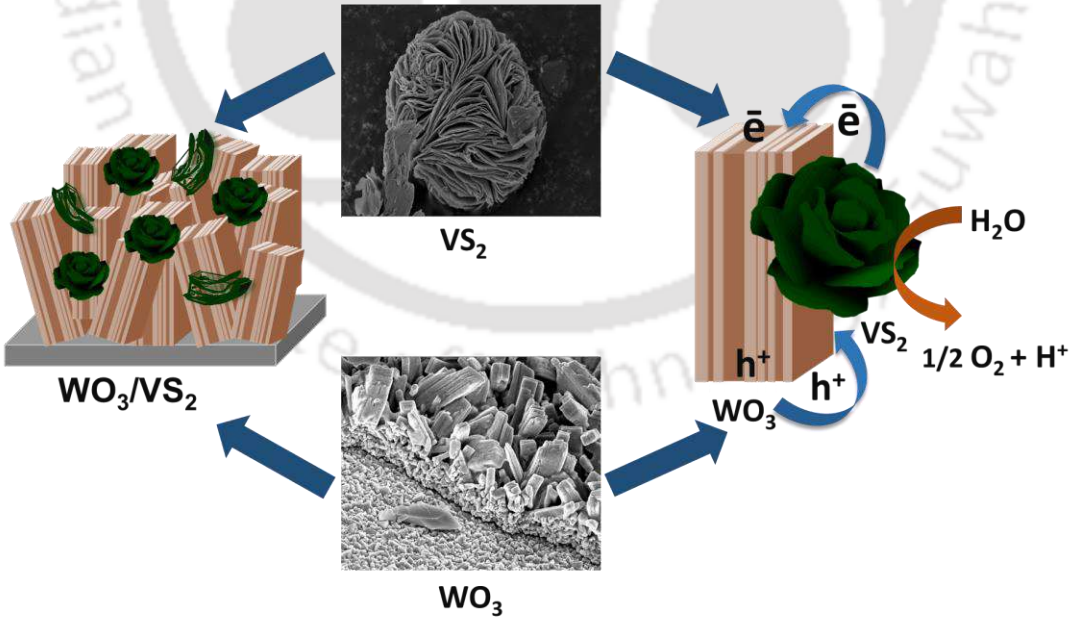

C. T. Moi et al., *Sustainable Energy Fuels*, 2019, **3**, 348

6.1 INTRODUCTION

With increase in global energy consumption and environmental crisis, the need for clean, economical and environmentally benign renewable energy resources to moderate our dependence on fossil fuel is the biggest technological challenge.[1] Accomplishing the objectives with semiconductor-based photo-electrochemical (PEC) water splitting, where solar energy is transformed directly into chemical energy to split water molecules into hydrogen and oxygen is the most promising, greener and challenging path.[2] Since the breakthrough work of water splitting on titanium electrode done by Honda and Fujishima in 1972, PEC water splitting with semiconductors became a potential route for generating clean energy.[3] For a promising PEC reaction, catalysts with good light harvesting ability, high stability, nontoxic and natural abundance are greatly desirable.[4] Wide range of metal oxides such as TiO_2,[5] Fe_2O_3,[6] $BiVO_4$,[7] ZnO[8] and WO_3[9] have been widely explored for application in PEC water splitting. WO_3 (E_g ~ 2.5–2.8 eV) can utilize about 12 % of solar spectrum.[10] WO_3 has a great potential for PEC water splitting due to its high earth-abundance, excellent electrical properties, chemical stability under acidic conditions, ease of fabrication etc. Although WO_3 possesses a moderate hole diffusion length (~ 150 nm) with a high electron mobility (~12 $cm^2 V^{-1} s^{-1}$), its rapid photogenerated electron–hole recombination at the hetero-interface i.e. semiconductor and electrolyte interface inherently hinders its photoelectrochemical (PEC) performance as compared with the theoretical conversion efficiency of 4.8 %.[11] Several strategies have been developed to address the limitation including, the introduction of oxygen vacancies or doping with heteroatoms,[12,13] morphological modification (e.g., nanowires, nanoflakes and nanoneedles)[14] and surface modification (e.g., with noble metal).[15] To overcome the shortcomings, "ideal" material should be highly efficient in light absorption, photogenerated charges separation and in accumulating and transporting those charges

carriers for constructive chemical processes.[16] Therefore, numerous efforts have attempted to achieve an efficient photocatalysis on WO_3 via fabrication with narrow band gap semiconductors to form a heterojunction including Fe_2O_3,[17] $BiVO_4$,[18] Cu_2O,[19] Bi_2S_3,[20] CdS,[21] Sb_2S_3,[22] MoS_2[23] etc. to enhance the light absorbance ability, facilitate charge separation and enhance oxygen evolution dynamics.

Layered transition metal dichalcogenides (LTMDs), such as WS_2, FeS_2, CoS_2, MoS_2, VS_2 and NiS_2 have attracted wide attention with its exclusive properties and applications to optoelectronics, energy storage, sensing etc. However, the basal plane of LTMDs are inert, limiting their photocatalytic activity.[24] VS_2 is one of the members of 2D layered TMDs, comprising of S−V−S triple layers with an interlayer spacing of 5.76 Å stacked together by weak van der Waal interactions and with hexagonal structure like MoS_2. VS_2 with its high surface area and exclusive electronic structure is an emerging electrocatalyst.[25] VS_2 is widely coupled with other semiconductors for water splitting,[24,26-28,] sensors,[29] electrochemical energy storage and conversion.[30,31] VS_2 with an active edge and basal plane possesses high electrocatalytic performance as compared to MoS_2 and WS_2.[32]

Herein, fabrication of VS_2 coupled with *in situ* grown WO_3 nanoflakes (NF's) for water oxidation is reported for the first time. Hydrothermally grown WO_3 directly on transparent conductive oxide, i.e., FTO, is coupled with VS_2 to generate abundant interfaces and create rich surface-active sites. VS_2 acts as photo-induced charge trapping and transportation media, which further leads to high charge transfer ability and effectively reduce bulk and surface charge recombination to facilitate the water oxidation. In the composite, WO_3-VS_2 exhibits 5.5-fold increments in the PEC water oxidation as compared to bare WO_3.

6.2 EXPERIMENTAL SECTION

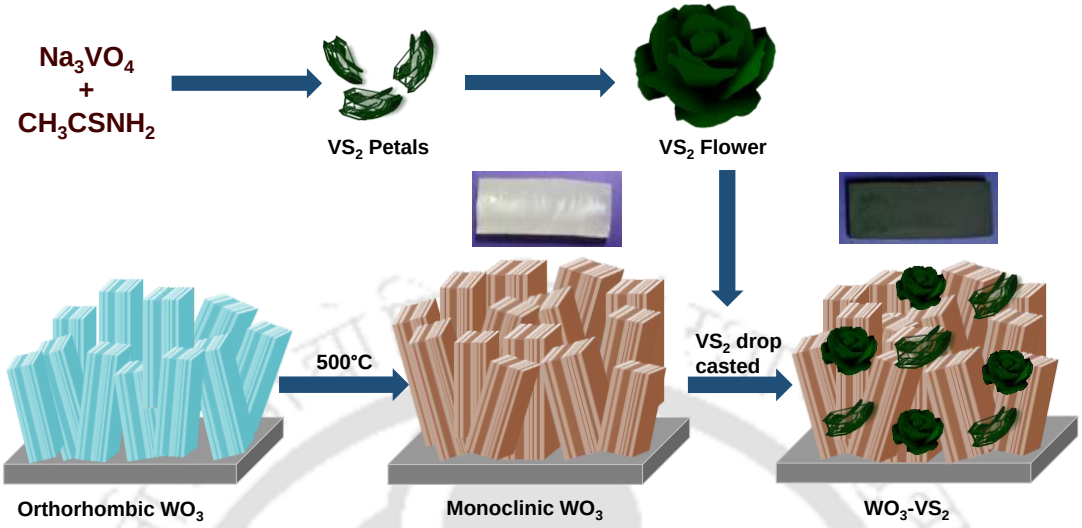

Scheme 6.1 Schematic representation of synthesis and fabrication of WO_3 and WO_3-VS_2.

Scheme 6.1 shows the schematic representation of as synthesis WO_3 and WO_3-VS_2. The *insitu* grown WO_3 nanoflakes directly onto FTO substrate is partially cover with VS_2 nanosheets.

6.2.1 Fabrication of WO_3 nanoflake arrays on FTO

WO_3 nanoflake arrays were directly grown onto FTO substrate without the aid of a seed layer following a previously reported procedure.[33] 0.05 M of sodium tungstate dihydrate was completely dissolved in deionized water by stirring. After the suspension of sodium tungstate dihydrate, concentrated hydrochloric acid (1ml) was added drop wise at room temperature (pH~2.5) and the solution was continuously stirred for an hour to give a yellow precipitate of tungstic acid. Hydrogen peroxide (1.5 ml) was added to the above solution and continue to stir vigorously for 2 h to give a stable solution of peroxopolytungstic acid (PTA).

Ozonized FTO substrates were placed subsequently at certain angle with the conducting side facing downward, inclined against the wall of a Teflon-liner. The prepared solution was then transferred to a Teflon lined autoclave to fill 70 % of its capacity and reacted hydrothermally at

160 °C for 6 hours. After the reaction, the reactor was allowed to cool down to room temperature normally. The FTO with light bluish colour product deposited on it was rinsed with deionized water and ethanol, air-dried at 60 °C overnight and annealed in a muffle furnace at 500 °C for an hour at heating rate of 5 °C /min. The as-synthesized films were pale blue in colour which was transformed to yellow-green upon calcination with an increase in crystallinity.

6.2.2 Synthesis of VS_2

In a typical synthesis, 6 mmol sodium orthovanadate ($Na_3VO_4.12H_2O$) and 32 mmol thioacetamide (CH_3CSNH_2) were dissolved in 50 ml deionized water, and the solution was vigorously stirred for an hour. Then the as-prepared homogenous solution was transferred into 75 ml Teflon-lined autoclave, tightly sealed and reacted hydrothermally at 160 °C for 24 hours. The autoclave was allowed to cool down to room temperature, the black precipitates product were rinsed using deionized water and anhydrous ethanol, further dried at 60 °C in a vacuum oven for overnight.[32]

6.2.3 Preparation of working electrodes

The *in situ* grown WO_3 directly on FTO was used as the bare WO_3 working electrode. For the composite WO_3-VS_2 working electrode, 110 µL of deionized water, 45 µL isopropanol and 15 µL Nafion solution were added to 5 mg of VS_2 and sonicated for about 30 minutes to give a homogenous slurry black ink. Then, 10 µL of the catalyst was then uniformly drop casted onto hydrothermally grown WO_3 film of 1 cm^2 and dried at 60 °C for 12 hours in a vacuum oven and used as the working electrodes for the photoelectrochemical characterizations.

6.3 RESULTS AND DISCUSSIONS

6.3.1 Powder X-Ray Diffraction (PXRD) Analysis

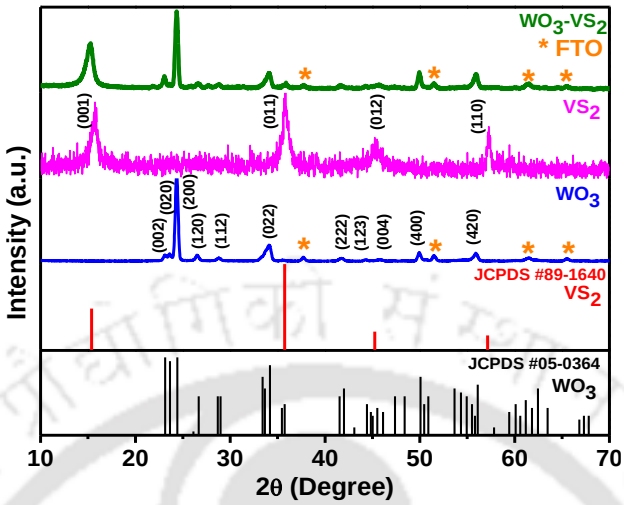

Figure 6.1 XRD diffraction patterns of WO_3, VS_2 and WO_3-VS_2 composites.

Crystal purity of the *in situ* grown WO_3 nanoflakes (NFs), VS_2 and WO_3-VS_2 composites were confirmed by X-ray diffraction (XRD) analysis and related diffractograms were present in **Figure 6.1**. Three well resolved diffraction peak at 2θ value of 23.2°, 23.6° and 24.3° corresponding to (002), (020) and (200) plane respectively, assignable to monoclinic crystal phase of WO_3 as confirmed by JCPDS card No. 05-0364. High intensity growth of (200) facet could be attributed to flake-like morphological WO_3 structure grown directly onto FTO with a distinctly ordered NFs arrays.[32] VS_2 PXRD pattern was indexable to hexagonal 1T-phase (JCPDS card No. 89-1640). Four sharp diffraction peaks were assignable to (001), (011), (012) and (110) at 2θ value of 15.4°, 35.7°, 45.2° and 57.2° respectively. In the composite, both diffraction peaks of WO_3 and VS_2 were indexable confirming the presence of both WO_3 and VS_2.

6.3.2 UV-Visible Spectra Analysis

The UV–visible absorption spectra of WO_3 and WO_3-VS_2 were illustrated in **Figure 6.2 (a)** and the Tauc plot for estimating the band gaps were shown in **Figure 6.2 (b)**. Composite made

using VS_2 was red shifted, and calculated band gaps from Tauc plots are 2.67 eV and 2.74 eV for composite WO_3-VS_2 and pristine WO_3 respectively.

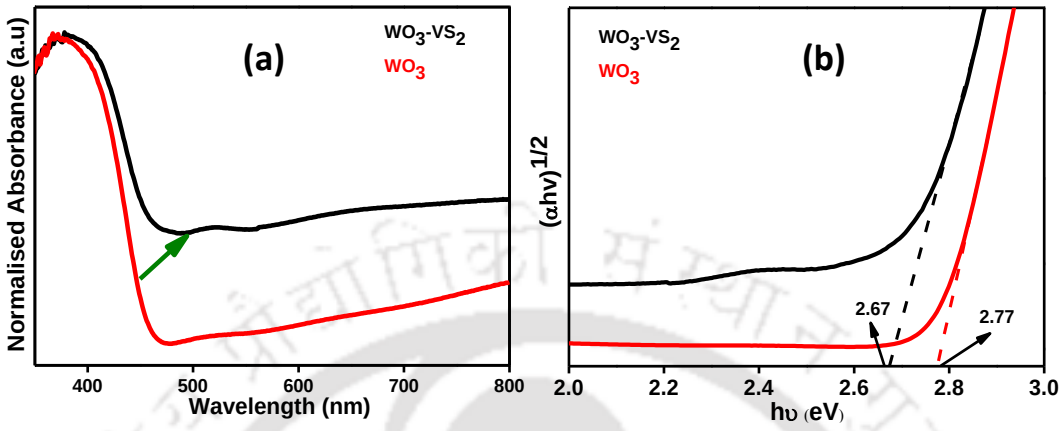

Figure 6.2 (a) UV-Vis absorption spectra and (b) Tauc plot of WO_3 and WO_3-VS_2 composites.

6.3.3 X-Ray Photoelectron Spectroscopy (XPS) Analysis

XPS was documented to probe the chemical state and elemental composition of the VS_2 and WO_3-VS_2 composite. Peaks were calibrated at 284.7 eV with respect to C 1s. **Figure 6.3 (a)** show the survey spectra of WO_3-VS_2, which indicate the presence of all components W, O, V and S in the composite sample. The O 1s core level spectra of pristine VS_2 and WO_3-VS_2 composites shows two peaks **(Figure 6.3 (b))** at binding energy value of 530.4 eV and 531.4 eV which were ascribed to M-O bonds corresponding to lattice oxygen and adsorbed O-H species respectively, a shoulder peak was observed at 532.6 eV due to water molecules.[34-35] In **Figure 6.3 (c)** V 2p core level spectra indicates the presence of V species with variable oxidation state at the surface of the synthesize materials. The V 2p signals of VS_2 located at 517.1 eV and 524.2 eV were attributed to V $2p_{3/2}$ and V $2p_{1/2}$, signifying the existence of V in +4 oxidation state. Owing to a strong attraction of vanadium towards oxygen, under atmospheric condition it rapidly gets oxidized which was confirmed by the observance of the other two peaks at 518.1 eV and 525.3 eV corresponding to V $2p_{3/2}$ and V $2p_{1/2}$ of vanadium in +5 oxidation states respectively. This indicates that V+4 was

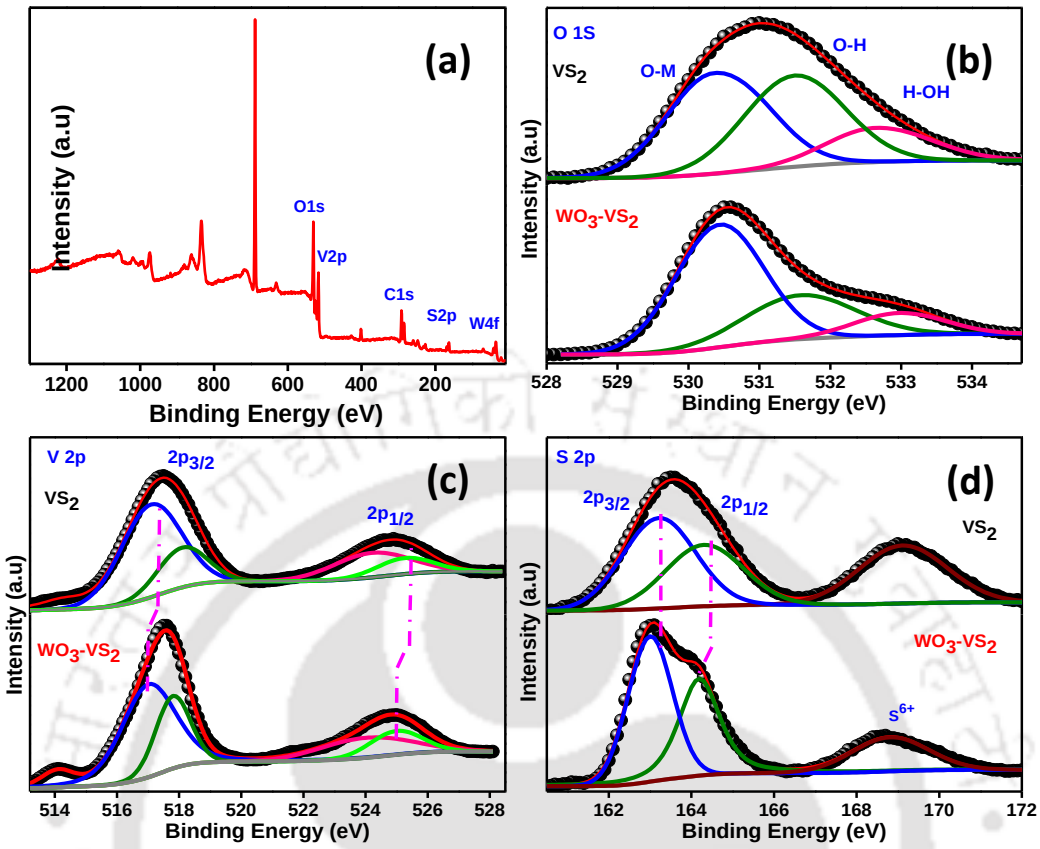

Figure 6.3 (a) XPS survey spectra of WO_3-VS_2 composites, high-resolution XPS core-level spectra of (b) O 1S (c) V 2p and (d) S 2p of VS_2 and WO_3-VS_2 composites.

partially oxidized to V+5 during the hydrothermal synthesis. Similarly, V 2p signals of WO_3-VS_2 shows two signals at 517.0 eV and 524.0 eV which were associated with V^{4+} $2p_{3/2}$ and V^{4+} $2p_{1/2}$ respectively, while the two weak peaks assigned at 517.8 eV and 525.0 eV were ascribed to V^{5+} $2p_{3/2}$ and V^{5+} $2p_{1/2}$ respectively.[24, 36-39] The peak at around 514 eV for VS_2 and WO_3-VS_2 samples in the XPS spectra of V 2p, corresponds to V2p (3/2) peak of V-O bond.[40] The S 2p **(Figure 6.3 (d))** peak fitting analysis confirms the presence of S^{2-} and O-S bond with two peaks located at binding energy value of 163.4 eV and 164.3 eV assignable to S $2p_{3/2}$ and S $2p_{1/2}$ respectively for VS_2 and 163.0 eV and 164.1 eV that can be assigned to S $2p_{3/2}$ and S $2p_{1/2}$ respectively for WO_3-VS_2 composite. The observation of the peak at around 169.1 eV and 168.8 eV for VS_2 and WO_3-

VS_2 were assignable to sulfate indicating the material surface was partially oxidized.[41-42] A slight shift to the lower binding energy of V 2p and S 2p spectra for WO_3-VS_2 were observed, an indicative that thin layer of VS_2 interacts with WO_3 NFs in the composite. In the composite the energy shift towards lower binding energy could be clarified by the existence of higher polarization of electron in the composite with VS_2, with respect to lesser electron- hole recombination, an increase in electron density in the composite was observed.[43]

6.3.4 Fourier transform infrared spectroscopy (FTIR) Spectra Analysis

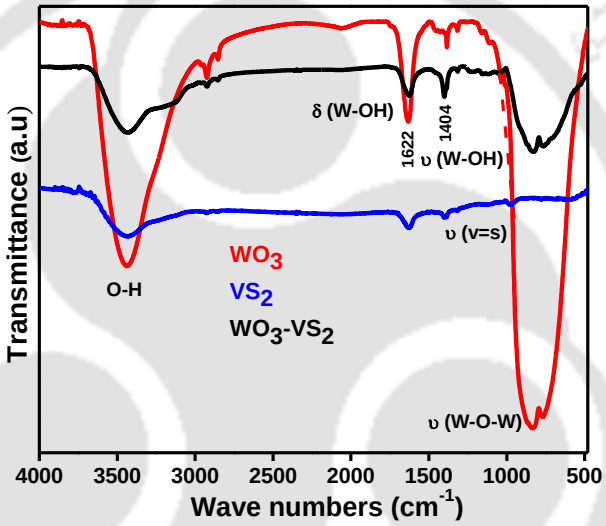

Figure 6.4 Fourier transforms infrared (FTIR) spectra of WO_3, VS_2 and WO_3-VS_2 composites.

Fourier transforms infrared (FTIR) spectra was documented to characterize the surface functional groups as shown in **Figure 6.4**. Monoclinic WO_3 exhibited three distinct peaks at the wavelengths of 1622, 1405, and 804 cm^{-1}, which correspond to W-OH bending vibration mode as a result of adsorbed water molecules, W-O stretching vibration and O-W-O stretching mode respectively.[44] The broad absorption bands at 3450 cm^{-1} was associated with weakly bound surface hydroxyl from ethanol/water. VS_2 shows characteristic band centered at 986 cm^{-1} in the low-frequency region, which can be assigned to υ (V=S) terminal S stretches.[45] In WO_3-VS_2, the

corresponding terminal S stretch of VS_2 was observed at 1020 cm^{-1} which is slightly blue shifted compared to VS_2, which implies an interaction between the components in the composite.

6.3.5 Morphological Analysis

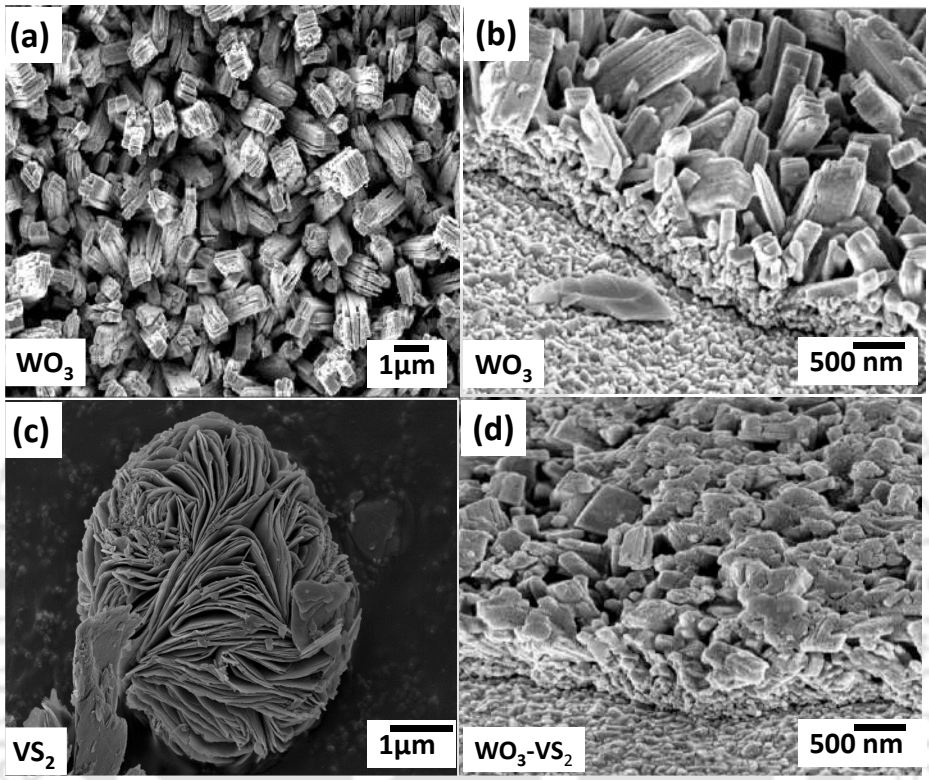

Figure 6.5 Field Emission Scanning Electron Microscopy (FESEM) image of (a) WO_3 (top view) (b) WO_3 (Cross-sectional view) (c) VS_2 (top view) and (d) WO_3-VS_2 (Cross- sectional view).

Morphology of hydrothermally grown WO_3 NFs directly grown onto FTO without the aid of a seed layer was observed by FESEM. WO_3 NF arrays were uniformly distributed over the FTO surface **(Figure 6.5 (a-b))**. The WO_3 NF arrays were about 1 to 2 µm in length. VS_2 has rose petal like morphology with uniform sheets **(Figure 6.5 (c))** having an average size of about 3–4 µm. Uniform sheets were ruptured upon sonication **(Figure 6.6 (a))** and WO_3 NFs were partially covered with a thin layer of VS_2 nanosheets as could be seen from **Figure 6.5 (d)**. Transmission electron microscopy (TEM) image of the composite **(Figure 6.6 (b))** shows WO_3 nanoflake and

sheet like morphology for VS_2 and HRTEM images of WO_3-VS_2 was shown in **Figure 6.6 (c)**. Monoclinic WO_3 NFs and VS_2 with a lattice fringe of 0.38 nm and 0.28 nm between adjacent planes as determined from the HRTEM image, corresponds to the d-spacing of (002) plane of WO_3 and (011) plane of VS_2 respectively. Elemental mapping analysis **(Figure 6.6 (e-h))** shows the presence of the entire component in the WO_3-VS_2 composite without any impurities.

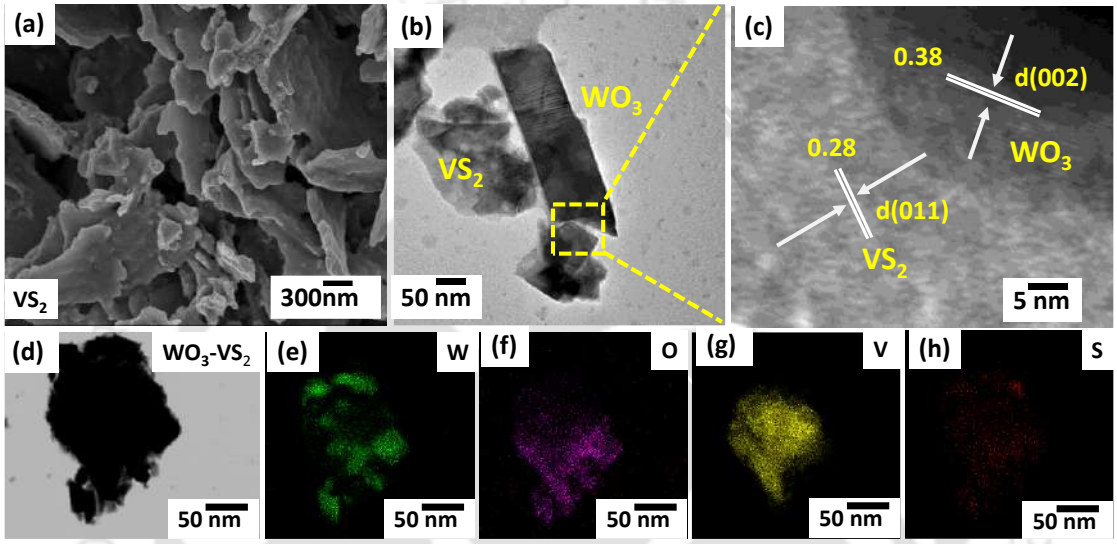

Figure 6.6 (a) Field Emission Scanning Electron Microscopy (FESEM) image of VS_2 (after 30 minutes sonication), (b) Transmission Electron Microscopy (TEM) image of WO_3-VS_2 composite, (c) High Resolution Transmission Electron Microscopy (HRTEM) images of WO_3-VS_2 composite, (d) TEM image of WO_3-VS_2 composites and (e) – (h) the corresponding EDS mapping analysis for WO_3-VS_2 composite.

6.3.6 Photo Current density Voltage (*J-V*) curve and Incident Photon to Current Efficiency (IPCE)

PEC measurements were performed in 0.1M Na_2SO_4 (pH~6.5) under dark and light illumination (100 mW/cm^2). **Figure 6.7 (a)** shows WO_3-VS_2 composite with a significantly enhanced photocurrent density in comparison with pristine WO_3 NFs under simulated solar light irradiation. Substantial increment in photocurrent density of 2.2 mA/cm^2 with VS_2 loaded was obtained, while merely a 0.41 mA/cm^2 for WO_3 at 1.23 V (vs. RHE). With unmodified WO_3, the

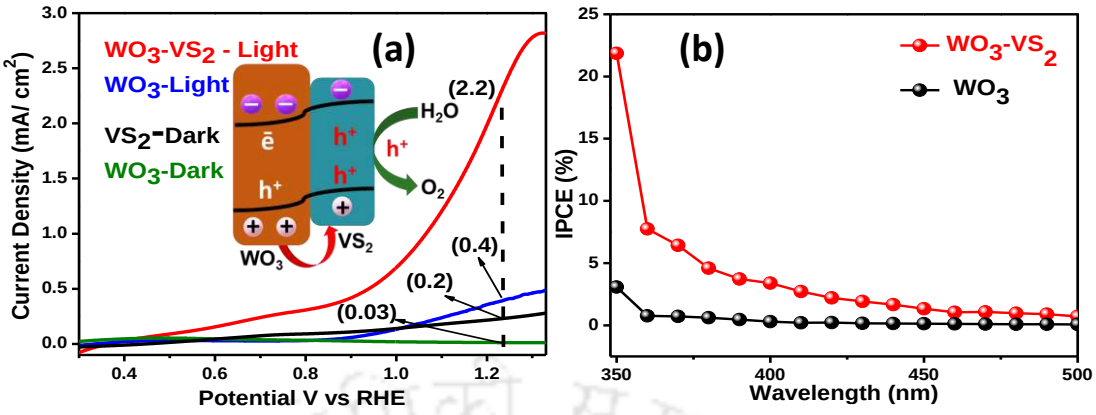

Figure 6.7 (a) Photo Current density – Voltage (*J-V*) curve of WO_3 (dark), WO_3-VS_2 (Dark), VS_2 (dark) WO_3 (light) and WO_3-VS_2 (light) photoanode with a scan rate of 10 mV s^{-1} in 0.1 M Na_2SO_4 under 1 sun illumination. Inset shows the probable charge transfer mechanism in the WO_3-VS_2 composite. (b) IPCE of WO_3 and WO_3-VS_2 in 0.1M Na_2SO_4.

holes generated under light illumination was not consumed quickly enough for surface water oxidation, resulting in enhanced electron-hole recombination. Prominent 5.5-fold enhancement can be attributed to the superior charge separation of surface reactive VS_2 sheets deposited on WO_3, to promote charge extraction and separation which resulted in increased water oxidation. Under light illumination, **(Inset Figure 6.7 (a))** both WO_3 and VS_2 were absorbing the photons and generating electron–hole pairs. The valence band (VB) edge of WO_3 aligns much closer to the VB edge of VS_2 as compared with the conduction band (CB) position of WO_3 with respect to the CB position of VS_2. Therefore, the hole from the VB position of WO_3 can easily be transferred to the VB of VS_2. Based on the band alignments, the photogenerated electrons in VS_2 would partially transfer to the CB of WO_3 driven by the built-in electric field and finally collected by the conductive FTO substrate.[46, 47] The dark current in the WO_3-VS_2 composite with the loading of VS_2 might be attributed to the intrinsic electrocatalytic property of VS_2.[48] Bare WO_3 show a negligible dark current of 0.03 mA/cm^2 while VS_2 show 0.2 mA/cm^2 current in the dark. The dark current in VS_2 and WO_3-VS_2 composite might also be due to the capacitance or charge storage

properties of VS_2 as the capacitance value increase with the loading of VS_2 **(In Table 6.1)**. **Figure 6.7 (b)** shows the IPCE spectra for VS_2 and WO_3-VS_2 composite in 0.1M Na_2SO_4 (pH~6.5), the pristine WO_3 show negligible IPCE value of 3 % while WO_3-VS_2 show a substantially IPCE increment of about 22 %.

6.3.7 Electrochemical impedance spectroscopy (EIS) and Mott–Schottky plots

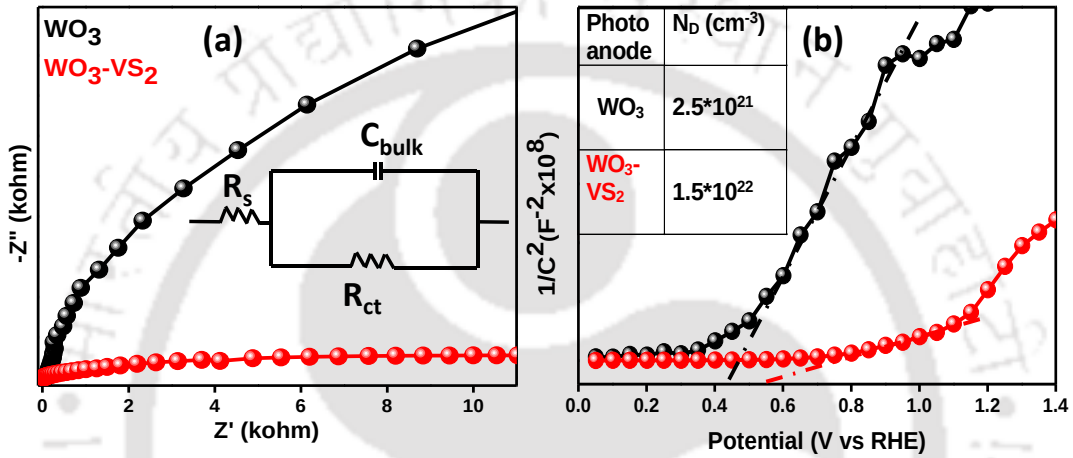

Figure 6.8 (a) Nyquist plots of WO_3 and WO_3-VS_2 photoanode and (b) Mott–Schottky plot documented at 1500 Hz in the dark for WO_3 and WO_3-VS_2 in 0.1M Na_2SO_4.

Electrochemical impedance spectroscopy (EIS) was performed at a potential of 1.23 V (vs. RHE) at a frequency range of 100 kHz to 0.1 Hz, to further examine the interfacial charge transfer kinetics between the photoanode/electrolyte interfaces. As depicted in **Figure 6.8 (a)**, WO_3-VS_2 composite has a smaller arc as compared to bare WO_3 in dark, which implies that deposition of highly surface reactive VS_2 on WO_3 NF's, was conducive to reduce charge transfer resistance in the semiconductor and electrolyte interface. This significantly improved photocurrent of WO_3-VS_2 composite as compared to bare WO_3, which directly signify its lesser charge transfer resistance and recombination kinetics.

Table 6.1: Tabulation of fitted parameters of Nyquist plot at open circuit potential.

Photoanode	R_s (Ω)	C_{bulk}	R_{ct}
WO_3	61.29	1.02×10^{-5}	2.5×10^4
WO_3-VS_2	32.36	1.15×10^{-5}	9073

To associate the changes in Nyquist plots with charge transfer abilities through the bulk and electrolyte interface, EIS data were fitted with an equivalent circuit model (shown in inset of **Figure 6.8 (a)**). From **table 6.1** it was observed that there was a reduction in charge transfer resistance at the surface (R_{ct},) for the composite WO_3-VS_2 (9073 Ω) compared to WO_3 (2.5×10^4 Ω) which implies a facilitated charge transfer in the composite compared to bare WO_3. Moreover, the surface states capacitance was increased in WO_3-VS_2 (1.15×10^{-5} µF) compared to WO_3 (1.02×10^{-5} µF), which could be due to capacitance or charge storage properties of VS_2. From the Mott–Schottky plots as shown in **Figure 6.8 (b)**, both WO_3 and WO_3-VS_2 exhibit positive slopes, indicative of n-type semiconductors, where electrons are the majority charge carriers. Flat-band potential (V_{fb}) values determined by extrapolating the plot at X- intercepts are 0.42 V and 0.54 V vs. RHE corresponding to WO_3 and WO_3-VS_2 respectively. The flat band potential for WO_3-VS_2 was much closer to the OER onset potential of WO_3 (0.7 V vs. RHE). From the slope of tangent lines of the M–S plots, charge carrier density (N_D) can be estimated and a smaller slope indicates a higher carrier concentration. Donor densities calculated were 2.5×10^{21} for WO_3 and 1.5×10^{22} for WO_3-VS_2. Thus, the increased activity of the composite WO_3-VS_2 could be attributed to the increase in carrier concentration. With VS_2 loaded in the composite an increase in capacitance and a reduced charge transfer resistance at the electrode and electrolyte interface favours collection of holes at the photoanode surface for water oxidation. Therefore, a thin layer of VS_2 deposited over

WO_3 photoanode could efficiently promote interfacial charge transfer kinetics in promoting photogenerated charge separation.

6.3.8 Charge Separation Efficiency and Faradaic Efficiency/Yield

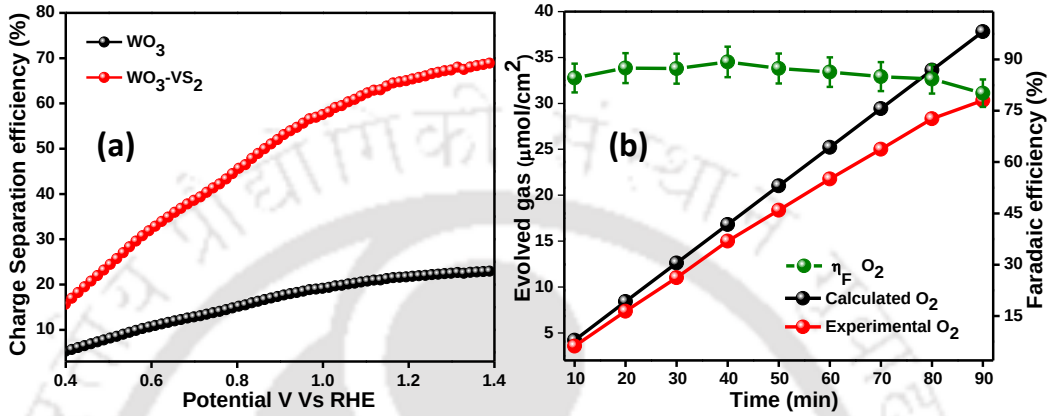

Figure 6.9 (a) Calculated charge separation efficiency for WO_3 and WO_3-VS_2 in presence of 0.1M Na_2SO_4 and 0.1M Na_2SO_3 and (b) Evolved O_2 gases detected by online gas chromatography with Faradaic efficiency for WO_3-VS_2 in 0.1M Na_2SO_4 under 1 sun illumination.

The charge separation efficiency was calculated by measuring the photocurrent density with and without the presence of scavenger (0.1M Na_2SO_3) in the electrolyte. In **Figure 6.9 (a)**, the charge separation efficiency of WO_3-VS_2 was found to be 65 % which is much higher as compared to bare WO_3 (21 %). The enhancement in charge separation could be attributed to the high surface reactivity of VS_2 nanosheets. The calculated solar-to-hydrogen conversion efficiency for WO_3-VS_2 was about 2.35 %. The amount of evolved oxygen from the system was measured using online GC in a gastight PEC cell with a 0.1 M Na_2SO_4 (pH~6.5) electrolyte solution under illumination. The electrolyte was bubbled with nitrogen to completely remove dissolved O_2 in the electrolyte and headspace before the measurement. The Faradaic efficiency was calculated to be about 87 % after 90 minutes of constant light illumination **(Figure 6.9 (b))** by comparing the experimentally produced O_2 amount with that of the theoretical calculation.

6.3.9 Stability Measurements

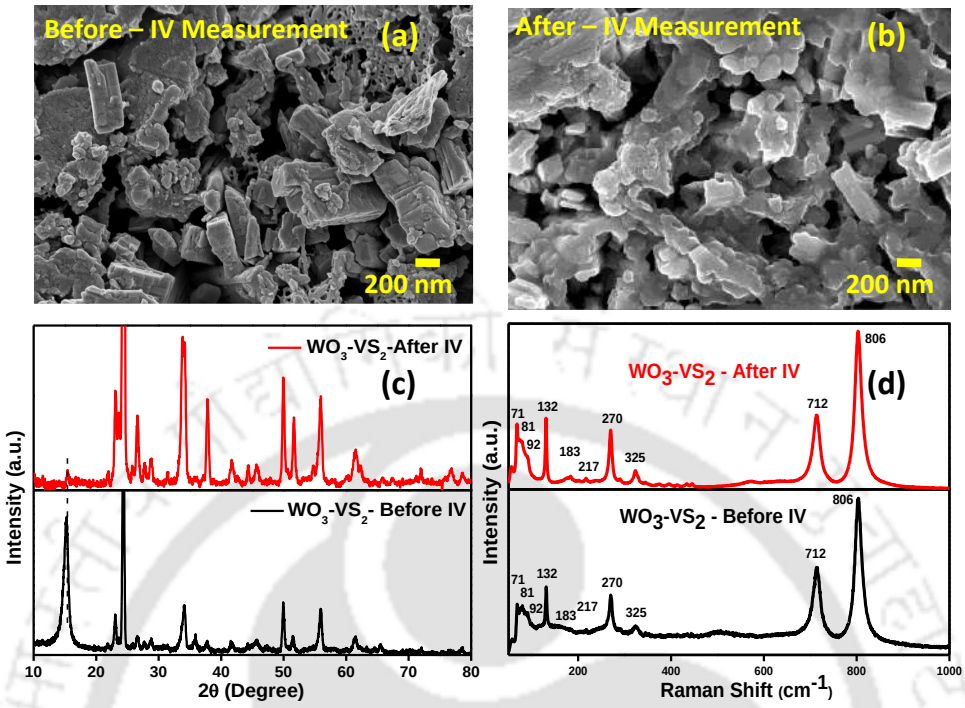

Figure 6.10 (a) and (b) are FESEM image, (c) XRD and (d) Raman spectra of WO_3-VS_2 composite before and after the PEC measurement.

To further know the photoelectrochemical stability of the as synthesize photoanode, we have carried out the FESEM, XRD and Raman analysis **(Figure 6.10)** before and after the PEC measurements. After post-PEC measurements, no significant changes in morphology was observed before and after the PEC measurements as shown in **Figure 6.10 (a)-(b)**. The crystal structure of the as synthesized catalyst also remain unchanged as seen from the PXRD in **Figure 6.10 (c)** and from Raman spectra in **Figure 6.10 (d))** before and after the PEC experiment which further substantiate the stability of the as synthesized photoanode.

Table 6.2: Comparison of photocurrent densities of hetero junction based WO_3 systems w.r.t. literature.

Materials	Morphology	Electrolyte used	J (mA/cm^2)	Ref.
WO_3/ α Fe_2O_3 core-shell	Rod	0.5 M H_2SO_4	1.29 mA/ cm^2 at 1.23 V (vs. RHE)	17
$WO_3/BiVO_4/CoPi$	Nano rod	0.5 M Na_2SO_4 (pH ≈ 7)	5.1 mA/cm^2 at 1.23 V (vs. RHE)	18
WO_3/Cu_2O	Nano rod	1 M H_2SO_4 (pH ≈ 0)	1.37 mA/ cm^2 at 0.8 V (vs. RHE)	19
WO_3/Bi_2S_3	Nano plates	0.1 M Na_2S and 0.1 M Na_2SO_3 (pH ≈ 12)	5.95 mA/ cm^2 at 0.9 V (vs. RHE)	20
WO_3/CdS	Nano sheet	0.1 M Na_2S and 0.1 M Na_2SO_3	1.8 mA/ cm^2 at 0 V (vs. Ag/Agcl)	21
WO_3/ Sb_2S_3	Micro crystal	1 M H_2SO_4	1.79 mA/ cm^2 at 0.8 V (vs. RHE)	22
WO_3/MoS_2	Nano Plate arrays	0.5 M H_2SO_4	0.96 mA/ cm^2 at 1.0 V (vs. RHE)	23
$CoOx/WO_3$	Nano Plate arrays	0.2 M Na_2SO_4 (pH≈ 7)	0.76 mA/ cm^2 at 1.6 V (vs. RHE).	49
Au/ WO_3	Nano Plates	0.1 M Na_2SO_4	2.40 mA/ cm^2 at SCE	50
WO_3/ VS_2	**Nano Plate arrays**	**0.1 M Na_2SO_4**	**2.2 mA/ cm^2 at 1.23 V (vs. RHE)**	**Present Work**

6.4 CONCLUSIONS

In summary, we have successfully fabricated WO_3 NF arrays directly grown onto FTO without a seed layer and highly surface active VS_2 sheets was drop cast onto WO_3 for heterojunction formation. VS_2 serves as a hole trapping from the valence band of WO_3, thereby promoting interfacial electron-hole pair separation. An increment in photocurrent density of about 5.5-fold for WO_3-VS_2 was obtained as compared to bare WO_3. The increment could be contributed to the increase in charge carrier density with better charge separation and reduction in photogenerated charge carrier recombination. This system can perform as a model system to develop highly efficient photoelectrocatalytic system for water oxidation reactions.

6.5 REFERENCES

1 J. Ran, J. Zhang, J. Yu, M. Jaroniec and S. Z. Qiao, *Chem. Soc. Rev.*, 2014, **43**, 7787.

2 E. L. Miller, *Energy Environ. Sci*., 2015, **8**, 2809.

3 A. Fujishima and K. Honda, *Nature*, 1972, **238**, 37.

4 W. Kong, X. Zhang, S. Liu, Y. Zhou, B. Chang, S. Zhang, H. Fan, and B. Yang, *Adv. Funct. Mater.*, 2019, **6**, 1801653.

5 X. Cheng, Y. Zhang and Y. Bi, *Nano Energy*, 2019, **57**, 542.

6 H. Han, S. Kment, K. Karlicky, L. Wang, A. Naldoni, P. Schmuki, and R. Zboril, *Small,* 2018, **14**, 1703860.

7 L. Gao, F. Li, H. Hu, X. Long, N. Xu, Y. Hu, S. Wei, C. Wang, J. Ma and J. Jin, *ChemSusChem,* 2018, **11**, 2502.

8 S. Fu, H. Hu, C. Feng, Y. Zhang and Y. Bi, *J. Mater. Chem. A,* 2019, **7**, 2513.

9 Y. Zhao, S. Balasubramanyam, R. Sinha, R. Lavrijsen, M. A. Verheijen, A. A. Bol and A. Bieberle-Hütter, *ACS Appl. Energy Mater.*, 2018, **1**, 5887.

10 Q. X. Mi, A. Zhanaidarova, B. S. Brunschwig, H. B. Gray and N. S. Lewis, *Energy Environ. Sci*. 2012, **5**, 5694.

11 Y. Gu, W. Zheng and Y. Bu, *J. Electroanal. Chem.*, 2019, **833**, 54.

12 B. Cole, B. Marsen, E. Miller, Y. Yan, B. To, K. Jones and M. AI-Jassim, *J. Phys. Chem. C*, 2008, **112**, 5213.

13 Y. Sun, C. J. Murphy, K. R. Reyes-Gil, E. A. Reyes-Garcia, J. M. Thornton, N. A. Morris and D. Rafery, *Int. J. Hydrogen Energy*, 2009, **34**, 8476.

14 X. J. Shi, L. L. Cai, I. Y. Choi, M. Ma, K. Zhang, J. H. Zhao, J. K. Kim, X. L. Zheng and J. H. Park, *J. Mater. Chem. A,* 2018, **6**, 19542.

15 H. Li, H. Yu, X. Quan, S. Chen and Y. Zhang, *ACS Appl. Mater. Interfaces*, 2016, **8**, 2111.

16 S. S. Kalanur, Y. J. Hwang, S.Y. Chae and O. S. Joo, *J. Mater. Chem. A*, 2013, **1**, 3479.

17 X. Fan, T. Wang, H. Xue, B. Gao, S. Zhang, H. Gong, H. Guo, L. Song, W. Xia and J. He, *ChemElectroChem*, 2019, **6**, 543.

18 Y. Pihosh, I. Turkevych, K. Mawatari, T. Asai, T. Hisatomi, J. Uemura, M. Tosa, K. Shimamura, J. Kubota, K. Domen and T. Kitamori, *small*, 2014, **10**, 3692.

19 J. Zhang, H. Ma and Z. Liu, *Appl. Catal., B*, 2017, **201**, 84.

20 Y. Wang, W. Tian, L. Chen, F. Cao, J. Guo and L. Li, *ACS Appl. Mater. Interfaces*, 2017**, 9,** 40235.

21 Y. Liu, Y. Cui, F. Huang and X. Yang, *RSC Adv*., 2016, **6**, 16668.

22 J. Zhang, Z. Liu and Z. Liu, *ACS Appl. Mater. Interfaces*, 2016, **8**, 9684.

23 Y.-H. Xiao and W.-D. Zhang, *Electrochim. Acta*, 2017, **253**, 416.

24 M. Shao, Y. Shao, S. Ding, J. Wang, J. Xu, Y. Qu, X. Zhong, X. Chen, W. F. Ip, N. Wang, B. Xu, X. Shi, X. Wang and H. Pan, *Appl. Catal., B*, 2018, **237**, 295.

25 C. Du, D. Liang, M. Shang, J. Zhang, J. Mao, P. Liu and W. Song, *ACS Sustainable Chem. Eng.*, 2018, **6**, 15471.

26 X. Zhong, J. Tang, J. Wang, M. Shao, J. Chai, S. Wang, M. Yang, Y. Yang, N. Wang, S. Wang, B. Xu and H. Pan, *Electrochim. Acta*, 2018, **269**, 55.

27 Y. Zhang, Y.-Z. Lin, Z.-X. Wang, K. Li, T. Li and F.-T. Liu, *Catal. Sci. Technol.*, 2019, **9**, 583.

28 G. Gogoi, C. T. Moi, A. S. Patra, D. Gogoi, N. R. Peela and M. Qureshi, *Chem. - Asian J.*, 2019, **14**, 4607.

29 X. Chen, K. Yu, Y. Shen, Y. Feng, and Z. Zhu, *ACS Appl. Mater. Interfaces*, 2017, **9**, 42139.

30 M. N. Rantho, M. J. Madito, F. O. Ochai–Ejeh and N. Manyala, *Electrochim. Acta,* 2018, **260**, 11.

31 A. Samad and Y.-H. Shin, *ACS Appl. Mater. Interfaces,* 2017, **9**, 29942.

32 Y. Qu, M. Shao, Y. Shao, M. Yang, J. Xu, C. T. Kwok, X. Shi, Z. Lu and H. Pan, *J. Mater. Chem. A*, 2017, **5**, 15080.

33 S. S. Kalanur, Il-H. Yoo, K. Eom and H. Seo, *J. Catal.*, 2018, **357**, 127.

34 J. Zhang, Y. Guo, Y. Xiong, D. Zhou and S. Dong, *J. Catal.*, 2017, **356**, 1.

35 T. Soltani, A. Tayyebi, H. Hong, M. H. Mirfasih and B.-K. Lee, *Sol. Energy Mater. Sol. Cells,* 2019, **191**, 39.

36 H. Liang, H. Shi, D. Zhang, F. Ming, R. Wang, J. Zhuo and Z. Wang, *Chem. Mater.* 2016, **28**, 5587.

37 Y. Wang, Z. Sofer, J. Luxa, and M. Pumera, *Adv. Mater. Interfaces*, 2016, **3**, 1600433.

38 Y. Wang, L. Liu, C. Meng, Y. Zhou, Z. Gao, X. Li, X. Cao, L. Xu and W. Zhu, *Scientific Reports*, 2016, **6**, 33092.

39 C. M. Ghimbeu, E. R.-Piñero, P. Fioux, F. Béguin and C. V.-Guterl, *J. Mater. Chem.*, 2011, **21**, 13268.

40 G. kiss, H. Paulus, O. Krafcsik, F. Réti, K.-H. Müller, J. Giber, *Fresenius' J. Anal. Chem.*, 1999, **365**, 203.

41 G. Li, J. Sun, W. Hou, S. Jiang, Y. Huang and J. Geng, *Nat. Commun.*, 2016, **7**, 10601.

42 L. Zhang, L. Ji, P.-A. Glans, Y. Zhang, J. Zhu and J. Guo, *Phys. Chem. Chem. Phys.*, 2012, **14**, 13670.

43 S. V. P. Vattikutia, A. K. R. Police, J. Shima and C. Byon, *Appl. Surf. Sci.*, 2018, **447**, 740.

44 J. Wang, Z. Chen, G. Zhai and Y. Men, *Appl. Surf. Sci.* 2018, **462**, 760.

45 B. Pandit, L. K. Bommineedi and B. R. Sankapal, *J. Energy Chem.*, 2018, **0**, 1.

46 S. Kuang, L. Yang, S. Luo and Q. Cai, *Appl. Surf. Sci*., 2009, **255**, 7385.

47 X. Chai, H. Zhang, Q. Pan, J. Bian, Z. Chen and C. Cheng, *Appl. Surf. Sci*., 2019, **470**, 668.

48 F.-X. Xiao and B. Liu, *Nanoscale*, 2017, **9**, 17118.

49 M. Sarnowska, K. Bienkowski, P. J. Barczuk, R. Solarska and J. Augustynski, *Adv. Energy Mater*., 2016, **6,** 1600526.

50 D. Hu, P. Diao, D. Xu and Q. Wu, *Nano Res.*, 2016, **9**, 1735.

CHAPTER 7

Thesis overview and future perspectives

The current chapter, in brief, summaries the outcomes of the present thesis work. Herein, it also discusses the future scope for improvement to enhance the (photo)electrochemical performance of metal oxides for OER and HER reactions.

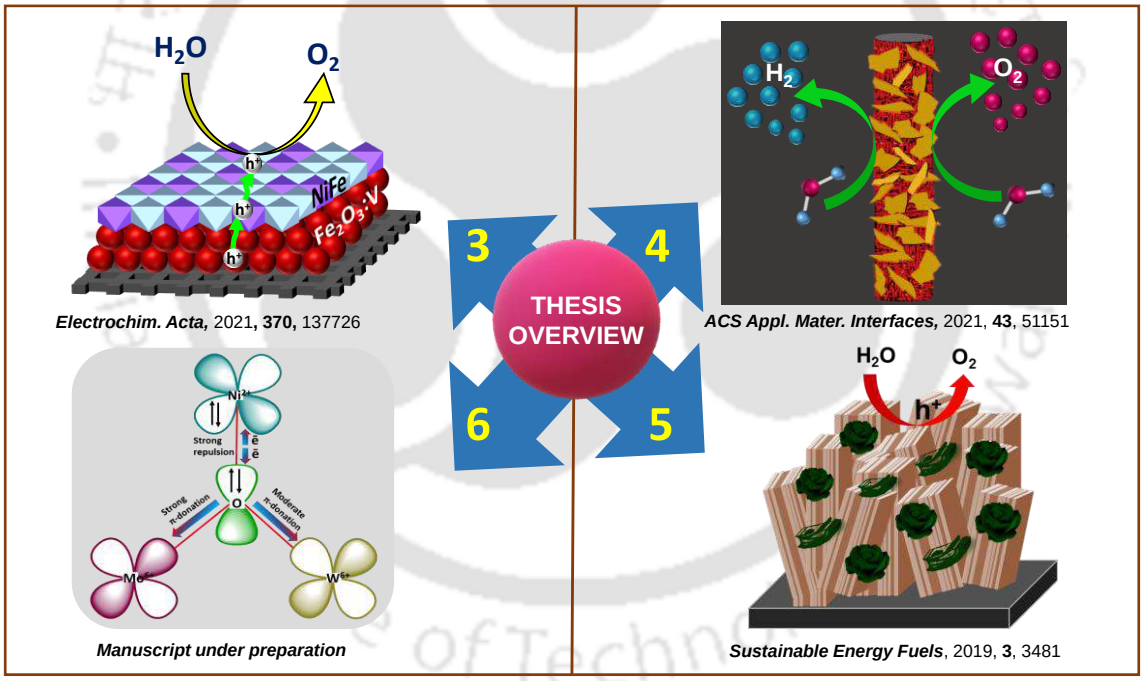

Thesis Overview:

The present thesis discussed the design of *insitu* grown metal oxides/hydroxide for (photo)electrochemical oxygen evolution reaction (OER) and hydrogen evolution reaction (HER). Herein, low cost, efficient and stable metal oxide and hydroxide such as WO_3, Fe_2O_3, FeO(OH) and FeVO(OH) are employ as model system to study their (photo)electrocatalytic properties. Different strategies like morphological modification, co-catalyst modification, elemental doping, and heterojunction strategies are employed to enhance the water splitting performance. The fabrication of catalyst directly onto substrate (carbon paper/ Fluorine doped tin oxide) is emphasized in this thesis. The thesis includes 7 chapters, which are summarize below:

Chapter 1: Chapter one demonstrates the basic technique of (photo)electrochemical water splitting to meet global energy demands and environmental crises. The present chapter also describes the working principle of (photo)electrochemical water splitting in different electrolytic conditions. This chapter also discussed the literature survey of current state-of-the-art scenarios, challenges, and various strategies for the development of stable, efficient, cheap, and abundant catalysts for practical application.

Chapter 2: This chapter discusses the comprehensive synthetic protocols of the metal oxides/hydroxide and the co-catalysts, which were employed to show (photo)electrochemical water splitting. The chapter also describes instrumentation techniques used in the characterization of the materials. It demonstrates the complete experimental procedure used in (photo)electrochemical characterization of the catalysts. In this chapter, different performance perimeters for photo and electrocatalysts are also discussed in brief.

Chapter 3: Enhanced Surface Reaction Kinetics in Vanadium Doped Hematite co-modified by NiFe Layered Double Hydroxide for Electrocatalytic Oxygen Evolution Reaction. **(C. T. Moi et al., *Electrochim. Acta*, 2021, 370, 137726)**

The present chapter describes exploring a low-cost, efficient and stable electrocatalyst to replace noble metal-based catalysts for oxygen evolution reaction (OER) for practical applications. Herein, we have proposed vanadium doping and co-modification of α- Fe_2O_3 utilizing NiFe LDH for noble metal-free electrocatalytic oxygen evolution reaction (OER), which exceeds the performance of benchmark RuO_2 under similar experimental conditions. Vanadium doping enhances the carrier density, whereas NiFe LDH contributes to the surface-active sites for promoting water oxidation kinetics. A five-fold enhancement in electrochemically active surface area (ECSA) for α- Fe_2O_3:V-NiFe LDH (2.5 mF/cm^2) as compared to α- Fe_2O_3 (0.5 mF/cm^2) is observed. α- Fe_2O_3:V-NiFe LDH exhibited an impressive overpotential of 190 mV @ 10 mA/cm^2 with corresponding Tafel slopes of 42 mV/dec. Detailed electrochemical studies with long-term stability indicate the potential of as-synthesized composite α- Fe_2O_3:V-NiFe LDH for utilization as a heterogeneous catalyst for efficient oxygen evolution reaction.

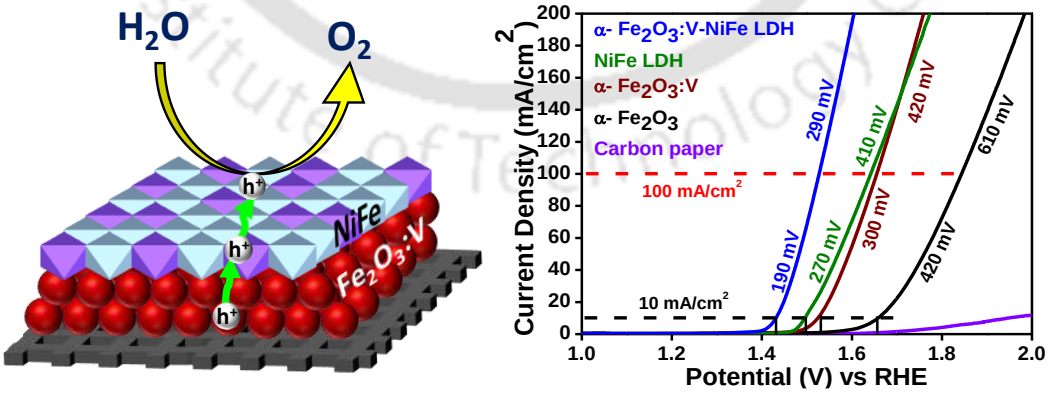

Figure 1: Graphical illustration of probable reaction mechanism of α- Fe_2O_3:V-NiFe LDH along with *JV* of all prepared electrocatalyst in 1M KOH.

Chapter 4: Hierarchical FeO(OH)/CoCeV (oxy)hydroxide as a water cleavage promoter (C. T. Moi et al., ACS Appl. Mater. Interfaces, 2021, 13, 51151–51160)

Search for a bifunctional electrocatalyst having water cleavage promoting ability along with the operational stability to efficiently generate oxygen and hydrogen could lead to robust systems for applications. These fundamental ideas can be achieved by designing the morphology, tuning the electronic structure, and using dopants in their higher oxidation states. Herein, we have fabricated a binder-free FeO(OH)-CoCeV-layered triple hydroxide (LTH) bifunctional catalyst by a two-step hydrothermal method, in which the nanograin-shaped FeO(OH) coupled with CoCeV-LTH nanoflakes provide more electro catalytically active sites and enhanced the charge transfer kinetics for hydrogen evolution reaction (HER) and oxygen evolution reaction (OER). The composition-optimized electrocatalyst (FeO(OH)-$Co_{0.5}Ce_{0.05}V_{0.15}$-LTH) acts as an efficient water cleavage composite by its favorable oxidation states leading to cyclic redox couples which yields an overpotential of 53 mV for HER, and 227 mV for OER to drive 10 mA/cm^2 current density in 1M KOH, with a corresponding Tafel slope of 70 mV/dec for HER and 52 mV/dec for OER. Furthermore, for the overall water splitting reaction, FeO(OH)-$Co_{0.5}Ce_{0.05}V_{0.15}$-LTH requires a cell voltage of 1.52 V vs RHE to drive 10 mA/cm^2 current density.

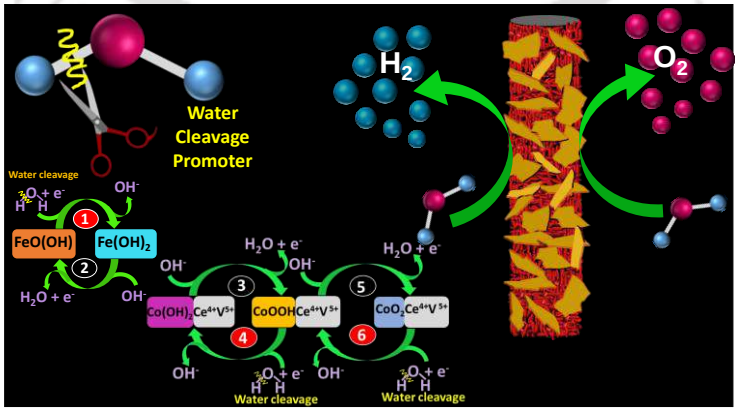

Figure 2: Graphical representation of probable water cleavage mechanism of FeO(OH)-$Co_{0.5}Ce_{0.05}V_{0.15}$-LTH.

Chapter 5: Tapping the potential of high-valent Mo and W metal centres for dynamic electronic structure in multi-metallic FeVO(OH)/$Ni(OH)_2$ for water splitting (manuscript under preparation)

Rationally designing a noble metal-free electrocatalyst for OER and HER is pivotal for large-scale energy generation via water splitting. Multi-metallic electrocatalyst FeVO(OH)/ $Ni_{0.86}Mo_{0.07}W_{0.07}(OH)_2$ aiming at tuning the electronic structure is fabricated, giving a huge improvement in water splitting reaction kinetics. By taking the advantage of (ē–ē) repulsions at the t_{2g} level, we have introduced high-valent Mo and W to provide a viable path for π–electron donation from oxygen 2p orbitals to vacant Mo and W orbitals for a dynamic electronic structure and interfacial synergistic effect which optimized the bond lengths for reaction intermediates to facilitate the water-splitting. The experimental data shows that the hybrid heterostructure FeVO(OH)/$Ni_{0.86}Mo_{0.07}W_{0.07}(OH)_2$ requires 231 mV for OER and 156 mV for HER to drive 20 mA/cm^2 with a corresponding Tafel slope value of 24 mV/dec for OER and 67 mV/dec for HER respectively.

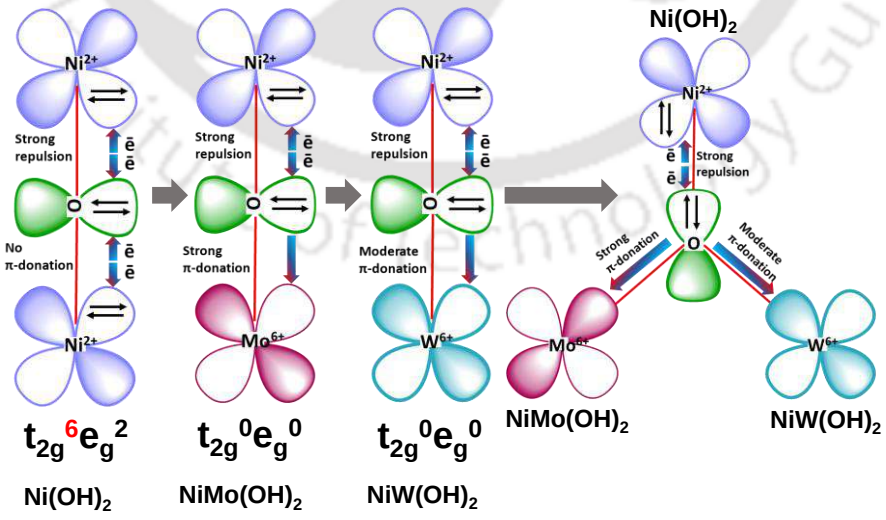

Figure 3: Schematic illustrations of the electronic coupling between Ni^{2+}, Mo^{6+} and W^{6+} of $NiMoW(OH)_2$.

Chapter 6: Noble metal-free hierarchical VS_2 onto WO_3 nanoflakes as heterojunction strategy for photoelectrochemical water oxidation **(C. T. Moi et al., *Sustainable Energy Fuels*, 2019, 3, 3481)**

Chapter 6 describes the design of highly surface reactive and noble metal-free VS_2 nanoflowers onto in situ grown WO_3 photoanode as a heterojunction strategy for efficient charge separation. The main drawback of WO_3 is slow-to-surface reaction kinetics leading to undesired carrier recombination. VS_2, with active sites both on the edge and basal plane, reduces the surface charge recombination and enhances the kinetics of O_2 evolution reaction. The current chapter study about the charge carrier density, charge transfer kinetics, and durability of the prepared catalyst for PEC water oxidation. A significant increment in photocurrent density is observed for WO_3-VS_2 composite as compared to the bare WO_3 with an increase in charge carrier density from 2.5 x 10^{21} for WO_3 to 1.5 x 10^{22} for WO_3-VS_2. Electrochemical impedance spectroscopy indicates an effective reduction in charge transfer resistance from 7.71 x 10^5 for WO_3 to 2.79 x 10^3 for WO_3-VS_2. A Faradaic efficiency of 87 % is indicative that the oxygen generated in the reaction is mainly due to photoelectrochemical water oxidation.

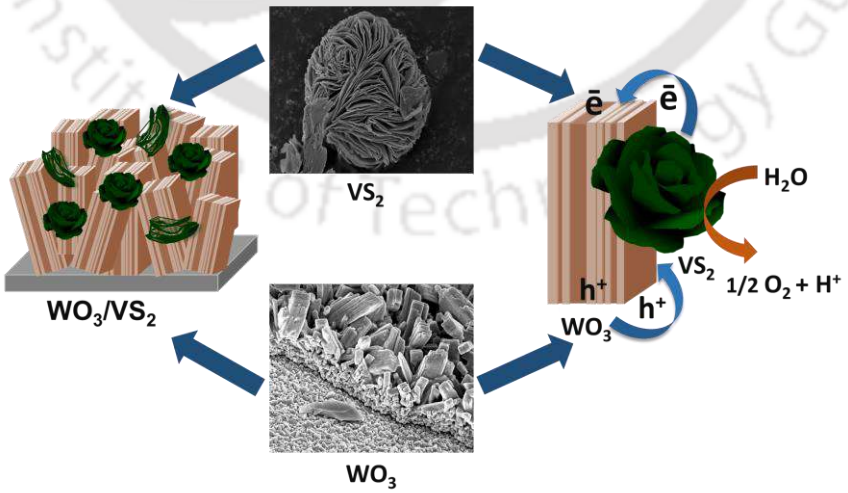

Figure 4: Schematic illustrations of synthesis and reaction mechanism of WO_3-VS_2.

Future Perspective

The thesis discussed the brief study of metal oxide/hydroxide to address the drawback of charge carrier recombination, slow surface reaction kinetics, ohmic contact at the interface and electrochemical surface active sites for (photo)electrochemical water splitting. The research findings and different strategies employ in this thesis have made substantial improvements in the field of (photo)electrochemical water splitting. However, there is a great scope for improvement as the efficiency of metal oxide/hydroxide is lower than their theoretical efficiency for water splitting. The various scope to further improve the water splitting efficiency are as follows:

- Synthesizing of catalyst which is active for OER and HER in the same electrolytic medium such as, Co/W doped VS_2, V/N doped NiS_2, W/P doped $Co(OH)_2$.
- Non-metal doping on metal oxide/hydroxide to enhance the number of electrochemically surface active sites and improves the overall water splitting properties.
- Morphological modification to enhances electrolyte penetration and increases the number of catalytically surface active sites.
- Fabrication of catalyst to reduce diffusion length and to optimize adsorption energy of reaction intermediates for HER and OER.

LIST OF PUBLICATIONS AND CONFERENCES/WORKSHOPS ATTENDED

Journal Articles:

Included in Thesis:

1. **Ching Thian Moi,** et al., Design of noble metal free hierarchical VS_2 onto WO_3 nanoflakes as an effective heterojunction strategy for enhanced photoelectrochemical water oxidation, ***Sustainable Energy Fuels***, 2019, **3**, 3481.
2. **Ching Thian Moi,** et al., Electrocatalytic oxygen evolution surpassing benchmark RuO_2 using stable, noble metal free vanadium doped hematite co-modified by NiFe Layered Double Hydroxide, ***Electrochim. Acta,*** 2021, **370**, 137726.
3. **Ching Thian Moi,** et al., Hierarchical FeO(OH)–CoCeV (Oxy)hydroxide as a water cleavage promoter, ***ACS Appl. Mater. Interfaces,*** 2021, **43**, 51151.
4. **Ching Thian Moi,** et al., Tapping the potential of electro-inactive high-valent Mo and W metal centres for dynamic electronic structure in multi-metallic FeVO(OH)/$Ni(OH)_2$ for ultra-stable and efficient water splitting, ***ACS Appl. Mater. Interfaces***, 2023, 15, 5336.

Work Contributed Off the Thesis:

1. Gaurangi Gogoi, **Ching Thian Moi,** et al., A Z-zcheme strategy that utilizes $ZnIn_2S_4$ and hierarchical VS_2 microflowers with improved charge-carrier dynamics for superior photoelectrochemical water oxidation, ***Chem.–Asian J.,*** 2019, **14**, 4607-4615.
2. Sourav Bhowmick, **Ching Thian Moi,** et al., Spontaneous Fenton-like dye degradation in clustered-petal di-manganese copper oxide by virtue of self-cyclic redox couple, ***J. Environ. Chem. Eng.,*** 2021, **9**, 106094.
3. Sourav Bhowmick, Arijeet Sarangi, **Ching Thian Moi**, Sudip Chakraborty, and Mohammad Qureshi, Diffusion-Mediated Morphological Transformation in Bifunctional Mn_2O_3/CuO–$(VO)_3(PO_4)_2 \cdot 6H_2O$ for Enhanced Electrochemical Water Splitting, **ACS *Applied Materials & Interfaces,*** 2022, **14**, 52204

Conferences/Workshops:

1. International Conference on Frontiers in Chemical Sciences (**FICS-2018**), 6-8th December 2018, Indian Institute of Technology Guwahati, Guwahati, India. (**Poster Presented**)
2. 6th International Conference on Advanced Nanomaterials and Nanotechnology (**ICANN-2019**), 18-21 December, 2019, Indian Institute of Technology Guwahati, Guwahati, India. (**Poster Presented**)
3. International Conference on Recent Advances and Innovation in Solar Energy **(RAISE 2021)**, 2 – 4th December, 2021, Indian Institute of Technology Madras Chennai, India. (**Oral Presented**)
4. 7th International Conference on Advanced Nanomaterials and Nanotechnology (**ICANN-2021**), 14-17 December, 2021, Indian Institute of Technology Guwahati, Guwahati, India. (**Oral Presented**)
5. 29th National Conference on Condensed Matter Physics **(CMDAYS 2021),** 10-12 December, 2021, Department of Physics, Central University of Jharkhand, Ranchi, Jharkhand. (**Oral Presented**)
6. 28th National Symposium in Chemistry, Chemical Research Society of India (CRSI) & RSC Joint Symposium, 25-27 March, 2022, Indian Institute of Technology Guwahati, Guwahati, India. (***Best poster awarded***)
7. North East Research Conclave **(NERC 2022)**, 20–22 May, 2022, Indian Institute of Technology Guwahati, Guwahati, India. (**Poster Presented**)
8. Scientific Writing Workshop Organized by ACS Publications in collaboration with IIT Bhilai, 20th September, 2021. (**Attended**)
9. Royal Society of Chemistry (RSC)-IIT Desktop Seminar with Journal of Materials Chemistry A **(**JMCA), 27th October, 2021. (**Attended**)